

## ABSTRACT

Title of Dissertation: THIN FILMS FOR IMPROVED  
RESOLUTION OF THREE COLOR  
LITHOGRAPHY

Sandra A. Gutierrez Razo Doctor of  
Philosophy, 2023

Dissertation directed by: John T. Fourkas, Department of Chemistry and  
Biochemistry

The goal of this project is to create thin films to improve resolution for 3-color lithography (3CL). Lithography is a technique that is used to pattern semiconductor chips. The current methods used to manufacture chips use deep and extreme ultraviolet light to create patterns on a photoresist. 3CL is an alternative that creates patterns using easily-accessible visible light instead of dangerous radiation that requires specialized and prohibitively expensive equipment. This work focuses on improving the resolution of the 3CL technique by using thin negative tone acrylate photoresist films.

Modern microelectronic devices require semiconductor chips that have individual features less than 100 nm wide and patterns with features that pack closely together. The industry is moving to shorter wavelengths because feature size is directionally proportional to the wavelength of the light used. However, 3CL uses visible light, which has larger wavelengths than the desired feature size. One way to

reduce the size of features is to shape and overlap the beams so that not all irradiated areas result in fabricated features. Two beams are used to excite the photoinitiator in the photoresist to initiate radical polymerization in the acrylate monomers. The third beam is used to deactivate the photoinitiator, thus inhibiting polymerization before it can occur.

Another requirement for semiconductor chip patterns is high resolution, or closely packed features. To prevent unwanted polymerization between features in 3CL, and thereby increase resolution, initiation and deactivation should occur from different photoinitiator excited states. Therefore, a 3CL photoinitiator should have a long-lived chemically inactive excited state where either deactivation can relax it back down to the ground state, or further excitation can bring it to the chemically active excited state. We examine isopropylthioxanthone (ITX) and its excited states to probe for 3CL behavior.

Deactivation limits the feature width, but the deactivated features in the bulk material are taller than their width and collapse. Thin films are employed to correct the aspect ratio and further improve resolution.

This project focuses on ITX's performance as a 3CL photoinitiator, the procedure to produce 40 nm thin films, and how polymerization and deactivation are different in thin film samples compared to the micron-thick bulk samples.

THIN FILMS FOR IMPROVED RESOLUTION IN THREE COLOR  
LITHOGRAPHY

by

Sandra A. Gutierrez Razo

Dissertation submitted to the Faculty of the Graduate School of the  
University of Maryland, College Park, in partial fulfillment  
of the requirements for the degree of  
Doctor of Philosophy  
2023

Advisory Committee:

Professor John T. Fourkas, Chair

Professor Daniel E. Falvey

Professor Amy S. Mullin

Professor Leah Dodson

Professor Mohamad Al-Sheikhly

© Copyright by  
Sandra A. Gutierrez Razo  
2023

# Dedication

For Jim.

## **Acknowledgements**

I'd like to thank my advisor, John Fourkas, as well as my committee members, Dan Falvey, Amy Mullin, Leah Dodson, and Mohamad Al-Sheikhly. Past and current members of the Fourkas group have taught me so much and provided much needed support and encouragement.

# Table of Contents

Dedication.....	ii
Acknowledgements.....	iii
Table of Contents.....	iv
Chapter 1 : Background.....	1
1.1 Introduction.....	1
1.2 Multiphoton absorption polymerization (MAP).....	2
1.3 Two-color lithography (2CL).....	3
1.4 Three-color lithography (3CL).....	3
1.5 Parts of the document.....	5
Chapter 2 : Experimental setup.....	6
2.1 Optical Setup.....	6
2.2 Preparation of thick-film samples.....	8
2.21 Substrates.....	8
2.22 Photoresist.....	9
2.23 Microscope samples.....	9
Chapter 3 : <i>In situ measurement of the effective nonlinear absorption order in multiphoton photoresists</i> .....	11
3.1 Introduction.....	12
3.2 Theory.....	14
3.3 Experimental section.....	16
3.31 Optical setup.....	16
3.32 Sample preparation.....	17
3.33 2-BIT measurements.....	18
3.4 Results and discussion.....	19
3.5 Conclusions.....	22
Chapter 4 : <i>Elucidating complex triplet-state dynamics in the model system isopropylthioxanthone</i> .....	24
4.1 Abstract.....	24
4.2 Introduction.....	25
4.3 Results.....	29
4.31 Effective order of nonlinearity of ITX photoresists.....	29
4.32 Triplet-state absorption.....	35
4.33 Phosphorescence.....	48
4.34 Kinetic modeling.....	54
4.35 Implications for resolution.....	59
4.4 Discussion.....	62
4.5 Conclusion.....	67
Chapter 5 : Thin films for high-resolution, 3-color lithography.....	69
5.21 Abstract.....	69
5.22 Thin film preparation.....	70
5.23 Materials and Procedure.....	74
5.24 Results.....	75

5.25 Conclusion .....	78
Chapter 6 : <i>Oxygen effects in thin films for high-resolution, 3-color lithography</i> .....	79
6.1 Abstract .....	79
6.2 Introduction.....	79
6.23 Sample preparation .....	82
6.24 Results.....	86
6.25 Conclusions.....	88
Chapter 7 : Impact and Future work .....	89
Appendices.....	90
Bibliography .....	99

## List of Tables

Table 1.1 Polymerizaion thresholds.....	5
Table 4.1 ITX triplet-state lifetimes in different solvents as measured by microsecond transient absorption.....	39

## List of Figures

Figure 2.1 Simplified schematic of the polymerization and deactivation beams. ....	8
Figure 3.1 Photoinitiators studied in this chapter. ....	18
Figure 3.2 2-BIT data for photoresists. ....	20
Figure 3.3 2-BIT data for photoresists. ....	22
Figure 4.1 Multiphoton exposure of an ITX/PETA photoresist. ....	30
Figure 4.2 2-BIT data for a photoresist consisting of 1.5 wt% of ITX in PETA. ....	33
Figure 4.3 Analysis of 2-BIT data in an ITX/PETA photoresist. ....	34
Figure 4.4 Deactivation and self-deactivation of ITX. ....	37
Figure 4.5 Vertical transition energies for the lowest singlet and triplet states of 4-ITX in vacuum. ....	41
Figure 4.6 Vertical transition energies for the lowest singlet and triplet states of 4-ITX in tetrahydrofuran. ....	41
Figure 4.7 Vertical transition energies for the lowest singlet and triplet states of 4-ITX in ethyl acetate. ....	42
Figure 4.8 Vertical transition energies for the lowest singlet and triplet states of 4-ITX in ethylene glycol. ....	42
Figure 4.9 Vertical transition energies for the lowest singlet and triplet states of 4-ITX in water. ....	43
Figure 4.10 Transient absorption spectra of ITX in glyme. ....	44
Figure 4.11 In situ monitoring of exposure and deactivation. ....	45
Figure 4.12 Microsecond transient absorption experiments on ITX/PETA photoresists containing ethyl lactate. ....	47
Figure 4.13 Luminescence studies of ITX in PEG-400. ....	49
Figure 4.14 Fluorescence spectra of ITX in different solvents. ....	50
Figure 4.15 Schematic of the experimental setup for 2-beam constant emission intensity (2-BCEIn) spectroscopy. ....	52
Figure 4.16 Kinetic model for self-deactivation. ....	56
Figure 4.17 Schematic representation of the experimental setup for 2-beam initiation threshold with deactivation (2-BITD) spectroscopy. ....	61
Figure 4.19 Schematic representation of the most important photophysical processes that take place in the ITX photoresist. ....	63
Figure 5.1 Representation of the chemical nature of a SiO <sub>2</sub> -coated Si wafer surface. ....	71
Figure 5.2 (3-Aminopropyl) triethoxysilane. ....	72
Figure 5.3 Representative schematic of the SiO <sub>2</sub> -coated Si wafer surface once functionalized with 3-(aminopropyl) triethoxysilane. ....	72
Figure 5.4 Acrylic monomers used to functionalize thin film substrates for this work. ....	73
Figure 5.5 Result of Michael addition of the monomers to the functionalized substrate. ....	73
Figure 5.6 AFM images of 3CL behavior in thin films on glass cover slips. ....	76
Figure 5.7. AFM images of substrates during substrate and film preparation steps. ....	76
Figure 5.8 Plot of film thickness etched at the same plasma conditions. ....	77
Figure 6.1 SEM image of features fabricated with the 3CL technique in 600-nm-thick films. ....	81

Figure 6.2 Adapted from Zhou et al., <sup>97</sup> the figure above shows the roles of oxygen in our resist.....	82
Figure 6.3 Acrylic monomers used for this work .....	84
Figure 6.4 Experimental setup showing a single-beam experiment .....	85
Figure 6.5 Plots of the three photoresists with varying viscosities.....	87
Figure 6.6 Plots of the most viscous photoresist with increased oxygen .....	87

## List of Abbreviations

Abbreviation	Definition
2-BA	2-beam action
2-BAD	2-beam action with deactivation
2-BCEIn	2-beam constant emission intensity
2-BIT	2-beam initiation threshold
2-BITD	2-beam initiation threshold with deactivation
AFM	atomic force microscopy
APTES	(3-aminopropyl) triethoxysilane
CCD	charged-coupled device
CHIPS	Creating Helpful Incentives to Produce Semiconductors
CW	continuous wave
DAS	deactivation action spectroscopy
DFT	density functional theory
ESA	excited-state absorption
EUV	extreme ultraviolet
ISC	intersystem crossing
ITX	isopropylthioxanthone
IVR	intramolecular vibrational relaxation
LED	light-emitting diode
MACS	multiphoton absorption cross sections
MAP	multiphoton absorption polymerization
ML	mode-locked
NA	numerical aperture
Nd:YAG	neodymium-doped yttrium aluminum garnet
OBJ	objective
OPO	optical parametric oscillator
PBC	polarizing beam cube
PC	personal computer
PD	photodiode
PEG	polyethylene glycol
PETA	pentaerythritol triacrylate
PSI	Periodic Structures, Inc.
RISC	reverse intersystem crossing
RMS	root mean square
RPM	revolutions per minute
SEM	scanning electron microscope

STED	stimulated emission depletion
THF	tetrahydrofuran
TLC	thin layer chromatography
TMPTA	trimethylolpropane triacrylate
TPO-L	ethyl phenyl(2,4,6-trimethylbenzoyl)phosphinate
TX	thioxanthone
UV	ultraviolet

# Chapter 1 : Background

## 1.1 Introduction

Microelectronics have become integral in our lives, in applications ranging from communication and transportation to cutting edge medical devices and security systems. Recently, the Biden-Harris administration has acknowledged what professionals in the semiconductor industry have asserted for decades: supply is unable to keep up with demand for semiconductor chips. The industry is quickly reaching its technical limits, and the 2020 pandemic laid bare the uncomfortable reality that localized supply-chain disruptions can quickly cause global economic consequences. In addition to the supply-chain disruptions, semiconductor-chip manufacturing in the United States has dropped from almost 40% of the global supply in the 1990s to a projected less than 10% in 2030. Currently, 85% of semiconductor fabrication occurs in Asia.<sup>1</sup> In September 2022, the President's Council of Advisors on Science and Technology recommended the 11 billion dollars appropriated via the CHIPS and Science Act be directed into revitalizing semiconductor fabrication in North America. They further recommend a focus on research and development, as well as on education and workforce development, to reverse the decline in manufacturing in the United States.

An early stage of the current semiconductor manufacturing process employs extreme ultraviolet (EUV) lithography using the shortest possible wavelengths of light to produce small features. As the wavelength decreases, the feature size also decreases, meaning that a single chip can be smaller and more densely packed. The

industry is now using soft X-rays. These wavelengths are dangerous and destructive, thus requiring expensive and specialized materials and optics. A single EUV tool costs hundreds of millions of dollars. Unsurprisingly, only the largest and most well-funded companies can compete in the semiconductor manufacturing industry. EUV is only feasible for high-volume applications. This work focuses on developing materials for an alternative optical lithography using visible wavelengths of light to produce small features. Visible light is much easier and safer to use. These features ease costs significantly and will enable small companies to participate once the technique is established and scaled for production.

## 1.2 Multiphoton absorption polymerization (MAP)

EUV uses linear exposure to create features in a photoresist. In other words, a single photon of light is needed to initiate a chemical reaction in the photoresist. With linear exposure, all of the photoinitiators exposed to the light can become excited. However, in MAP, 2 or more photons are required to excite a photoinitiator. For 2-photon polymerization to occur, two photons must be absorbed by the photoinitiator simultaneously. Only a small area at the focal region of an ultrafast beam has enough intensity to deliver two simultaneous photons for excitation, and the remainder of the molecules along the beam path are unaffected. This intensity dependence means that the photochemical reaction initiated by the light is confined to the focus of the beam and can be controlled in three dimensions by moving the focus of the beam with respect to the photoresist, or vice versa.

### 1.3 Two-color lithography (2CL)

2CL builds on the intensity dependence of MAP, but adds a second beam to reduce feature sizes further. Our work uses radical-initiated photopolymerization. Polymerization happens when a photoinitiator is excited to a chemically active state, breaking into radicals that initiate polymerization of the acrylate monomers. The deactivation beam inhibits polymerization by promoting the photoinitiators into an inactive state that does not produce radicals. Those photoinitiators then relax to the ground state without initiating polymerization. This polymerization inhibition is called deactivation. The deactivation beam can be shaped so that it has a dark spot in the middle. When the two beams are overlapped, all photoinitiators are irradiated, but only the molecules in the dark spot of the deactivation beam will produce radicals to initiate polymerization. The photoinitiators in the bright area of the deactivation beam are promoted to the inactive state before radicals can form.

### 1.4 Three-color lithography (3CL)

3CL builds further on 2CL by using three spatially overlapped beams instead of two as shown in Figure 1.1. Two beams are combined to polymerize, and the third beam deactivates. In this case, polymerization and deactivation happen from different energy states of the photoinitiator. Separating these two processes results in less unwanted polymerization buildup between features, because undeactivated photoinitiators do not produce radicals. We found that isopropylthioxanthone (ITX) can exhibit 3-color behavior because this molecule has a long-lived, chemically inactive excited state. We separated the 2- and 4-ITX isomers, and found that 4-ITX

has a higher polymerization threshold compared to 2-ITX as shown in Table 1. Even a trace of 2-ITX in the 4-ITX analytical standard significantly reduced the polymerization threshold when using 445 nm, continuous wave (CW) excitation. This surprising result led us to understand that the electronic environment of the photoinitiator can cause significant differences in polymerization behavior. Once we observed 3CL behavior in 4-ITX, we proceeded to make thin films to see if we could further reduce feature sizes in this manner. Observations in thin films reaffirmed that small changes in the material around the photoinitiator can have profound effects on polymerization and deactivation behaviors by shifting the molecule's energy states.

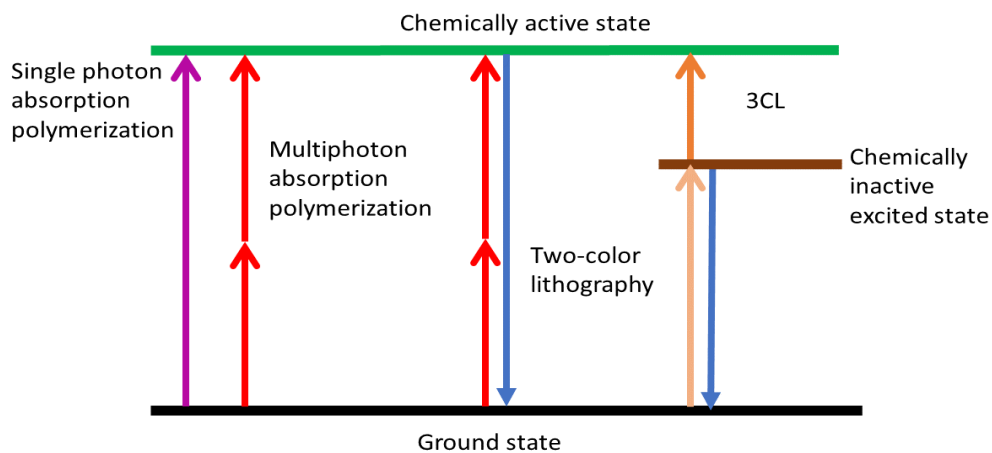


Figure 1.1 Simplified schematic of 3CL.

Table 1.1 Polymerizaion thresholds

One and Two Beam Polymerization			
Sample in SR444	800nm ML (mW)	445 nm CW (mW)	800 nm + 445 nm CW (mW)
2 – ITX analytical standard 1.5 wt%	7.6	2.96	6
4 – ITX analytical standard 1.5 wt%	9.6	3.50	6
4 – ITX prep-TLC 1.5 wt%	10.3	12.6	6.14

### 1.5 Parts of the document

This thesis is a collection of papers on our work with ITX using 3CL. Many experiments were performed using a microscope, as described in Chapter 2. Chapter 3 discusses a novel method of measuring nonlinearity of candidate photoinitiators. Chapter 4 examines ITX in detail. Chapter 5 discusses the synthesis and characterization of the ITX thin films. Chapter 6 reviews some of the effects we observed in thin films that may not be seen in thick films.

## Chapter 2 : Experimental setup

### 2.1 Optical Setup

Polymerization is performed on a Zeiss Axiovert 100 microscope with a tunable Ti:sapphire oscillator from Coherent, Mira 900-F. The laser can be tuned between 700 and 900 nm and has a pulse duration of 150 fs and a repetition rate of 76 MHz. The beam is collimated and spatially filtered with lenses and pinholes. The power is controlled with a polarizer and a half-wave plate. A small percentage of the beam is reflected by a plain glass coverslip into a photodiode to observe the power carefully using a lock-in amplifier. The beam is positioned precisely with galvanometric scanning mirrors and reflected into the microscope using dichroic mirrors. The beam is expanded to 8 mm to fill the back aperture of a 1.45 NA, 100 $\times$ , oil-immersion, Zeiss  $\alpha$  Plan-Fluar objective. The objective tightly focuses the beam into a mounted photoresist sample. The photoresist sample is moved using a translation stage (Ludl) for coarse positioning. For fine positioning, a 3-axis piezoelectric stage (Physik Instrumente) with a 250  $\mu$ m range in three dimensions, and with sub-nanometer resolution, is attached to the Ludl stage. The focus of the beam with respect to the photoresist sample can be moved by changing the scanning mirrors in the  $x$  and  $y$  directions. The beam is focused on the sample in the  $z$  direction by moving the objective towards or away from the sample and or by adjusting the piezo stage.

Polymerization changes the refractive index of the photoresist. Therefore, polymerization can be observed directly using a CCD camera attached to the microscope. Before polymerization, the refractive index of the photoresist closely

matches the refractive indices of the glass coverslip and the immersion oil. As the monomers polymerize, the refractive index increases and the polymerized features appear as dark lines through the CCD camera. Polymerization inhibition experiments use two beams, one for initiation, as described above, and another for deactivation. A second Coherent Mira 900-F tunable Ti:sapphire oscillator is used for deactivation. The beam is similarly collimated, the power is controlled with a polarizer and a half-wave plate and a photodiode is used to observe the power. An additional half-wave plate is used so that the polarization of the second beam is orthogonal to that of the first laser beam, and the two beams are combined by a beam cube before entering the microscope.

A radial-polarization converter from ARCoOptix is used to convert the linearly polarized beam into a beam that has a continuous radial polarization distribution. This polarization converter is used to shape the deactivation beam into a donut-shaped focal point that can be focused through the objective. The shaped deactivation beam selectively deactivates molecules and decreases the size of the polymerized feature. To take full advantage of the radially-polarized deactivation beam, the two beams must be well overlapped in all three dimensions. The beams are aligned in a photoresist sample with both beams mode-locked (ML). Polymerization is observed in the CCD camera and the power of both beams is adjusted to just below the polymerization threshold. The scanning mirrors are changed to move the first beam in the  $x$  and  $y$  directions until the first beam overlaps the second, and polymerization is observed. The overlap in the  $z$  direction is adjusted as described in Appendix I.

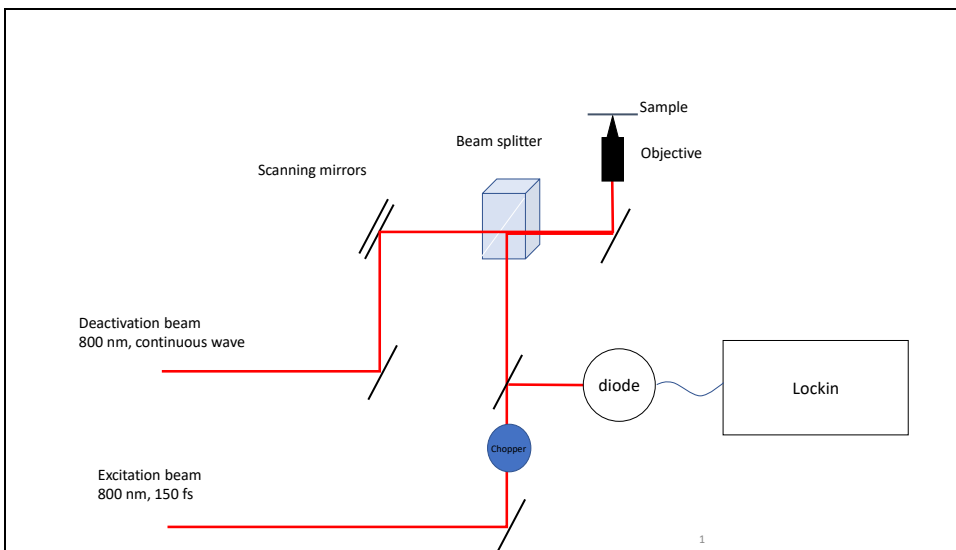


Figure 2.1 Simplified schematic of the polymerization and deactivation beams.

## 2.2 Preparation of thick-film samples

Most samples used for this work are solutions of photoinitiators in a mixture of multi-acrylate monomers. Although the goal of this project is to use thin films, many threshold and other preliminary experiments were performed in thick films. This section will describe how thick films are made, whereas Chapter 5 discusses thin films.

### 2.21 Substrates

For thick-film samples, polymerization occurs on an acrylated glass coverslip. The glass coverslips are acrylated to promote polymer adhesion to the substrate, such that features can be characterized after unpolymerized monomer is developed away. The coverslips are first cleaned and de-greased. The substrates are sonicated for 3 minutes each time in deionized water to remove dust, then in acetone to remove most organic impurities, then again in water, as acetone can dry too fast and leave a residue behind. After drying in a 100 °C oven for 1 h, the substrates are cleaned in O<sub>2</sub> plasma

at 250 mTorr for 3 min, exposing silanol groups to increase reactivity for the acrylation. The coverslips soak in a 2% solution of acrylate in ethanol and 10% water overnight. The coverslips are then rinsed in ethanol for 1 h, and left to dry at room temperature.

## 2.22 Photoresist

The monomer mixture is made first. If one of the acrylate monomers is a solid at room temperature, the solid monomer is weighed out into a 20 mL vial and mixed in a FlackTek SpeedMixer™ model DAC 330-100 L for 5 min at 1700 RPM and then heated in a 100 °C oven for 5 min. Mixing in this mixer minimizes the need to heat the monomers. The sample is mixed and heated again until the waxy monomer becomes liquid and translucent. Once the solid monomer is liquified, the other monomers are weighed directly into the vial and mixed. Once the monomers are codissolved, the photoinitiator is weighed out in a separate vial and the monomer mixture is added. The sample is mixed and heated again until the photoinitiator is completely dissolved. The solution is then filtered through a nylon syringe filter with a 0.45 micron pore size.

## 2.23 Microscope samples

If the sample is to be used as a thick film, a drop of photoresist is placed between coverslips to be mounted into the microscope. A microscope slide is cut to size, and a coverslip is taped onto the slide. The thickness of the adhesive tape dictates the thickness of the film. The tape is placed carefully to avoid air bubbles under the tape, as such imperfections tilt the substrate on which polymerization

occurs. The photoresist is applied with a wooden stick. The stick is inserted into the material deep enough to get a drop of material, but not so deep that the stick comes in contact with the bottom of the vial, to reduce the risk of picking up polymerized or crystallized precipitates. The small amount of material is slowly rolled on the coverslip with the wooden stick to avoid creating bubbles in the material. An acrylated coverslip is marked and gently lowered on top of the drop of material. The acrylated coverslip is taped into position with minimal pressure, as too much pressure can also create bubbles in the material when the coverslip springs back up.

### **Chapter 3 : *In situ measurement of the effective nonlinear absorption order in multiphoton photoresists***

Based on a paper by Zuleykhan Tomova, Nikolaos Liaros, Sandra A. Gutierrez Razo, Steven M. Wolf, and John T. Fourkas. John Fourkas conceived of the method and directed the project. Measurements were performed by Zulya Tomova and Nikos Liaros. I made the samples and confirmed the 2-BIT measurements. Steven Wolf collected absorption spectra.

This chapter discusses a method developed for the simple measurement of the nonlinear absorption of photoinitiators in photoresist. This method quickly became an invaluable tool in our laboratory for assessing monomers and photoinitiators, not only in the formulation of a favorable photoresist, but also yielding many surprising results that guided our research. Knowledge of the order of the effective nonlinear absorption in multiphoton photoresists is a key element in the development of improved materials for multiphoton absorption polymerization (MAP). The direct measurement of this nonlinearity has proven challenging. A new technique, called 2-beam initiation threshold (2-BIT) spectroscopy is presented. This technique allows for the unambiguous, *in situ* measurement of the order of the effective nonlinear absorption using a simple optical arrangement that can be employed with virtually any MAP setup. This technique is benchmarked using three common commercial photoinitiators that have been used previously in MAP, and one common dye that acts as a photoinitiator. The linear absorption spectrum is demonstrated to be a poor predictor of the effective order of nonlinear absorption at a given wavelength. Surprisingly, for two of these initiators, the effective nonlinear absorption process is

dominated by 3-photon absorption in the 800 nm wavelength range, suggesting that 2-BIT is a valuable means of identifying initiators that can improve the resolution of MAP.

### 3.1 Introduction

Since multiphoton absorption polymerization (MAP) was first demonstrated in 1997,<sup>2</sup> the use of this technique in the microfabrication of 3D structures has grown exponentially.<sup>3-6</sup> In MAP, multiphoton absorption is used to expose a negative-tone photoresist exclusively within the focal volume of an ultrafast laser beam that is focused through a high-numerical-aperture objective. By moving the focal point relative to the photoresist, highly complex structures can be created, with feature sizes down to the sub-100-nm range.

The ever-increasing applications of MAP have driven the sustained development of new materials for this technology. One focus has been on the creation of photoinitiators that have improved multiphoton absorption cross sections (MACS<sup>7</sup>). However, the measurement of MACS to states that undergo irreversible photochemistry is challenging. Early attempts worked under the assumption that the MACS for fluorescence mirrors that for photochemistry.<sup>8</sup> Although this assumption is often reasonable, there is no guarantee that it is correct in any given system. Even if the excitation of fluorescence is a 2-photon process at a given wavelength, initiation of photochemistry need not be, as has been demonstrated recently for 7-diethylamino-3-thenoylcoumarin.<sup>9</sup> More generally, at a given wavelength, the order of the effective nonlinear optical absorption for MAP, i.e. the nonlinear absorption that leads to polymerization, need not match the dominant order of nonlinear absorption at the

same wavelength as measured with techniques such as Z-scan.<sup>10</sup> It is therefore essential to know the effective order of nonlinear absorption if one wishes to determine the MACS at the correct order.

With this problem in mind, a number of recent studies have focused on determining the effective order of the nonlinear absorption of photoinitiators in situ by measuring photopolymerization. In one commonly used technique, the feature size is measured as a function of fabrication velocity for a range of different average laser powers.<sup>5,11</sup> However, Fischer et al. pointed out that this method cannot unambiguously determine the order of nonlinear absorption in a photoresist,<sup>12</sup> and developed an alternative technique in which the exposure threshold is measured as a function of pulse energy at different pulse repetition rates.<sup>12</sup> Their method can provide detailed information on the processes that contribute to MAP at different pulse intensities. The same group also introduced a technique in which the effective order of nonlinear absorption is determined by measuring the polymerization threshold at a fixed repetition rate but different exposure times.<sup>13</sup> However, both of these techniques require fast, nonmechanical shutters and high power (multiwatt) oscillators, which are not available in many laboratories in which MAP is performed.

Here, we introduce a simple and complementary method for determining the effective order of nonlinear absorption processes in photoresists. 2-BIT can be implemented with the addition of a few simple optics, can be performed with a single, low-power ultrafast oscillator, and allows for the determination of the order of the effective nonlinear absorption using only a single repetition rate. 2-BIT is therefore amenable to use in virtually any laboratory that performs MAP.

## 3.2 Theory

In MAP, multiphoton excitation of a photoinitiator leads to local crosslinking of a negative-tone photoresist. Photoresists have highly nonlinear exposure curves, and become insoluble above a threshold exposure dose. In principle, this threshold is reached when a specific density of photoinitiators has been excited. However, the use of ultrafast pulses in MAP brings other time scales into play. On the one hand, ultrafast pulses are typically much shorter than the time scales on which photoinitiators undergo photochemistry.<sup>14</sup> On the other hand, due to the small size of the region irradiated at any given time in MAP, the diffusion of heat or species such as radicals or quenchers can play an important role in determining the threshold exposure. Diffusive effects leading to termination become important when, due either to a low pulse intensity or a low repetition rate, the exposure time at a given spot is relatively long.<sup>13</sup> Because of these effects and others, it is often desirable to be able to determine the order of the effective nonlinear absorption of a photoresist at a fixed repetition rate.

If the exposure conditions are comfortably between these two extremes, then overcoming the exposure threshold can safely be equated with generating a specific density of photoinitiators that have been excited at some time in the exposure window. This condition is generally met at a typical oscillator repetition rate at a reasonable fabrication velocity (e.g., tens to hundreds of  $\mu\text{m/s}$ ). It is essential that the repetition time be much longer than the excited state lifetime of the photoinitiator, to prevent any effects of excited-state absorption. Typical radical photoinitiators generate radicals on a 100-ps time scale,<sup>14</sup> which is 2 orders of magnitude faster than

a typical repetition time. The radicals that are formed do not absorb the laser light, and so are unaffected by subsequent pulses. It is also important that the repetition period is much shorter than the termination time scale, so that the effects of the laser pulses are cumulative. In a typical photoresist, termination becomes important on time scales of  $100 \mu\text{s}$  or more,<sup>13</sup> which is much longer than the typical dwell time on a given spot. If a fixed duration for the exposure window ( $t_w$ ) and a fixed repetition rate for the ultrafast pulses ( $\nu_{\text{pulse}}$ ) are chosen, then the minimum average power for which crosslinking is observed can be defined as  $P_{\text{th}}(t_w, \nu_{\text{pulse}})$ .

Consider the case in which exposure occurs via two independent trains of pulses that are identical in wavelength, duration, and repetition rate, but not in intensity. For simplicity, assume that these pulse trains are timed such that pulses arrive at the sample at repetition rate  $2\nu_{\text{pulse}}$ . So long as  $\nu_{\text{pulse}}$  and  $2\nu_{\text{pulse}}$  are (1) small enough that there is plenty of time for excited photoinitiators to undergo chemistry between pulses and (2) large enough that diffusive effects are unimportant between pulses, the exposure threshold will be reached when

$$P_1^n + P_2^n = P_{\text{th}}^n. \quad (3.1)$$

Here, the subscript denotes the pulse train and  $n$  denotes the number of photons involved in the transition to the excited state that is the gateway to crosslinking. This equation can be recast in terms of normalized powers  $\bar{P}_i = P_i/P_{\text{th}}$  as

$$\bar{P}_2 = \sqrt[n]{1 - \bar{P}_1^n}. \quad (3.2)$$

Thus, by measuring the value of  $\bar{P}_2$  required to reach the threshold exposure for different values of  $\bar{P}_1$ ,  $n$  can be determined directly. In practice, the power of each beam is normalized to the threshold power for polymerization using that beam, to

correct for any minor differences in properties such as beam size, pulse length, or focal volume.

### 3.3 Experimental section

#### 3.31 Optical setup

A tunable, femtosecond Ti:sapphire oscillator (Coherent Mira 900-F) was used as the excitation source. The repetition rate of the laser was 76 MHz, and the pulse duration was approximately 150 fs. The beam was spatially filtered and then split into two roughly equal parts. Each beam was passed through a separate variable beam expander to allow for adjustment of the beam size at the back aperture of the microscope objective.

The average power of each beam was adjusted using a motorized half-wave plate and a Glan–Taylor polarizer. To increase the accuracy of the laser power measurement, a small portion of each beam was reflected using a 95:5 beam splitter and then passed through neutral-density filters to lower its intensity. The beam was chopped, and its power was measured using a calibrated Si photodiode, the output of which was sent to a lock-in amplifier.

The two beams were combined through a polarizing beam cube and made collinear. The lengths of the two beam paths were adjusted so that consecutive pulses arrived at the sample with roughly equally spaced timings, giving an effective repetition rate of 152 MHz. The timing between the pulse trains was adjusted using a fast photodiode and an oscilloscope, which is sufficiently precise for performing 2-BIT experiments. The beams were sent through the reflected-light illumination port of an inverted microscope and were focused through a 100 $\times$ , 1.45 NA oil-immersion

objective, the back aperture of which was overfilled. Samples were mounted on a 3-axis piezoelectric stage for fine sample positioning in all dimensions. The piezo stage was attached to a motor-driven stage for coarse sample positioning. The movement of the sample stage was controlled using LabVIEW programs, and fabrication was followed in real time using a CCD camera and a monitor. To ensure that the two focused beams had identical focal volumes that were completely overlapped at the sample, gold nanoparticles were deposited on a cover slip and multiphoton absorption induced luminescence<sup>15</sup> was used to determine the position and shape of the point-spread function of each beam. Special attention was paid to ensure that the two beams had exactly the same diameter and divergence at the entrance pupil of the microscope objective, such that beams of the same average power would also have the same on-axis intensity. However, we note that due to the normalization of the power thresholds, 2-BIT measurements are tolerant to modest misalignments of the beams.

### 3.32 Sample preparation

The photoresist samples studied were created by adding 0.1–2.0 wt% photoinitiator to a base resist composed of 45 wt% tris (2-hydroxy ethyl) isocyanurate triacrylate and 55 wt% dipentaerythritol pentaacrylate. The photoinitiators examined are shown in Figure 3.1, and included Lucirin TPO-L, Irgacure 369, Irgacure 651, and crystal violet lactone. All samples were blended at 2500 rpm for 5 min using a vortex mixer. After mixing, a drop of the photoresist was placed on a functionalized, #1 glass coverslip. The functionalized coverslips were prepared by exposure to oxygen plasma for about 4 min, immersion in a solution of 93 vol% ethanol, 5 vol% distilled

water and 2 wt% (3-acryloxypropyl) trimethoxysilane (Gelest) for 14 h, rinsing in ethanol for 1 h, and drying at 95 °C for 1 h.

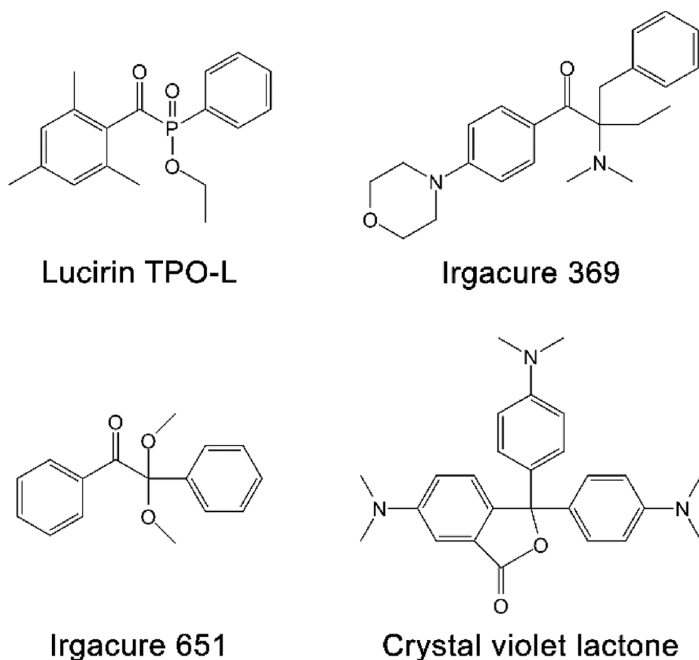


Figure 3.1 Photoinitiators studied in this chapter.

### 3.33 2-BIT measurements

The first step in a 2-BIT measurement is determination of the polymerization threshold powers of each laser beam independently. These thresholds were measured by creating sets of lines at a constant distance above the coverslip surface at a stage velocity of 20  $\mu\text{m/s}$ . The minimum average power at which fabricated lines were observed was then determined visually on the monitor. This is a well established, robust, and reliable method of determining the threshold for MAP<sup>9,16</sup> that we employ here due to its ease of use, but 2-BIT can be used in concert with any method of measuring the threshold exposure. Although the threshold exposure measured may differ for different optical systems, the normalization procedure described above corrects for any such differences. The power of the first laser beam was then lowered

to a set of fixed values below the threshold. For each of the fixed values of  $P_1$ , the corresponding minimum value of the power of the second beam,  $P_2$ , for which polymerization was observed at the same stage velocity was determined. The values of  $P_1$  were chosen so that a representative range of values of  $P_2$  was measured, such that the plot of  $\bar{P}_2$  vs.  $\bar{P}_1$  could be fit reliably. At least five measurements were made for each value of  $P_1$  so that reproducibility could be quantified.

### 3.4 Results and discussion

Lucirin TPO-L and Irgacure 369 are two commercial photoinitiators that are known to be effective materials for MAP.<sup>16,17</sup> Shown in Figure 3.2 are 2-BIT data for photoresists containing Lucirin TPO-L (panel A) and Irgacure 369 (panel B). In each case the laser was tuned to a center wavelength of 800 nm. The best-fit exponential  $n$  was determined in each case by nonlinear least-squares fitting of the 2-BIT data to Equation 3.1

Although the absorption spectrum of the initiators may be slightly different in the photoresist, spectra obtained in methanol give a semiquantitative measure of the positions of the absorption bands. Lucirin TPO-L has modest absorption at 400 nm, and strong absorption at 267 nm (Figure 3.2A, inset). The single-beam threshold power for this initiator was  $5.9 \pm 0.2$  mW, and the best-fit exponent to the 2-BIT data is  $2.0 \pm 0.1$  mW. Despite the strong linear absorption at the effective 3-photon wavelength, this material acts quadratically at 800 nm, as has been suggested previously.<sup>16,18</sup> Irgacure 369 has a weak absorption tail at 400 nm and considerably stronger absorption at 267 nm (Figure 3.2B inset). The single-beam threshold power for this initiator was  $6.6 \pm 0.4$  mW, and the best fit 2-BIT exponent for this material is

$2.0 \pm 0.2$  mW at 800 nm. It is evident from the 2-BIT data that the effective nonlinearity in this material is primarily a 2-photon absorption at 800 nm, in agreement with previous measurements.<sup>8,12,19</sup> Thus, as expected, both materials form radicals via 2-photon absorption at 800 nm. It is difficult to predict the nonlinearity in these materials from the absorption spectrum alone, due to the different orders of nonlinearity for 2- and 3-photon absorption in conjunction with the potential influence of selection rules in multiphoton transitions.

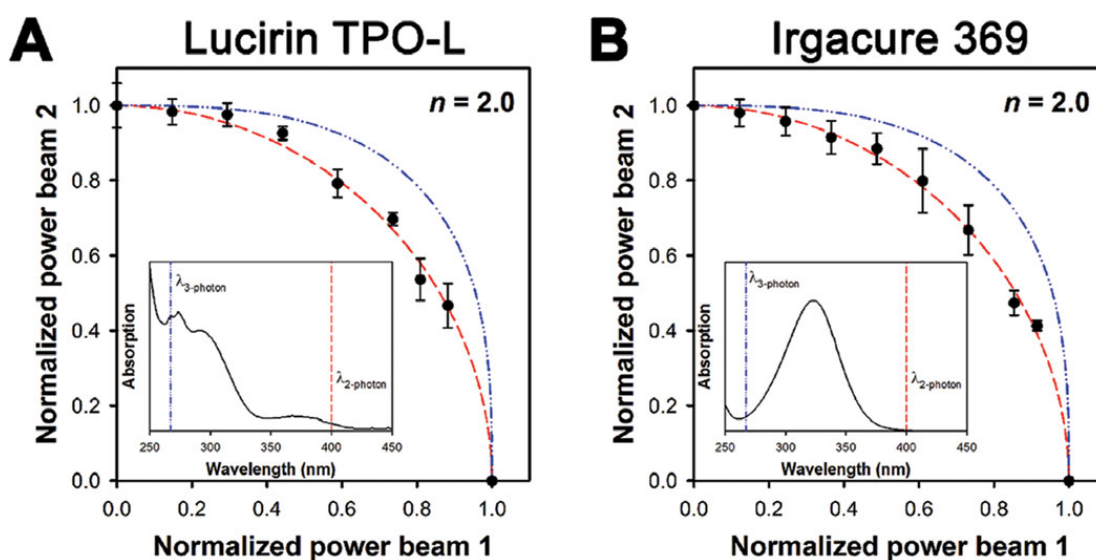


Figure 3.2 2-BIT data for photorezists containing (A) 1.0 wt% Lucirin TPO-L and (B) 0.1 wt% Irgacure 369. The red curves are the best fits to Equation 3.2. The blue curves are the result that would be expected for 3-photon absorption as a reference. The insets show the absorption spectra of these photoinitiators in methanol, with the effective wavelengths for 2-photon and 3-photon absorption indicated as red and blue lines, respectively. The error bars in this and the ensuing figure are based on standard deviations from multiple measurements.

Irgacure 651 is another commercial photoinitiator that has also been used for MAP.<sup>20</sup> The 2-BIT data for this initiator are shown in Figure 3.2A for excitation at a center wavelength of 830 nm. As can be seen from the inset, this material has weak absorption at 415 nm and stronger absorption at 277 nm. The single-beam threshold power for this initiator was  $17.6 \pm 0.9$  mW, and the best fit exponent for the 2-BIT data is  $3.1 \pm 0.1$  mW, indicating that polymerization is a 3-photon process for this

initiator at this wavelength. This result again underscores the fact that the order of the effective nonlinear absorption cannot be determined readily from the linear absorption spectrum alone. It is possible, for instance, that there is significant 2-photon absorption to the origin of the lowest singlet excited state in this molecule, but that this state does not generate radicals. Additional measurements (data not shown) indicate that at shorter wavelengths, this initiator does transition to initiating via 2-photon absorption. Crystal violet lactone is not typically used as a photoinitiator, but is one of many common dyes<sup>14</sup> that can produce radicals, and therefore act as a photoinitiator, under multiphoton excitation. The 2-BIT data for a photoresist containing this material for 800 nm excitation are shown in Figure 3B. As can be seen from the absorption spectrum in the inset of Figure 3B, this material has weak absorption at 400 nm and strong absorption at 267 nm. In this case, the single-beam threshold power was  $5.2 \pm 0.4$  mW. The 2-BIT data are best fit with an exponent of  $3.0 \pm 0.1$  mW, indicating that the dominant effective nonlinear absorption is 3-photon at 800 nm.

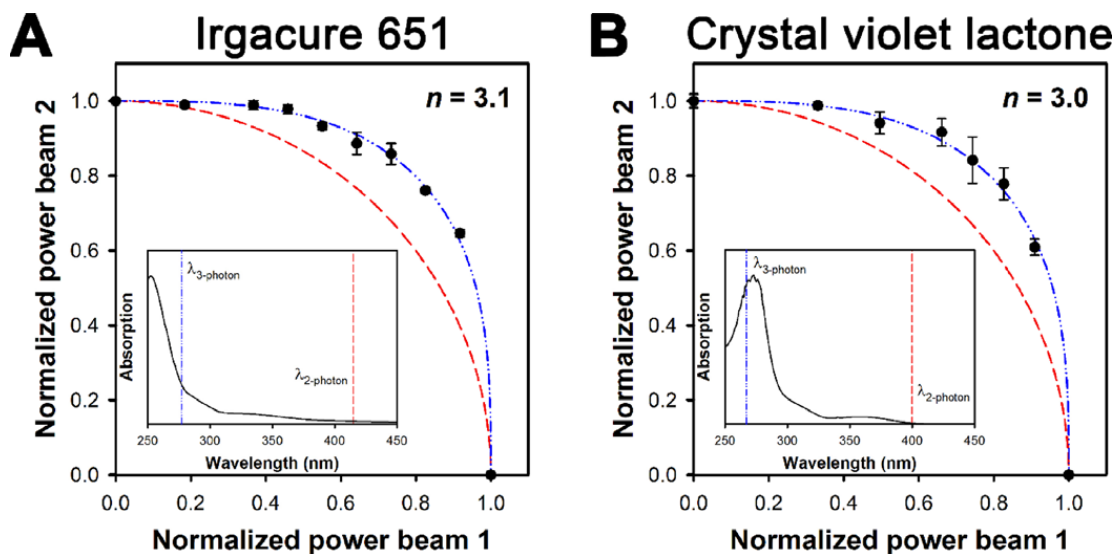


Figure 3.3 2-BIT data for photoresists containing (A) 1.0 wt% Irgacure 651 and (B) 2% crystal violet lactone. The blue curves are the best fits to Equation 3.2. The red curves are the results that would be expected for 2-photon absorption as a reference. The insets have the same meaning as in Figure 3.2.

It is clear from our results that one cannot predict the order of the effective nonlinear absorption required for photoinitiation directly from a linear or nonlinear absorption spectrum. Even when the 2-photon absorption spectrum has been measured using another technique, such as fluorescence, it may not match the polymerization action spectrum. Furthermore, MAP photoinitiators that have been assumed to operate via 2-photon absorption near 800 nm may actually operate via 3-photon absorption. Identification of such photoinitiators may make it possible to improve the resolution of MAP.

### 3.5 Conclusions

2-BIT is a simple and effective method for the in situ measurement of the order of the effective nonlinear absorption in multiphoton photoresists, and as such can be an important element of the development of new materials that extend the capabilities of MAP. 2-BIT relies on the use of a single oscillator of fixed repetition rate, and so can

be set up easily in virtually any laboratory in which MAP is performed. This technique can be used with any type of MAP photoresist, and can be implemented with any of a wide range of means for determining the initiation threshold of a photoresist, including monitoring of lines or voxels during fabrication using optical or spectroscopic methods, or postfabrication using methods such as optical, electron, and atomic force microscopy. 2-BIT allows the order of the effective nonlinear absorption of a photoresist to be determined without having to use devices for rapid beam modulation, and measurements can be performed at any desired repetition rate. Variations of this technique can be used to make *in situ* measurements of the order of the effective optical nonlinearity (and therefore the multiphoton action cross section, as opposed to the multiphoton absorption cross section) not just in photoresists, but in any sort of system in which nonlinear absorption causes a property to reach a measurable threshold. With knowledge of the other relevant parameters, it will further be possible to use 2-BIT data to convert the multiphoton action cross section into a multiphoton absorption cross section. 2-BIT therefore promises to be a powerful means of elucidating the photochemical and photophysical details of complex multiphoton processes through, for instance, comparison with nonlinear absorption data.

## **Chapter 4 : Elucidating complex triplet-state dynamics in the model system isopropylthioxanthone**

Based on the paper by Nikolaos Liaros, Sandra A. Gutierrez Razo, Matthew D. Thum, Hannah M. Ogden, Andrea N. Zeppuhar, Steven Wolf, Tommaso Baldacchini, Matthew J. Kelley, John S. Petersen, Daniel E. Falvey, Amy S. Mullin, and John T. Fourkas. N.L. and J.T.F. conceived the project. N.L. implemented and performed the 2-BA and multiphoton luminescence deactivation experiments and analyzed the data. I prepared the samples for these measurements. N.L and I performed the multiphoton absorption polymerization experiments and characterized their results using SEM measurements. J.T.F. supervised this portion of the research. H.M.O. performed the in-situ monitoring of exposure and deactivation experiments; A.S.M. supervised this portion of the research. M.D.T., A.N.Z., and S.W. performed the microsecond transient spectroscopy and DFT calculations; D.E.F. supervised this portion of the research. T.M. and M.J.K. performed the ultrafast transient spectroscopy measurements. J.T.F. performed the kinetic modeling. J.S.P. provided expertise and feedback. N. L. and J.T.F. drafted the manuscript. All authors discussed the results and edited the manuscript. J.T.F. supervised the project.

### 4.1 Abstract

We introduce techniques for probing the dynamics of triplet states. We employ these tools, along with conventional techniques, to develop a detailed understanding of a complex chemical system: a negative-tone, radical photoresist for multiphoton absorption polymerization in which isopropylthioxanthone (ITX) is the photoinitiator.

This work reveals that the same color of light used for the 2-photon excitation of ITX, leading to population of the triplet manifold through intersystem crossing, also depletes this triplet population via linear absorption followed by reverse intersystem crossing (RISC). Using spectroscopic tools and kinetic modeling, we identify the reactive triplet state and a non-reactive reservoir triplet state. We present compelling evidence that the deactivation channel involves RISC from an excited triplet state to a highly vibrationally excited level of the electronic ground state. The work described here offers the enticing possibility of understanding, and ultimately controlling, the photochemistry and photophysics of a broad range of triplet processes.

## 4.2 Introduction

The vast majority of stable molecules have singlet ground states.<sup>21</sup> When such a molecule absorbs light, one electron is promoted to a higher, unoccupied orbital. Because electronic transitions between states of different multiplicities are formally forbidden, the excited electronic state in such a transition generally must also be a singlet.<sup>22</sup> However, spin mixing due to weak spin-orbit coupling or hyperfine interactions can lead to a subsequent transition from the singlet to an optically “dark” triplet state, in a process known as intersystem crossing (ISC). Because electronic wave functions must be antisymmetric, the unpaired electrons in a triplet state cannot be in the same place at the same time. Thus, the triplet state for a given electronic configuration virtually always has a lower energy than the corresponding singlet excited state. The energy gap between the corresponding singlet and triplet states is usually well above thermal energy at room temperature. Thermally activated reverse intersystem crossing (RISC) from the lowest triplet state to the first excited singlet

state has a low statistical probability when the energy gap is of this magnitude. The lowest triplet state can instead relax through processes such as phosphorescence (which also involves a spin flip, and therefore has an intrinsic lifetime that is considerably longer than that for a typical fluorescence transition), RISC to a vibrationally excited level of the ground singlet state, and collisional energy transfer. Alternatively, the triplet may undergo a chemical reaction. There is a growing recognition that the ability to control triplet dynamics could lead to substantial advances in many photochemical and photophysical applications. For instance, trapping of population in dark triplet states reduces the fluorescence quantum yield of molecules and materials, which is a major issue in applications such as the development of efficient organic light-emitting diodes<sup>23</sup> and luminescent carbon nanotubes.<sup>24</sup> Because of their metastable nature, triplet states can also be used to store energy; this capability plays an important role in applications such as the frequency upconversion of low-intensity light<sup>25</sup> and superresolved optical imaging.<sup>26</sup> Triplet states can also be harnessed for their chemical reactivity, as in photosensitization<sup>27</sup> and photopolymerization.<sup>28,29</sup>

Controlling triplet-state dynamics is a challenging problem. Any scheme for control must balance the influence of unimolecular phenomena that include ISC and RISC,<sup>30</sup> heavy-atom effects,<sup>31</sup> phosphorescence,<sup>32</sup> triplet absorption,<sup>33</sup> thermally activated delayed fluorescence,<sup>34</sup> and even coupling to photonic states in a cavity.<sup>35</sup> Bimolecular processes, such as triplet quenching,<sup>36</sup> triplet-triplet annihilation,<sup>37</sup> and singlet fission into two triplets,<sup>38</sup> can also influence triplet dynamics. Developing a holistic understanding that encompasses such phenomena requires not only

knowledge of the energies of both the singlet and triplet states of molecules, but also of the couplings among these states.

Laser spectroscopy has been a crucial tool for probing the rich photochemistry and photophysics of triplet states, and has provided a platform for fundamental studies on molecular electronic structure,<sup>39</sup> molecular reactions,<sup>40</sup> and the dynamics of electronic transitions.<sup>41</sup> Despite considerable progress, the study of complex triplet-state dynamics remains challenging, and triplet electronic and spin properties are areas of intense research. Many triplet-associated phenomena are “dark,” and as such, probing the nature of these processes often requires the use of multiple experimental techniques.<sup>42</sup> Furthermore, the growing interest in multiphoton methods and applications in complex environments requires triplet probing methods that extend beyond the classical tool kit of phosphorescence, transient absorption, and electron paramagnetic resonance.

Spectroscopic tools that can probe triplet electronic transitions and dynamics in complex systems are critical for advancing the ability to control triplet states. Here, we introduce several such techniques, which we use in combination with existing methods to elucidate the rich triplet dynamics of a molecular system. As a representative system, we chose isopropylthioxanthone (ITX). Thioxanthenes exhibit complex photophysics because their first two singlet excited states, one ( $\pi,\pi^*$ ) and one ( $n,\pi^*$ ), are quite close in energy, and in fact have an ordering that depends on the solvent<sup>43,44</sup> The same situation holds for the two lowest triplet states,<sup>45,46</sup> for which again one is ( $\pi,\pi^*$ ) and one is ( $n,\pi^*$ ).

One reason for our particular interest in ITX stems from the fact that this substance is a photoinitiator that can be used in multiphoton absorption polymerization (MAP).<sup>47,48</sup> MAP has attracted broad attention as a method for 3D photolithography at the nanoscale.<sup>4,49-51</sup> In its simplest implementation, MAP is performed in a negative-tone photoresist incorporating a radical photoinitiator that can be excited via the simultaneous absorption of two or more photons. Owing to the nonlinear optical nature of such excitation, MAP allows for the creation of lithographic features in the 100 nm size range using visible, or even near-infrared, light.

Outstanding resolution has been achieved in MAP by adapting approaches<sup>52-54</sup> from super-resolved fluorescence microscopy. In these advanced approaches to MAP, a negative tone photoresist is excited using one beam of light and deactivated using a second beam.<sup>55-58</sup> By appropriate spatial shaping of these two beams, it is possible to improve both the feature size and resolution in MAP. Different mechanisms have been demonstrated for deactivation, and we will denote this general class of techniques as two-color lithography (2CL).<sup>59</sup> A second reason for our particular interest is that ITX has been shown to be a useful initiator for 2CL.<sup>13,28,29,48,60,61</sup> Even though ITX is a Type II photoinitiator, this compound has been demonstrated to be able to initiate crosslinking of acrylates upon multiphoton excitation with pulsed 800 nm light in the absence of a coinitiator.<sup>48</sup> This photochemistry has been shown to be suppressed by concurrent irradiation with a continuous-wave (CW) laser at either 532 nm or 630 nm.<sup>29,47</sup> It has been established that the mechanism of photodeactivation in ITX at these wavelengths is not stimulated emission.<sup>62</sup> To date, there has been no

clear evidence regarding the details of the deactivation process, although it has been proposed that triplet states are involved.<sup>28,29,60</sup>

Here, we demonstrate conclusively that excitation in ITX from the ground state to the first excited singlet state at wavelengths near 800 nm takes place via 2-photon absorption (2PA), even though the apparent number of photons absorbed is higher.<sup>9</sup> This behavior arises from the fact that the light at the excitation wavelength can also drive deactivation of the triplet state. Thus, although a higher order of nonlinear absorption can lead to improved feature sizes in MAP, in ITX the apparent greater number of photons is detrimental to resolution. By employing a combination of new and conventional spectroscopic tools, and by studying ITX both in photoresists and in solvents with similar polarities to the photoresists, we identify the triplet states and specific dynamics that are involved in the excitation, deactivation, and radical photochemistry of ITX.

## 4.3 Results

### 4.3.1 Effective order of nonlinearity of ITX photoresists

ITX is generally considered to be a Type II photoinitiator, i.e., photoresists that use this material typically also include a coinitiator.<sup>63</sup> However, it has been demonstrated that in some acrylic resins ITX can be used without a coinitiator, in a Type I process.<sup>48</sup> Based on its absorption spectrum, ITX would appear likely to be excited by 2PA using light at wavelengths in the 800 nm range. However, experiments by Mueller et al. on a photoresist composed of ITX and pentaerythritol triacrylate (PETA) monomers suggested that excitation at 800 nm involves 4-photon

absorption.<sup>13</sup> Such remarkably efficient 4-photon polymerization would be highly advantageous for high-speed, high-resolution MAP fabrication.<sup>13</sup> In contrast, Z-scan experiments have indicated that ITX in a solvent can be excited by 2PA at wavelengths in the 800 nm region.<sup>64</sup> These results are not necessarily inconsistent, as promotion of an electron to the lowest excited singlet state of ITX might not lead to photopolymerization. On the other hand, the feature sizes reported for MAP for ITX-based photoresists with 800 nm excitation closely resemble what would be expected for 2PA. These seemingly contradictory results highlight the potential complexity of the determination of the true order of nonlinear absorption in multiphoton photoresists.

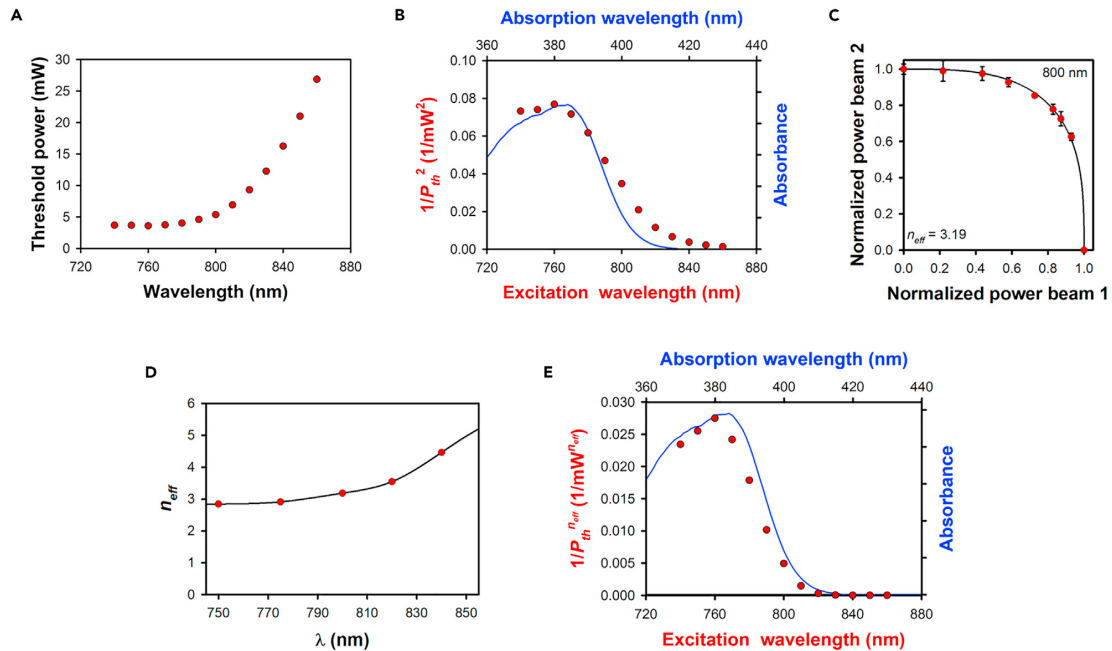


Figure 4.1 Multiphoton exposure of an ITX/PETA photoresist (A) Threshold average power for initiation of multiphoton absorption polymerization measured at wavelengths from 750 nm to 850 nm. (B) Polymerization action spectrum of the photoresist (symbols) and absorption spectrum of ITX in methanol (solid line). (C) Representative 2-BIT data obtained at 800 nm (symbols) with the best-fit exponent (solid line). The error bars represent  $\pm 1$  standard deviation, as determined by making multiple measurements. (D) Dependence of  $n_{eff}$  (symbols) on the excitation wavelength, with a cubic-spline fit (solid line). (E) Linearized polymerization action spectrum taking into account  $n_{eff}$  for each wavelength (symbols) and absorption spectrum of ITX in methanol (solid line).

Figure 4.1A shows the power threshold for MAP measured at wavelengths in the range of 750 – 850 nm in a photoresist composed of 1.5 wt% of ITX in PETA. The threshold power refers to the minimum power that is required to form a cross-linked polymer using MAP. The cross-linked polymer has a different refractive index than the unexposed photoresist, and so can be observed by means of optical microscopy during fabrication. The threshold was determined by creating sets of lines at a constant height above the substrate surface at a stage velocity of 20  $\mu\text{m/s}$ . The distance between adjacent lines was 2  $\mu\text{m}$ , which is large enough to avoid proximity effects. The threshold power,  $P_{\text{th}}$ , for which polymerized lines were formed was determined visually.<sup>16,65</sup>

An effective means of gaining insight into the order of nonlinearity in MAP is to determine the polymerization action spectrum, which is a plot of  $\overline{P}_{\text{th}}^{n_{\text{eff}}}$  as a function of the excitation wavelength, where  $n_{\text{eff}}$  is the effective order of nonlinear absorption.<sup>16</sup> Depicted in Figure 4.1B is a polymerization action spectrum calculated by assuming that  $n_{\text{eff}} = 2$ . The agreement between the polymerization action spectrum and the linear absorption spectrum of ITX at half the excitation wavelength is strong evidence that photoinitiation in this range of wavelengths is a 2-photon process. We measured the effective order of absorption,  $n_{\text{eff}}$ , as a function of excitation wavelength to explore the discrepancy between the actual order of nonlinear absorption, which is 2, and the higher value of the effective order of absorption reported previously.<sup>9</sup> We employed the 2-beam initiation threshold (2-BIT) method,<sup>66</sup> a type of 2-beam action (2-BA) spectroscopy,<sup>67,68</sup> to perform in situ measurements of  $n_{\text{eff}}$  in the ITX/PETA photoresist. In 2-BIT, two temporally interleaved, spatially

overlapped pulse trains are used to expose a multiphoton photoresist. Pairs of irradiances that together provide the threshold exposure are measured. Data obtained with this technique obey the relation

$$\bar{P}_1^{n_{eff}} + \bar{P}_2^{n_{eff}} = 1, \quad (4.1)$$

where the overbars indicate normalization of the average excitation power for each beam to the threshold power for that beam alone. A significant advantage of 2-BIT over other approaches for measuring the order of nonlinearity of photoresists is that important parameters that can change the measured value of  $n_{eff}$ , such as the exposure time and the repetition rate, are kept constant.<sup>69</sup>

Representative 2-BIT data for the ITX/PETA photoresist for 800 nm excitation are shown in Figure 4.1C. The best-fit  $n_{eff}$  for these data is  $3.19 \pm 0.05$ . The data were obtained at a stage velocity of 20  $\mu\text{m/s}$ . Although the value of  $P_{th}$  depends on the stage velocity, the measured value of  $n_{eff}$  was insensitive to velocity in the tested range of 10  $\mu\text{m/s}$  to 40  $\mu\text{m/s}$ . In Figure 4.1D, we plot  $n_{eff}$  as a function of the excitation wavelength. The corresponding 2-BIT data and fits at each wavelength are shown in Figure 4.2. As seen in Figure 4D,  $n_{eff}$  depends on the excitation wavelength, ranging from  $2.85 \pm 0.05$  at 750 nm to  $4.47 \pm 0.16$  at 840 nm. It is notable that the measured exponents take on non-integer values, which is often assumed to be indicative of mixed contributions from different orders.<sup>13,65,70</sup> However, it is not plausible that the average order of nonlinear absorption should change so radically over such a small range of excitation wavelengths, given the details of the linear absorption spectrum of ITX and the fact that higher-order absorption should be a considerably weaker process. We have previously introduced a method to determine

whether 2-BA data arise from a specific pair of orders of absorption.<sup>71</sup> The 2-BIT data for ITX do not fit well to either 2-photon plus 3-photon or 2-photon plus 4-photon absorption, as shown for the case of the 750 nm data in Figure 4.3.

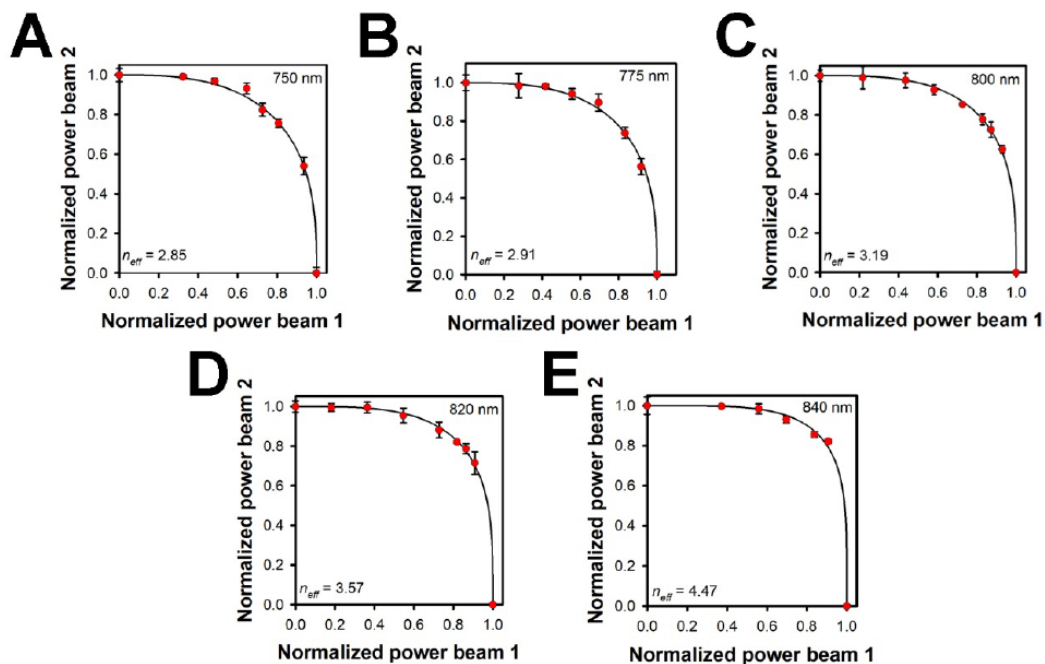


Figure 4.2 2-BIT data for a photoresist consisting of 1.5 wt% of ITX in PETA. Excitation was performed at (A) 750 nm; (B) 775 nm; (C) 800 nm; (D) 820 nm; and (E) 840 nm. The uncertainties in the  $n_{eff}$  values are  $\pm 0.05$  in (A),  $\pm 0.06$  in (B),  $\pm 0.03$  in (C),  $\pm 0.04$  in (D), and  $\pm 0.15$  in (E). The error bars represent  $\pm 1$  standard deviation as determined by making multiple measurements.

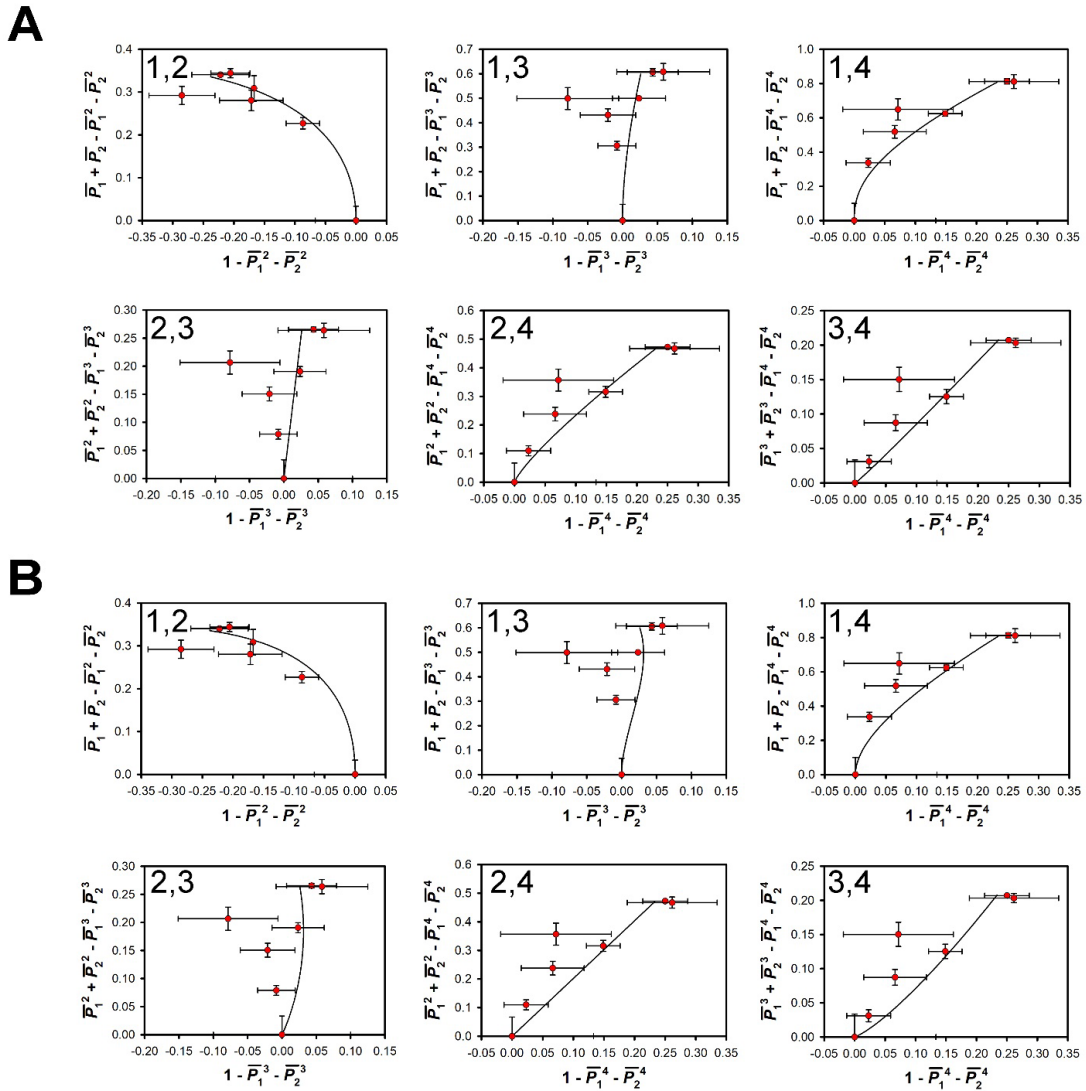


Figure 4.3 Analysis of 2-BIT data in an ITX/PETA photoresist at an excitation wavelength of 750 nm. The absorption is assumed to arise from (A) a combination of 2-photon and 3-photon absorption and (B) a combination of 2-photon and 4-photon absorption. The solid lines are the calculated values for different absorption orders given the assumed pairs of absorption orders. The poor fits indicate that neither of the pairs of two absorption orders tested describe the data. For this wavelength, no other pairs of orders of absorption are justified. The error bars represent  $\pm 1$  standard deviation as determined by making multiple measurements.

To estimate the dependence of  $n_{eff}$  on excitation wavelength, the data in Figure 4.1D were fit with a cubic spline (solid line in Figure 4.1D) to determine  $n_{eff}(\lambda)$  in the range  $\lambda = 750 - 850$  nm. Figure 4.1E shows a “linearized” polymerization action spectrum. To determine the wavelength axis, we assumed, as in Figure 4.1B, that the true order of nonlinear absorption over this wavelength range is 2, and we plot  $\bar{P}_{th}^{n_{ef}(\lambda)}$

as a function of the excitation wavelength. The agreement between the linearized action spectrum and the absorption spectrum at half of the 2PA excitation wavelength is striking. This analysis indicates that polymerization occurs solely through a 2PA process throughout this range of wavelengths. The slight deviation between the linearized action spectrum and the linear absorption spectrum is attributed to the solvatochromic shift being different for ITX in monomers (for the action spectrum) and in methanol (for the absorption spectrum). The questions we now address are (1) Why are the measured exponents higher than 2? and (2) Why does  $n_{eff}$  depend strongly on the excitation wavelength? From Figure 4.1D and Figure 4.1E, it is also clear that weaker 2PA (i.e., a higher value of  $P_{th}$ ) correlates with higher  $n_{eff}$ .

#### 4.32 Triplet-state absorption

A previous study suggested that stimulated emission is responsible for the strong inhibition dynamics that ITX/PETA photoresists exhibit under irradiation at 532 nm.<sup>47</sup> Subsequent ultrafast, pump-probe spectroscopy experiments revealed that at deactivation wavelengths longer than 500 nm, the influence of stimulated emission on deactivation is negligible.<sup>62</sup> Harke et al. studied the inhibition of ITX photoresists with a deactivation wavelength of 630 nm,<sup>29</sup> and suggested that the long-lived photogenerated species in ITX are triplet states. It was therefore proposed that the inhibition mechanism in this photoresist involves depletion of the lowest triplet state ( $T_1$ ) of ITX when the deactivation beam is resonant with transition between  $T_1$  and a higher triplet state. Although triplet absorption followed by RISC from a highly excited triplet state to a high singlet state has been suggested to be the deactivation mechanism,<sup>28,29,60</sup> no direct evidence has been provided for this process.

The triplet quantum yield of thioxanthenes can be as high as 85%,<sup>72,73</sup> underscoring the potential importance of triplet-state dynamics in these systems. To investigate these dynamics, we studied ITX solutions using a transient absorption (TA) spectrometer with a temporal resolution of 0.1 ms. TA is a powerful means of studying excited triplet states and identifying short-lived intermediates.<sup>74</sup> The time evolution of the TA spectrum of ITX in ethylene glycol following excitation at 355 nm is shown in Figure 4.4A. There are two major features in the initial spectrum, one at ~318 nm and another at ~605 nm (see dashed vertical lines in Figure 4.4A). Each of these peaks is assigned to absorption from both  $T_1$  and  $T_2$  to higher triplet states of ITX, on the basis of earlier reports.<sup>75</sup> The initial peaks decay over a timescale that is considerably longer than the longest delay time studied, 10  $\mu$ s. A new peak grows in at ~345 nm on a timescale of a few  $\mu$ s. We attribute this new feature to absorption of ketyl radicals that are created via H-atom transfer from the solvent to the carbonyl group of ITX in the  $T_2$  state. The fact that ketyl radicals can be formed on a timescale that is considerably longer than the expected lifetime of the  $T_2$  state suggests that this state is at least somewhat thermally accessible from the  $T_1$  state in ethylene glycol.

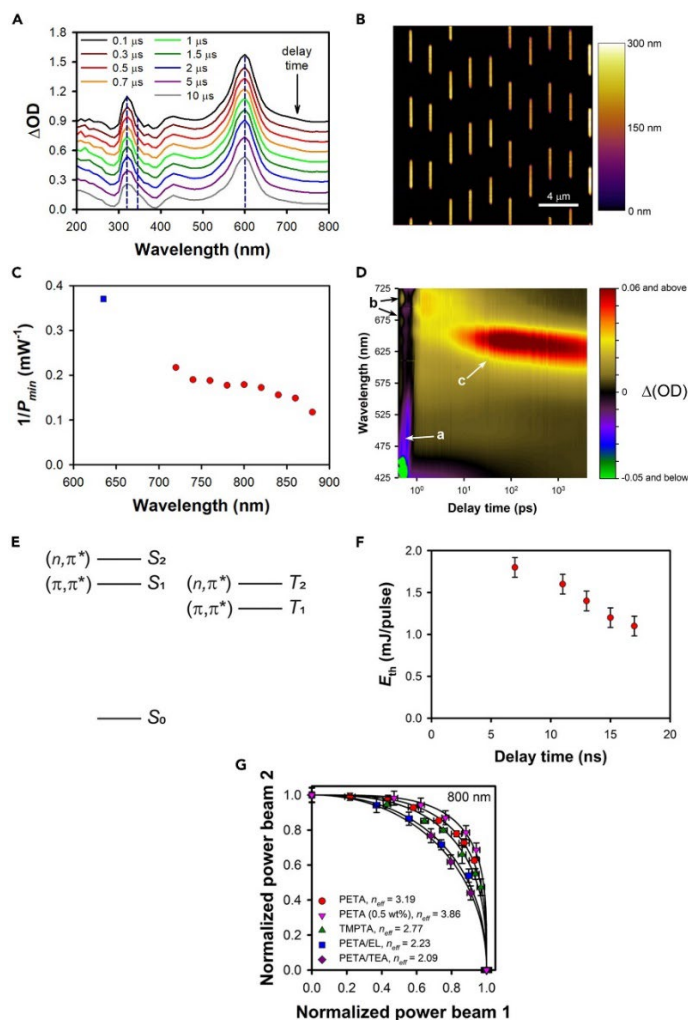


Figure 4.4 Deactivation and self-deactivation of ITX (A) Transient-absorption spectra of ITX in ethylene glycol with 355 nm, 7 ns excitation pulses. The DOD scale is correct for the spectrum with a 10 ms delay. Each subsequent spectrum, moving from longer delays to shorter delays, has been offset by 0.1 units vertically from the previous one for clarity. The vertical dashed lines indicate spectral features that are discussed in the text. (B) AFM images of lines written in an ITX/PETA photoresist with 800 nm, 150 fs laser pulses at a stage velocity of 20 nm/s. A chopped, spatially overlapped, 800 nm, CW beam was used to inhibit polymerization. The average excitation power was 5 mW and the deactivation power was 30 mW. The scale bar represents 4 nm. (C) Deactivation action spectrum of the photoresist following excitation with 800 nm, 150 fs laser pulses at an average excitation power of 8.2 mW. The blue square is for deactivation with a 635 nm diode laser, and the red circles are for deactivation with a Ti:sapphire oscillator in CW mode. (D) Ultrafast pump/probe spectrum of ITX in glyme. Excitation was performed at 400 nm, and white-light continuum was used as the probe. (E) Representative Jablonski diagram for ITX in a polar solvent. (F) Delay-time dependence of the threshold pulse energy for deactivation at 630 nm of the ITX/PETA photoresist following excitation with 315 nm pulses. Both beams had a pulse duration of 7 ns and a repetition rate of 10 Hz. The error bars represent the estimated uncertainty in determining the deactivation threshold. (G) 2-BIT data and the corresponding  $n_{eff}$  values for photoresists based on PETA (circles, 1.5 wt% ITX, and down triangles, 0.5 wt% ITX), TMPTA (up triangles, 1.5 wt% ITX), PETA and ethyl lactate (squares, 1.5 wt% ITX), and PETA and triethylamine (diamonds, 1.5 wt% ITX). The error bars in (F) and (G) represent  $\pm 1$  standard deviation, as determined by making multiple measurements.

The triplet absorption features of ITX are generally long-lived, having lifetimes of tens of ms or longer, depending on the solvent (Table 4.1). Interestingly, the triplet absorption spectrum is non-zero at 800 nm, and can extend to 900 nm or beyond. This observation raises the question of whether ITX triplet states can be deactivated within this wavelength region. To investigate this scenario, we fabricated polymer lines in ITX photoresists using ultrafast excitation at 800 nm, while simultaneously irradiating with CW light at a wavelength of 800 nm. The two beams were spatially coincident, and the CW beam was chopped. As evidenced by the atomic force microscopy (AFM) data in Figure 4.2B, 800 nm radiation can indeed cause complete inhibition of polymerization. The fact that the same color of light used for excitation also promotes deactivation suggests that deactivation can be induced by the same laser pulse train that is used for excitation, decreasing the efficiency of the exposure. We term this phenomenon “self-deactivation.”

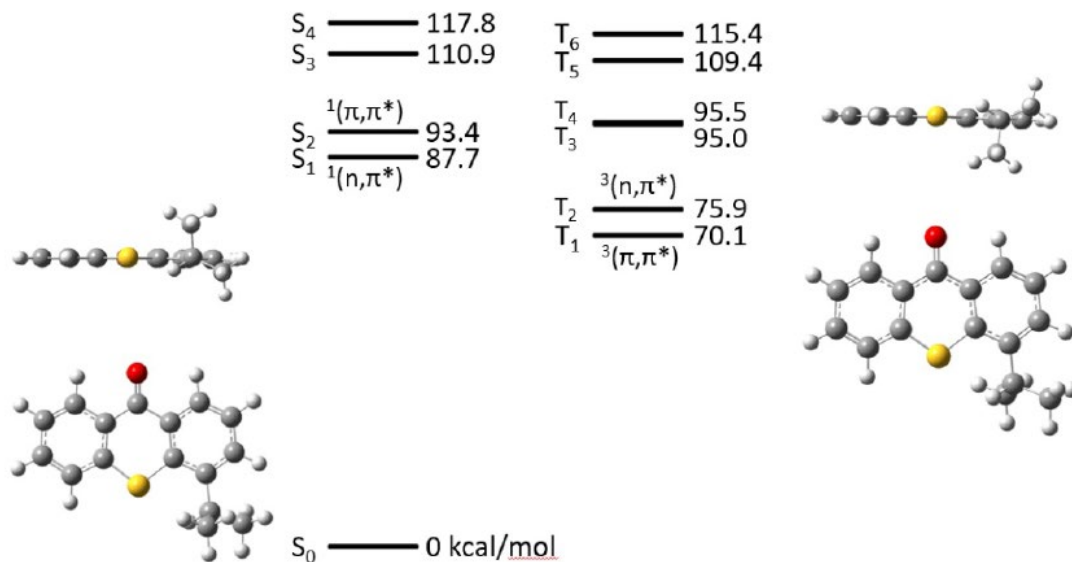
Table 4.1 ITX triplet-state lifetimes in different solvents as measured by microsecond transient absorption.

Solvent	Lifetime ( $\mu\text{s}$ )
Acetonitrile	$2.7 \pm 0.1$
Isopropyl alcohol	$5.9 \pm 0.1$
Polyethylene glycol	$37.1 \pm 0.9$
Ethylene glycol	$25.8 \pm 0.2$
Glyme	$1.6 \pm 0.1$

Our results are consistent with the previous conjecture<sup>29</sup> that deactivation involves triplet absorption. However, a more rigorous test of this hypothesis requires a comparison of the wavelength dependences of triplet absorption and deactivation. To this end, we developed a technique that we call deactivation action spectroscopy (DAS). In the case of ITX-based photoresists, DAS was implemented by keeping the excitation conditions the same (i.e., wavelength, average power, and stage velocity), while varying the deactivation wavelength and power. At each deactivation wavelength, we determined the minimum CW laser power required to cause complete inhibition of polymerization. Assuming that deactivation occurs through linear absorption, the DAS spectrum is a plot of the inverse of the threshold power for deactivation as a function of deactivation wavelength. As shown in Figure 4.4C, DAS data in an ITX-based photoresist bear a strong resemblance to the triplet absorption spectrum in the same wavelength range (Figure 4.4A). This correspondence provides additional evidence that triplet absorption is a key step in deactivation.

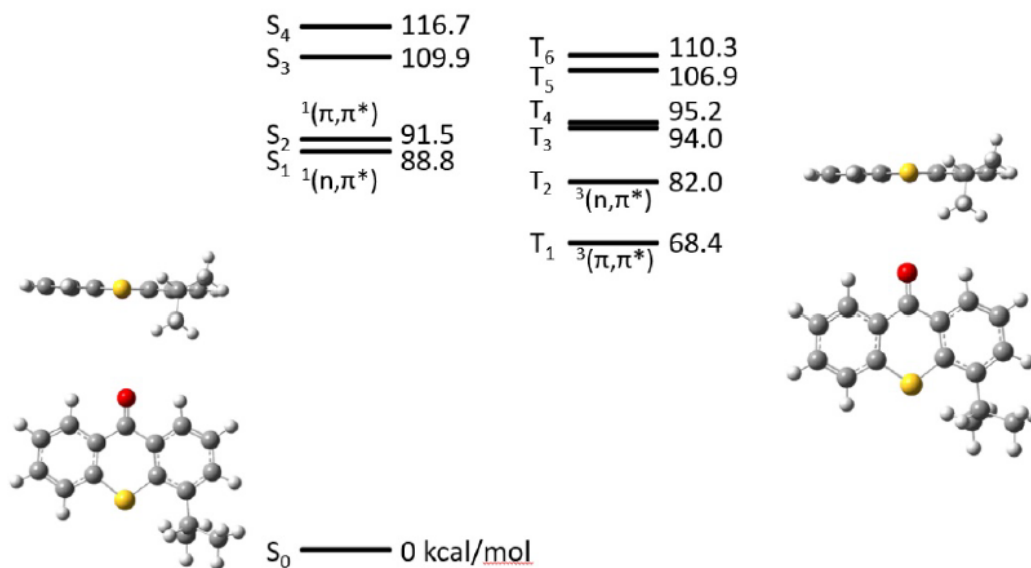
We performed ultrafast transient absorption spectroscopy on a solution of ITX in glyme to explore faster triplet dynamics. Figure 4.4D is a heatmap of the time-resolved absorbance change following ultrafast excitation at 400 nm. For  $\sim 500$  fs after excitation there is a negative feature (labeled a) from  $\sim 400$  nm to  $\sim 550$  nm that arises from stimulated emission. A longer-lasting feature at the shorter end of this

wavelength range arises from a ground-state bleach. After  $\sim 500$  fs, two positive, excited-state absorption (ESA) features (labeled b) grow in at  $\sim 660$  nm and  $\sim 700$  nm. The Jablonski diagram in Figure 4.4E shows the energy levels of ITX in a typical polar organic solvent. The  $S_1$  and  $S_2$  states of ITX have similar energies, in analogy to what is known for the parent molecule thioxanthone (TX).<sup>46</sup> One of these states has ( $n,\pi^*$ ) character, whereas the other has ( $\pi,\pi^*$ ) character. Density functional theory (DFT) calculations showed that the energetic ordering of the states depends on the nature of the solvent (Figures 4.5-4.9). In THF and ethyl acetate, the ( $n,\pi^*$ ) singlet state has the lower energy, whereas in water and ethylene glycol the ( $\pi,\pi^*$ ) singlet state has the lower energy. Because glyme is a polar, aprotic solvent, we assign the ESA feature at  $\sim 660$  nm to the ( $n,\pi^*$ ) singlet state and the feature at  $\sim 700$  nm to the ( $\pi,\pi^*$ ) singlet state, assuming that ESA leads to the same higher excited state from  $S_1$  and  $S_2$ . Although absorption from these states could potentially appear immediately following excitation, the  $\sim 500$  fs lag time observed presumably arises from a combination of vibrational relaxation and the existence of a negative-going feature in the same spectral region, which can be seen most clearly at wavelengths longer than 700 nm.



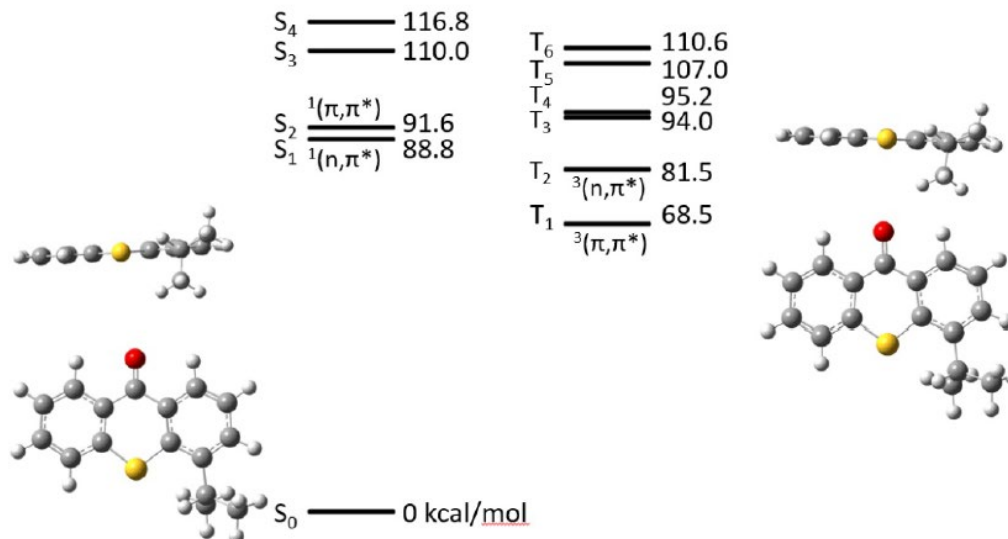
(u)M062x/6-311G(d)

Figure 4.5 Vertical transition energies for the lowest singlet and triplet states of 4-ITX in vacuum. The energy cutoff is the vertical transition energy of the  $S_4$  state. The molecular structures are those for the ground state (left) and the lowest triplet state (right). The level of the calculations is (u)M062x/6-311G(d).



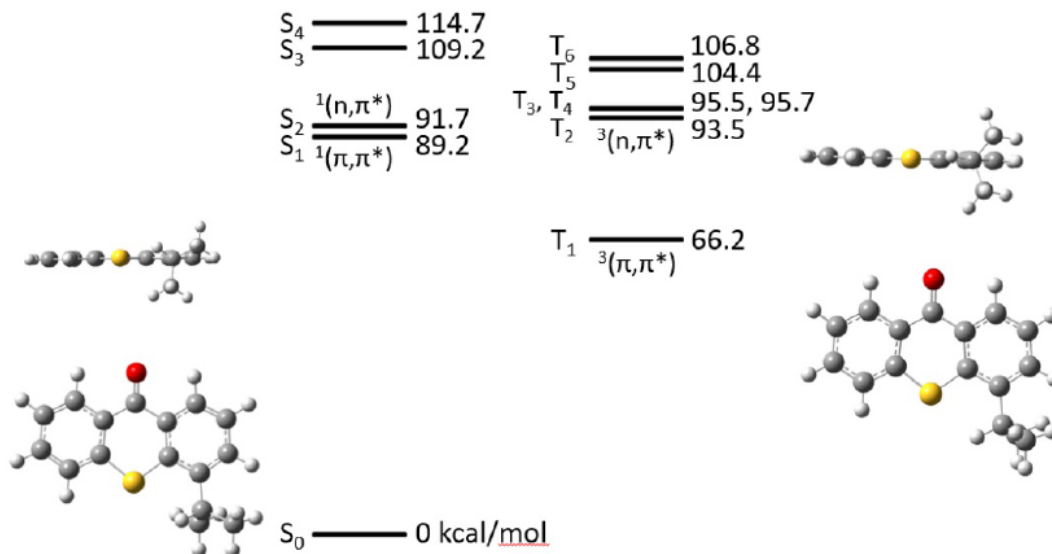
(u)M062x/6-311G(d) scrf=(smd, solvent=THF)

Figure 4.6 Vertical transition energies for the lowest singlet and triplet states of 4-ITX in tetrahydrofuran. The energy cutoff is the vertical transition energy of the  $S_4$  state. The molecular structures are those for the ground state (left) and the lowest triplet state (right). The level of the calculations is (u)M062x/6-311G(d).



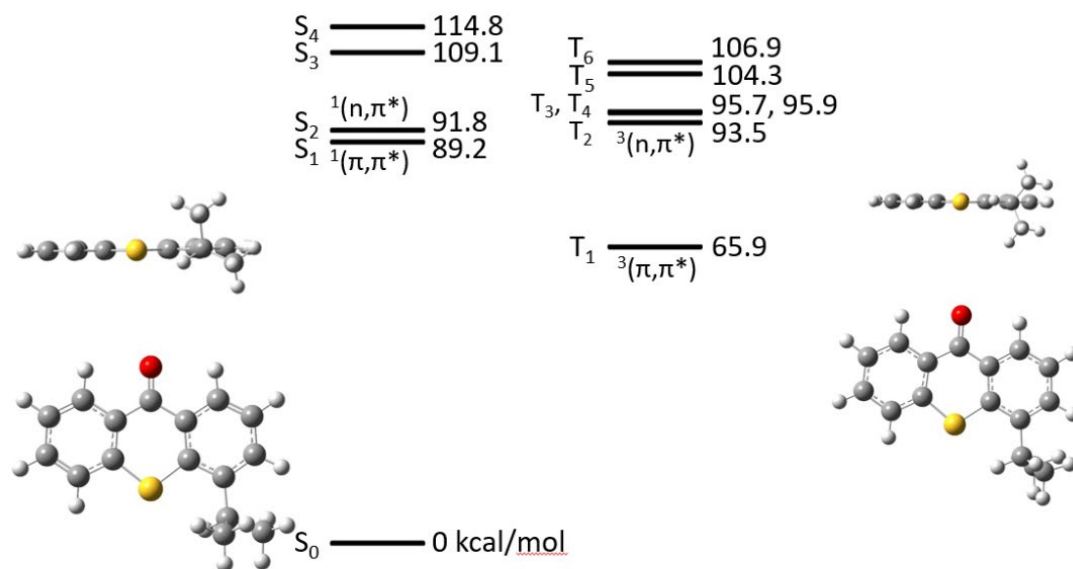
(u)M062x/6-311G(d) scrf=(smd, solvent=ethylethanoate)

Figure 4.7 Vertical transition energies for the lowest singlet and triplet states of 4-ITX in ethyl acetate. The energy cutoff is the vertical transition energy of the S4 state. The molecular structures are those for the ground state (left) and the lowest triplet state (right). The level of the calculations is (u)M062x/6-311G(d).



(u)M062x/6-311G(d) scrf=(smd, solvent=1,2-EthaneDiol)

Figure 4.8 Vertical transition energies for the lowest singlet and triplet states of 4-ITX in ethylene glycol. The energy cutoff is the vertical transition energy of the S4 state. The molecular structures are those for the ground state (left) and the lowest triplet state (right). The level of the calculations is (u)M062x/6-311G(d).



(u)M062x/6-311G(d) scrf=(smd, solvent=water)

Figure 4.9 Vertical transition energies for the lowest singlet and triplet states of 4-ITX in water. The energy cutoff is the vertical transition energy of the  $S_4$  state. The molecular structures are those for the ground state (left) and the lowest triplet state (right). The level of the calculations is (u)M062x/6-311G(d).

At delay times between 1 ps and 10 ps, there is evidence in the ESA bands for population changes in the excited singlet states (Figure 4.10). The blue shift of the ESA bands over this same time period reflects solvation dynamics.<sup>76</sup> Within 20 ps, the ESA feature has decayed, and a positive feature has grown in at  $\sim 650$  nm. This latter feature is the result of population growth in a triplet state via ISC. We therefore conclude that the time constant for the equilibration between the  $S_1$  and  $T_2$  states is on the order of 10–20 ps. The triplet absorption feature (labeled c) shifts to the blue on the nanosecond timescale. The triplet state initially populated is not the lowest triplet state, so this shift reflects a combination of equilibration between the triplet states and solvation. In the solvent in which these spectra were obtained, glyme, the  $(\pi,\pi^*)$  triplet state should have the lowest energy, with the  $(n,\pi^*)$  triplet being the state through which ISC occurs,<sup>44,77</sup> again in analogy with TX.<sup>45</sup>

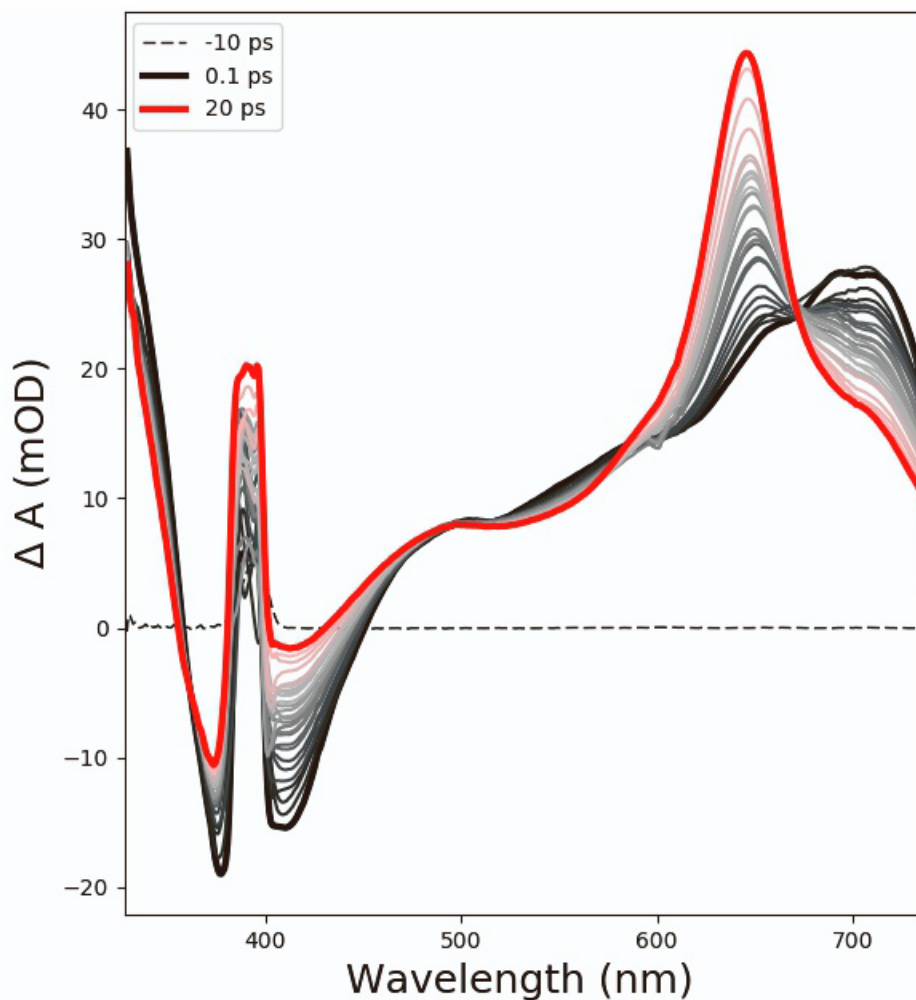


Figure 4.10 Transient absorption spectra of ITX in glyme (dimethoxyethane) at 3 different pump-probe time delays. The excitation wavelength was 400 nm, and the feature at this wavelength arises from a notch filter.

We developed an in situ technique to monitor exposure (i.e., crosslinking of a photoresist film) and deactivation to examine in more detail how triplet dynamics are manifested in a photoresist (Figure 4.11). Large area exposures were performed at a repetition rate of 10 Hz and a wavelength of 315 nm using the frequency-doubled output of an optical parametric oscillator (OPO) with a pulse length of  $\sim 7$  ns. The 630 nm fundamental of the OPO was used for deactivation. The minimum deactivation power for a fixed exposure time was determined as a function of the time delay between the 315 nm and 630 nm pulses. No deactivation was observed when the

deactivation pulse preceded the excitation pulse. Figure 4.4F shows the deactivation threshold for delay times ranging from 7 ns to 17 ns, a range over which the threshold decreases by  $\sim 40\%$ .

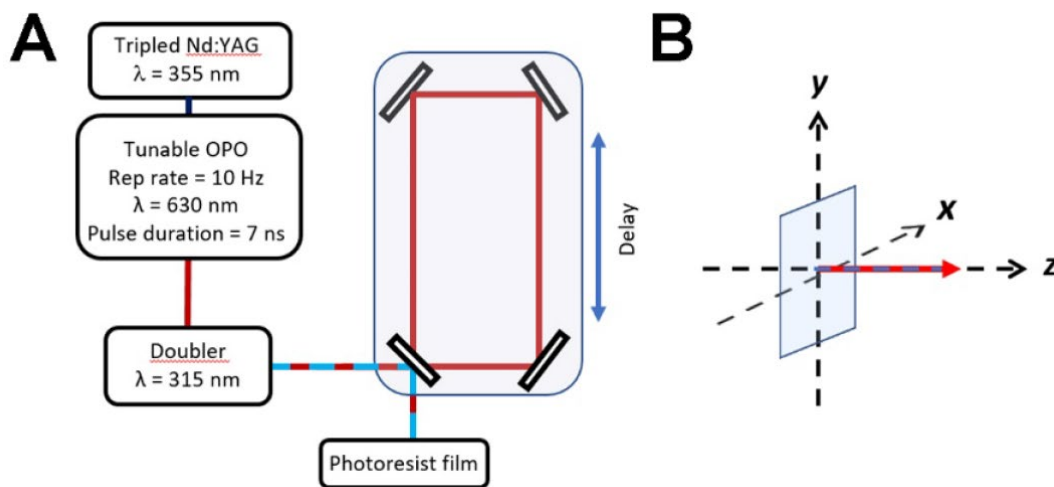


Figure 4.11 In situ monitoring of exposure and deactivation. (A) Schematic of the experimental setup. A tripled Nd:YAG pumps a tunable pulsed OPO that generates 7 ns pulses at 630 nm. These pulses are directed to a frequency doubler that outputs the doubled and undoubled light collinearly. A dichroic mirror is used to separate the collinear beams. The 630 nm light traverses an adjustable delay line. The two colors are overlapped spatially at the surface of the sample. (B) Schematic of the sample geometry. The film is positioned in the  $xy$ -plane and the pulses propagate along the  $z$ -axis.

These results yield key insights into the photophysics of deactivation based on the increase in deactivation efficiency with increasing delay time. The  $(n,\pi^*)$  triplet state is expected to be reactive, but the TA experiments discussed above show that this state generates radicals on a timescale much longer than 17 ns. The 100 ms repetition time used for the large-area exposure experiments is sufficient to allow all excited molecules to relax between pulses, as is the case in the TA experiments described above. Thus, the excitation and deactivation in this experiment must occur on a shot-by-shot basis. Based on the data in Figure 4.4D, the  $(n,\pi^*)$  triplet state undergoes internal conversion to the  $(\pi,\pi^*)$  triplet state on a timescale of nanoseconds. This timescale is highly dependent on the solvent environment.<sup>43,77</sup> It

appears that relaxation to the  $(\pi,\pi^*)$  triplet state enhances the efficiency of deactivation. Because internal conversion and deactivation are both first-order in the concentration of the  $(n,\pi^*)$  states, the order in which these processes occur does not affect the ultimate  $(n,\pi^*)$  population. Thus, the  $(\pi,\pi^*)$  triplet state serves as a long-term, inert reservoir, but the  $(n,\pi^*)$  triplet state remains thermally accessible to population in the  $(\pi,\pi^*)$  state. Furthermore, deactivation occurs more efficiently from the  $(\pi,\pi^*)$  state than from the  $(n,\pi^*)$  state. This phenomenon is likely due to a larger transition dipole for  $(\pi,\pi^*)$  absorption to a higher triplet state. Together, these effects account for the data in Figure 4.4F.

We note that the details of exposure are different for excitation with a Ti:sapphire oscillator, as the oscillator repetition time is on the order of 13 ns, rather than 100 ms. With the short repetition time of the Ti:sapphire laser, the  $(n,\pi^*)$  triplet state is continuously replenished, so that initiation can occur even in a resist in which  $T_2$  is not thermally accessible from  $T_1$ . We expect that the chemical nature of the monomers will have an influence on the exposure/deactivation behavior of an ITX-based photoresist. With this idea in mind, we performed 2-BIT experiments on additional ITX photoresists. We prepared a photoresist with trimethylolpropane triacrylate (TMPTA) as the monomer, and in another we added 20 wt% of ethyl lactate to the ITX/PETA mixture. As can be seen in Figure 4.4G,  $n_{eff}$  drops from  $3.19 \pm 0.05$  to  $2.77 \pm 0.05$  in moving from the ITX/PETA photoresist to the ITX/TMPTA photoresist. The decrease in  $n_{eff}$  results from chemical and/or physical differences that cause ITX/TMPTA to have a lower deactivation efficiency than ITX/PETA, resulting in less self-deactivation by the excitation beam.

The addition of the ethyl lactate to the ITX/PETA photoresist results in an even more dramatic reduction of  $n_{eff}$ , to  $2.23 \pm 0.05$ . We performed TA experiments on ITX solutions containing different percentages of ethyl lactate to delve into the cause of this behavior. These studies revealed that the triplet-state lifetime of ITX decreases with increasing ethyl lactate concentration, and that the signal from the ketyl radical appears rapidly in this solvent (Figure 4.12). These results indicate that ethyl lactate acts as a coinitiator, transferring a hydrogen atom to a molecule in the  $(n,\pi^*)$  triplet state much more rapidly than the monomers can.

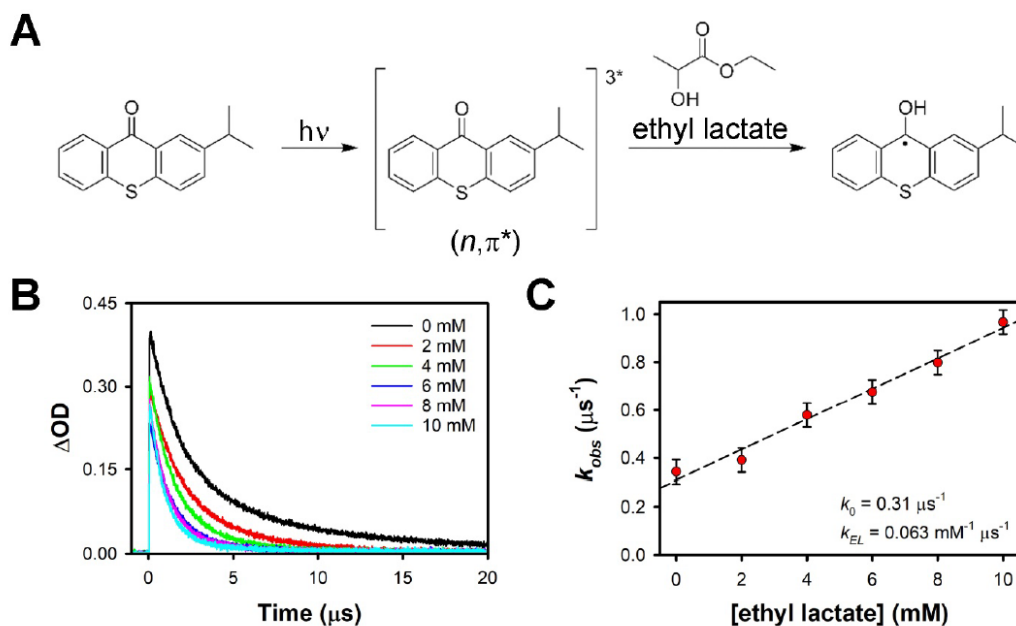


Figure 4.12 Microsecond transient absorption experiments on ITX/PETA photoresists containing ethyl lactate. (A) Mechanism for the generation of ketyl radicals from the  $n,\pi^*$  triplet state, shown for 2-ITX. (B) Absorption transients for different concentrations of ethyl lactate. Excitation was at 355 nm, and the transients were collected at 620 nm. (C) The observed rate constants  $k_{obs}$  are consistent with pseudo-first-order kinetics, with  $k_{obs} = k_0 + k_{EL} [EL]$  [EL = ethyl lactate]. The error bars represent  $\pm 1$  standard deviation as determined by making multiple measurements.

We next made 2-BIT measurements in an ITX/PETA photoresist containing a common coinitiator, triethylamine, to confirm the influence of such species on  $n_{eff}$ . In this case  $n_{eff}$  dropped even further, to  $2.09 \pm 0.05$  (Figure 4.4G). The considerably

more rapid reaction of the triplet-state molecules in the presence of a coinitiator renders self-deactivation less effective, because radical initiation can commence before relaxation to the lowest triplet state. The more efficient the coinitiator, the more rapid the initiation process, and the less effective the self-deactivation process.

An additional implication of the self-deactivation scenario is that the value of  $n_{eff}$  will depend on the concentration of the photoinitiator. The lower the concentration of the photoinitiator, the higher the threshold intensity for polymerization. A higher threshold intensity leads to an increased amount of self-deactivation, which is predicted to cause  $n_{eff}$  to increase. Indeed, we find that with 800 nm excitation, the  $n_{eff}$  value of  $3.19 \pm 0.05$  measured in a PETA photoresist with 1.5 wt% of ITX increases to  $3.86 \pm 0.05$  when the photoinitiator concentration is decreased to 0.5 wt% (Figure 4.4G).

#### 4.33 Phosphorescence

Phosphorescence provides another means of investigating triplet photophysics. The luminescence intensity, including both fluorescence from  $S_1$  and phosphorescence from  $T_1$ , has the advantage of being linear in the concentration of excited molecules, which is not the case for photopolymerization.<sup>69,70</sup> We developed a luminescence deactivation technique to probe the photophysics of deactivation. An ultrafast laser was used to excite an ITX solution through a high-numerical-aperture objective, and luminescence was collected epifluorescently. We chose PEG-400 as the solvent, because this material approximates the photoresist in polarity and viscosity. A second CW laser beam that could be tuned through in a wavelength range known to deactivate photoresists containing ITX (740 nm–840 nm) was

focused through the same objective. The focal volumes of the two beams were overlapped in three dimensions.

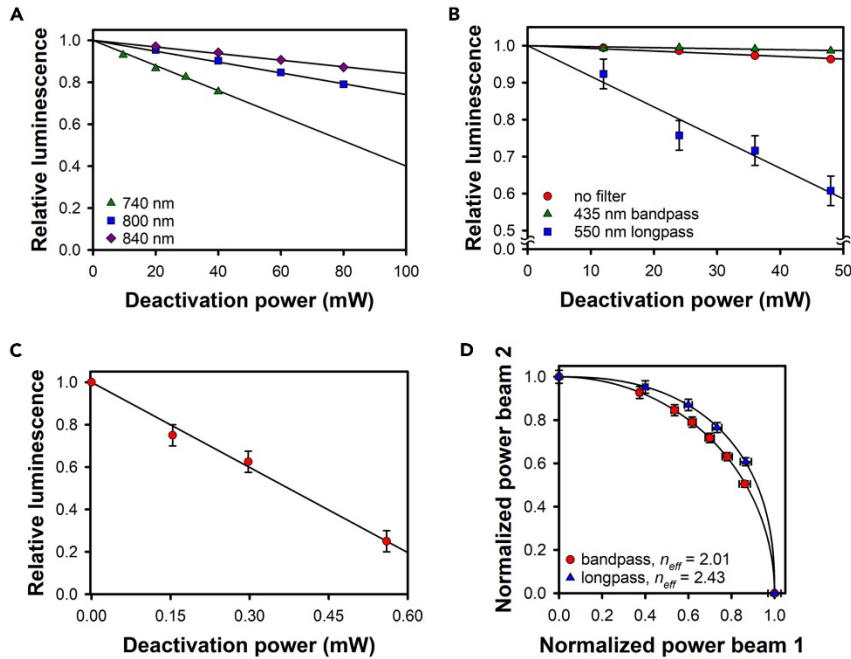


Figure 4.13 Luminescence studies of ITX in PEG-400 (A) Luminescence as a function of CW deactivation power. Excitation was performed using 800 nm, 150 fs pulses, and deactivation was performed at 740 (triangles), 800 nm (squares), and 840 nm (diamonds). (B) Inhibition of luminescence by 800 nm light with detection in different spectral windows: unfiltered (circles), with a 445 nm bandpass filter to capture predominantly fluorescence (triangles), and with a 550 nm longpass filter to capture only phosphorescence (squares). (C) Inhibition of luminescence by 635 nm light using a longpass filter with a 645 nm cutoff. Phosphorescence deactivation is extremely efficient at this wavelength. (D) 2-BCEIn data for fluorescence (circles) and phosphorescence (triangles) with ultrafast, 800 nm excitation. The difference in  $n_{eff}$  between the two datasets indicates that self-deactivation plays a role in the phosphorescence data. The error bars in all panels represent  $\pm 1$  standard deviation, as determined by making multiple measurements.

As shown in Figure 4.13A, the CW beam had an inhibitory effect on the luminescence that exhibits the same qualitative wavelength dependence observed in the deactivation action spectrum in Figure 4.4C, in which shorter wavelengths provide more efficient deactivation. The decrease in the luminescence is linear in the deactivation power. To examine this phenomenon further, we used 800 nm deactivation and probed the luminescence in different spectral windows (Figure 4.13B). With unfiltered emission, for powers up to 50 mW, the deactivation is limited

to a few percent. A 435 nm bandpass filter with a full width at half maximum bandwidth of 48 nm restricts transmission to the wavelength region of the ITX fluorescence spectrum (Figure 4.14), although some phosphorescence should fall within this window as well.<sup>60</sup> When this filter is used, virtually no deactivation is observed (Figure 4.13B). A 550 nm longpass filter blocks the fluorescence of ITX, but transmits some of the phosphorescence.<sup>60</sup> When this filter is used, substantial deactivation is observed (Figure 4.13B), which suggests that the small amount of deactivation observed with the 435 nm bandpass filter is also due to inhibition of phosphorescence. In all cases, the deactivation was linear in the power of the 800 nm CW laser.

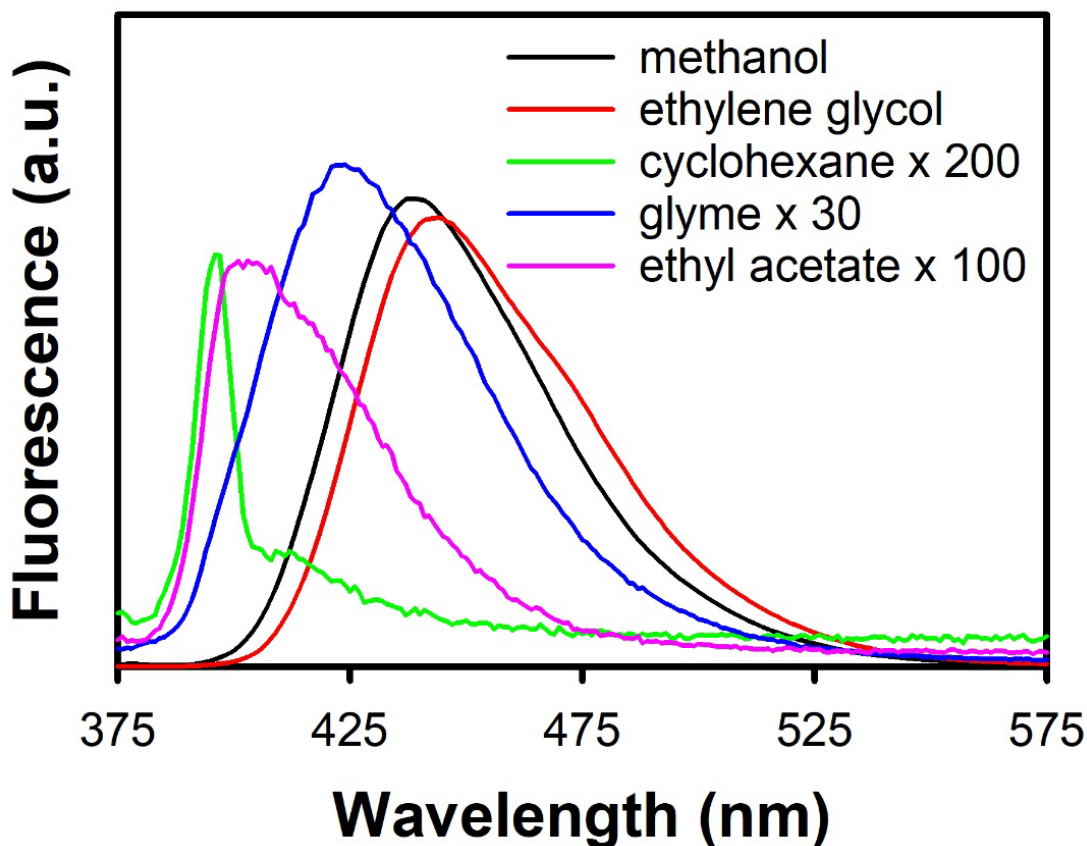


Figure 4.14 Fluorescence spectra of ITX in different solvents.

The polymerization deactivation action spectrum (Figure 4.4C) indicates that deactivation is considerably more efficient at 635 nm than at 800 nm. We therefore tested the ability of CW, 635 nm light to deactivate phosphorescence, in this case using a 645 nm longpass filter so that scatter from the deactivation beam would not be detected. Using an efficient deactivation wavelength and filtering out all fluorescence facilitates the sensitive detection of phosphorescence deactivation. As shown in Figure 4.13C, this scheme enables extremely efficient phosphorescence deactivation of ITX, with a reduction of emission of greater than 80% at a laser power of less than 0.6 mW.

The luminescence observed using longpass filters serves as a proxy for the population of  $T_1$ , which is the  $(\pi,\pi^*)$  triplet state in this solvent. Given that virtually no deactivation is observed when detection is restricted to the spectral window of the fluorescence spectrum, our results exclude stimulated emission as the mechanism of deactivation at the CW wavelengths studied here. The  $T_2 (n,\pi^*)$  state is expected to have a shorter intrinsic phosphorescence lifetime than the  $T_1 (\pi,\pi^*)$  state.<sup>77</sup> However, because the  $(n,\pi^*)$  triplet has an energy similar to that of the first excited singlet state, phosphorescence from  $T_2$  will occur in essentially the same wavelength range as fluorescence. In contrast,  $T_1$  is the most stable triplet state, and so will phosphoresce at longer wavelengths than does  $T_2$ . With the 645 nm longpass filter, the only phosphorescence detected should therefore arise from  $T_1$ .

We next measured  $n_{eff}$  independently for fluorescence and phosphorescence. For these measurements, we employed another technique that we have developed recently, 2-beam constant emission intensity (2-BCEIn) spectroscopy.<sup>68</sup> 2-BCEIn is

analogous to 2-BIT, except that  $n_{eff}$  is measured for the emission intensity (Figure 4.15). In contrast to traditional methods for studying emission induced by nonlinear absorption, 2-BCEIn can determine  $n_{eff}$  at any given emission intensity, using only a limited range of average excitation powers.

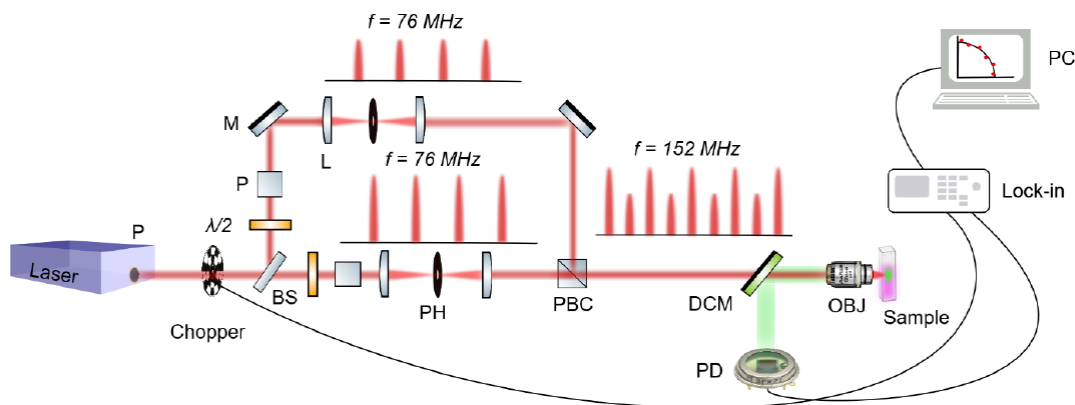


Figure 4.15 Schematic of the experimental setup for 2-beam constant emission intensity (2-BCEIn) spectroscopy. Two pulse trains with independently adjustable average powers are interleaved in time and focused into a sample to generate fluorescence observable via linear and/or nonlinear excitation. BS = beam splitter,  $\lambda/2$  = half-wave plate, P = polarizer, M = mirror, f = repetition rate, PBC = polarizing beam cube, DCM = dichroic mirror, OBJ = objective lens, PD = photodiode, PC = personal computer.

We note that  $n_{eff}$  in a given system is dependent on the observable. For 2-photon excitation of ITX, we expect that  $n_{eff} = 2$  for fluorescence but that  $n_{eff} > 2$  for phosphorescence, because self-deactivation will play a role in phosphorescence that is similar to its role in photopolymerization. 2-BCEIn measurements in ITX solutions using 800 nm ultrafast excitation bear out this prediction, as shown by the data in Figure 4.13D. When a 435 nm bandpass filter is used to probe fluorescence, the measured value of  $n_{eff}$  is  $2.01 \pm 0.05$ . This value of  $n_{eff}$  agrees with the results of previous studies using the Z-scan technique, in which ultrafast excitation was reported to take place via 2PA.<sup>60</sup> However, when the phosphorescence is probed by using a longpass filter, we find that  $n_{eff} = 2.42 \pm 0.05$ . The measured exponents were

independent of whether the beams were spatially overlapped, indicating that the 2-BCEIn data were not affected by repetition-rate-dependent effects.

These results place strong constraints on the deactivation mechanism of ITX. It has been suggested previously that deactivation involves excitation to a higher triplet state that then undergoes RISC to an excited singlet state,<sup>29</sup> which would presumably be higher in energy than  $S_2$ . The typical fate of such a state is to relax quickly to  $S_1$ .<sup>78</sup> In this case, we expect that luminescence deactivation experiments would show a decrease in phosphorescence, accompanied by an increase in fluorescence, due to repopulation of  $S_1$ . Given the high triplet quantum yield for  $S_1$  in ITX, this mechanism would also repopulate  $T_1$  and  $T_2$ , and so deactivation would not be efficient. A second, less common fate of high singlet states is to undergo ISC to the triplet manifold. This process would also repopulate  $T_1$  and  $T_2$  through rapid internal conversion, and so is not an efficient path for deactivation.

Radiationless relaxation in the singlet manifold is another possible deactivation mechanism.<sup>79</sup> This process could occur in two different manners. The first is that higher excited singlet states undergo internal conversion directly to the ground electronic state. This scenario is unlikely, but not impossible.<sup>77</sup> The more plausible explanation is that a higher triplet state undergoes RISC directly to a highly vibrationally excited level of the ground electronic state, a process that is known to occur in other aromatic molecules.<sup>80-82</sup> The high density of states of  $S_0$  at the energy of a higher triplet state is favorable for RISC from the perspective of Fermi's golden rule. This mechanism could lead to a small increase in fluorescence in the luminescence deactivation experiments, due to repopulation of the ground state, but

this increase would be counterbalanced by the inhibition of phosphorescence in the same wavelength region. Furthermore, in photoresists, a mechanism that regenerates the ground electronic state is the only plausible scenario in which efficient deactivation could occur.

#### 4.34 Kinetic modeling

To assess the viability of the proposed self-deactivation mechanism further, we next present a simple kinetic model. Our model contains two electronic states, the ground singlet  $S_0$  and the lowest triplet  $T_1$ , as shown in Figure 4.16A. ISC to  $T_1$  is assumed to take place instantaneously upon 2PA, the latter of which occurs with rate constant  $k_2 I^2$ , where  $I$  is the irradiance. Because ISC is assumed to be instantaneous, the state  $S_1$  is not included explicitly in the model, although the branching ratio for ISC is included implicitly in  $k_2$ . RISC to  $S_0$  is assumed to take place instantaneously following linear absorption from  $T_1$ , the latter of which occurs with rate constant  $k_1 I$ . The higher triplet state through which RISC occurs is not included explicitly in the model, and the branching ratio for RISC is included implicitly in  $k_1$ . Intramolecular vibrational relaxation (IVR) is assumed to be instantaneous in the ground electronic state.

The goal of the kinetic model is to determine how  $n_{eff}$  depends on  $k_1$  and  $k_2$ . We model a train of square pulses at repetition rate  $f$ , such that the duty cycle  $D$  is the pulse duration multiplied by  $f$ . The key result is that the fraction of population in the triplet state following an exposure of duration  $t'$  is given by

$$\frac{[T_1]_{t'}}{[T_0]_0} = \frac{\frac{k_2 I^2}{D}}{k_1 I + \frac{k_2 I^2}{D}} \left( 1 - \exp \left[ - \left( k_1 + \frac{k_2 I^2}{D} \right) t' \right] \right). \quad (4.2)$$

Here, we assume that the polymerization threshold is reached when 1% of the population is in the triplet state (i.e.  $[T_1]_{t'}/[S_0]_0 > 0.01$ ). The qualitative conclusions from this treatment do not depend on the value of the threshold.

The measurement of  $n_{eff}$  using 2-BIT relies on the concept of limited reciprocity, which means that if the exposure time is kept constant, then the same degree of crosslinking will occur regardless of the details of how the exposure is distributed within the exposure window.<sup>69</sup> 2-BIT experiments are performed at a single repetition rate, but the same exponent can be obtained by determining the threshold irradiance for polymerization as a function of the repetition rate.<sup>69,83</sup> When the repetition rate is varied in a system exhibiting limited reciprocity, the peak pulse irradiance  $I_{p,th}$  obeys the relation

$$I_{p,th} \propto f^{1/n_{eff}}. \quad (4.3)$$

Thus,

$$n_{eff} = - \frac{d \ln(f)}{d \ln(I_{p,th})}. \quad (4.4)$$

Here, we start by choosing a base repetition rate  $f$  and then determining  $I_{p,th}$  at  $f$ ,  $0.99f$ , and  $1.01f$ . We determine  $n_{eff}$  by averaging the values calculated from Equation 4.4

with  $0.99f$  and  $1.01f$ . We used  $f = 80$  MHz and a pulse length of 200 fs. The radius of the laser spot size was chosen to be  $0.5 \mu\text{m}$  and the exposure time  $0.025$  s (corresponding to a scanning speed of  $\sim 40$  nm/s). The value of  $k_2$  was held constant at  $2.21 \times 10^{-25} \text{ s}^5/\text{kg}^2$ , and  $k_1$  was varied.

Figure 4.16B shows a plot  $n_{\text{eff}}$  as a function of the value of  $k_1$ . As expected,  $n_{\text{eff}} = 2$  when  $k_1 = 0$ . As  $k_1/k_2$  increases over an order of magnitude from  $10^{-16}$  to  $10^{-15} \text{ kg/s}^3$ ,  $n_{\text{eff}}$  increases by a factor of nearly 1000. This result illustrates that self-deactivation has a strong effect on the measured exponent, and that  $n_{\text{eff}}$  alone is not a reliable indicator of the actual number of photons involved in the absorption process in molecules that are subject to this phenomenon.

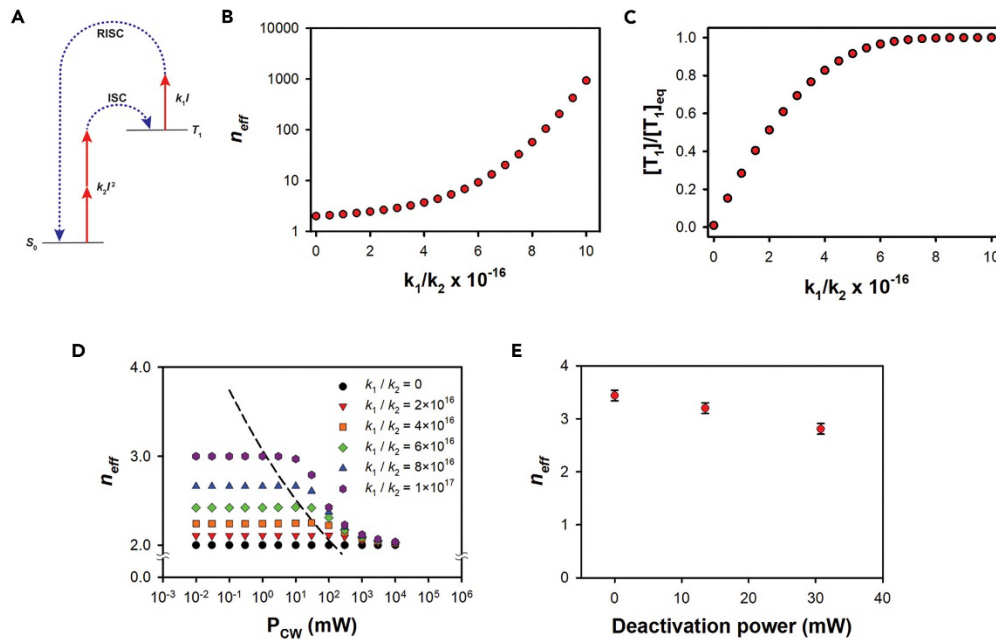


Figure 4.16 Kinetic model for self-deactivation (A) Schematic of a kinetic model that incorporates 2-photon excitation with rate constant  $k_2I^2$  and linear deactivation with rate constant  $k_1I$ , where  $I$  is the irradiance. (B) Dependence of  $n_{\text{eff}}$  on  $k_1/k_2$  (in units of  $\text{kg/s}^3$ ) for parameters given in the text. (C) Ratio of the triplet population to the equilibrium triplet population as a function of  $k_1/k_2$  for the same parameters as in (B). (D) Dependence of  $n_{\text{eff}}$  on the power of a CW deactivation beam for different values of  $k_1/k_2$  for the same parameters as in (B). The dashed line indicates the positions of the maxima in the curves. (E) Value of  $n_{\text{eff}}$  as a function of deactivation power in 2-BITD experiments on the ITX/PETA photoresist. The error bars represent  $\pm 1$  standard deviation, as determined by making multiple measurements.

The equilibrium (maximum) fractional population of the triplet state in Equation 4.2 is found by setting  $t' = \infty$  :

$$\frac{[T_1]_{eq}}{[S_0]_0} = \frac{\frac{k_2 I^2}{D}}{k_1 I + \frac{k_2 I^2}{D}} \quad (4.5)$$

At any time  $t'$ , the fraction of the population in  $T_1$  relative to its maximum value is

$$\frac{[T_1]_{t'}}{[T_1]_{eq}} = \left( 1 - \exp \left[ - \left( \frac{k_2 I^2}{D} + k_1 I \right) t' \right] \right) \quad (4.6)$$

As shown in Figure 4.16C, Equation 4.6 indicates that as  $k_1$  grows larger,  $[T_1]_{t'}$  approaches  $[T_1]_{eq}$  asymptotically. Once the concentration of  $T_1$  is near its maximum value,  $I_{p,th}$  is insensitive to changes in  $k_1$ , based on Equation 4.3. Accordingly,  $I_{p,th}$  changes less with repetition rate, leading to an increased value of  $n_{eff}$ . When  $[T_1]_{t'} = [T_1]_{eq}$ ,  $n_{eff}$  becomes infinite.

The qualitative behavior observed in this kinetic model is consistent with our experimental observations, pointing to self-deactivation as the cause of the large measured values of  $n_{eff}$ . As shown in Figure 4.1D and 4.1E, with increasing fabrication wavelength in the range explored here,  $k_1$  decreases gradually and  $k_2$  decreases rapidly. Therefore,  $k_1/k_2$  increases with wavelength, causing a corresponding increase in  $n_{eff}$ .

We used the kinetic model to make an experimentally testable prediction regarding what happens if  $n_{eff}$  is measured in the presence of a CW deactivation beam. In this case, the equation for the fraction of population in  $T_1$  becomes

$$\frac{[T_1]_{t'}}{[S_0]_0} = \frac{\frac{k_2 I^2}{D}}{k_1(I + I_d) + \frac{k_2 I^2}{D}} \left( 1 - \exp \left[ - \left( k_1(I + I_d) + \frac{k_2 I^2}{D} \right) t' \right] \right), \quad (4.1)$$

where  $I_d$  is the irradiance of the deactivation beam. The behavior of  $n_{eff}$  as a function of the deactivation power is shown in Figure 4.16D for different values of  $k_1/k_2$ ; in this case, the value of  $k_2$  was reduced to  $2.21 \times 10^{-26} \text{ s}^5 / \text{kg}^2$ , an order of magnitude lower than the value used above. The value of  $n_{eff}$  is nearly constant at low deactivation powers, but does reach a maximum at the CW deactivation power values denoted by the dashed line in Figure 4.16D. In this range of deactivation powers, the increase in the threshold irradiance causes the excitation beam to promote even greater self-deactivation. At higher deactivation powers,  $n_{eff}$  drops, eventually reaching a value of 2. When the deactivation power is higher than the excitation power, the deactivation beam is the major source of deactivation. The smaller the fraction of the deactivation that comes from the excitation beam, the closer  $n_{eff}$  gets to 2.

We developed a class of techniques called 2-beam action with deactivation (2-BAD) spectroscopies to test the prediction of our model shown in Figure 4.17. In this case, we performed 2-BIT in the presence of a CW deactivation beam, in a method we call 2-beam initiation threshold with deactivation spectroscopy (2-BITD). In Figure 4.16E, we show that, in agreement with the predictions of our model,  $n_{eff}$  decreases with increasing deactivation power. In these experiments, the ITX/PETA photoresist was exposed with pulsed 800 nm light and deactivated with CW 800 nm light.

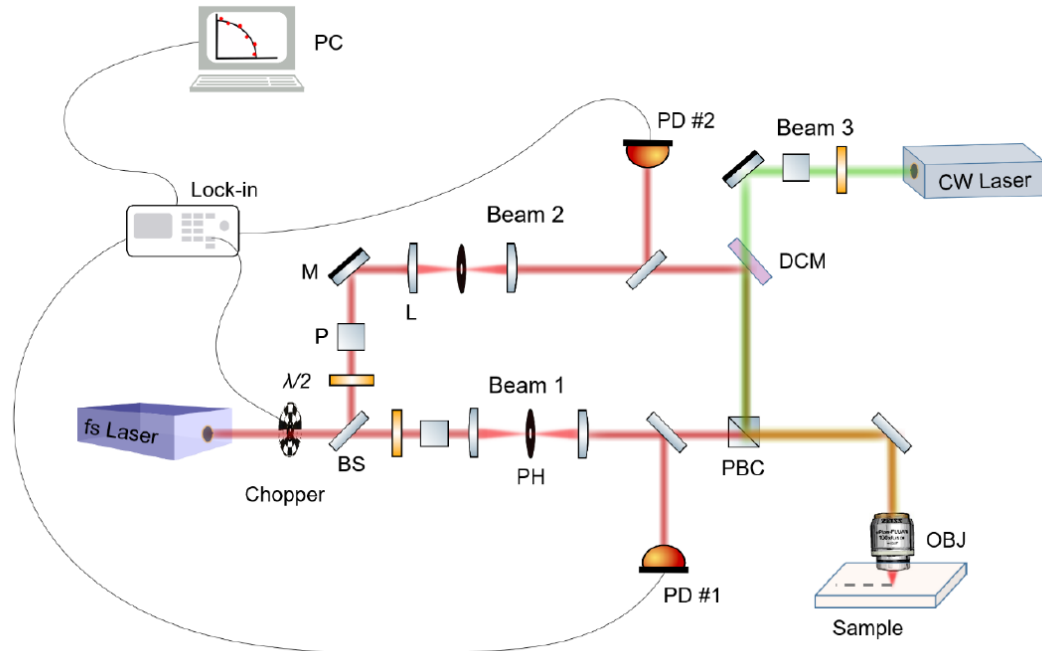


Figure 4.17 Schematic representation of the experimental setup for 2-beam initiation threshold with deactivation (2-BITD) spectroscopy. Two identical pulse trains are combined and create a pulse train with effective repetition rate that is twice the fundamental. A third CW laser beam is combined with the two pulse trains and is focused through a 100× objective. BS = beam splitter,  $\lambda/2$  = half-wave plate, P = polarizer, M = mirror, PBC = polarizing beam cube, DCM = dichroic mirror, OBJ = objective lens, PD = photodiode, PC = personal computer. Related to Figure 4.16.

### 4.35 Implications for resolution

In principle, a higher order of absorption is desirable in MAP, providing improved resolution due to the greater degree of spatial confinement of the optical exposure. However, this notion is based upon  $n_{eff}$  being a measure of the actual number of photons involved in exciting the photoinitiator from  $S_0$  to  $S_1$ . The results presented above demonstrate that for ITX,  $n_{eff}$  does not reflect the total number of photons that are involved in this transition, but rather can be thought of as the effective number of photons needed on average to yield a photoinitiation event. In light of this interpretation of the meaning of  $n_{eff}$ , it is important to examine whether a higher  $n_{eff}$  translates into better resolution in ITX-based photoresists.

We used the kinetic model developed above to determine the spatial distribution of triplets in the focal plane for values of  $n_{eff}$  ranging from 2.0 to 4.5 (roughly the range seen in the 2-BIT data presented here). We assume a Gaussian distribution of irradiance transverse to the direction of laser propagation, use  $k_2 = 2.21 \times 10^{-26} \text{ s}^5 / \text{kg}^2$ , and for each  $n_{eff}$  find the value of  $k_1$  such that the peak value of  $[T_1]_{t'} / [S_0]_0$  is 0.01. The results of this modeling are shown in Figure 4.18A. We find that as  $n_{eff}$  increases, the spatial distribution of triplet states becomes broader rather than narrowing. This behavior arises from the fact that the self-deactivation is strongest where the irradiance is the highest, i.e., in the center of the beam, thus flattening out the top of the peak of the triplet distribution. Thus, when  $n_{eff}$  is larger than the number of photons involved in the transition from  $S_0$  to  $S_1$ , we predict that the effect of increasing  $n_{eff}$  is to degrade, rather than enhance, the spatial resolution.

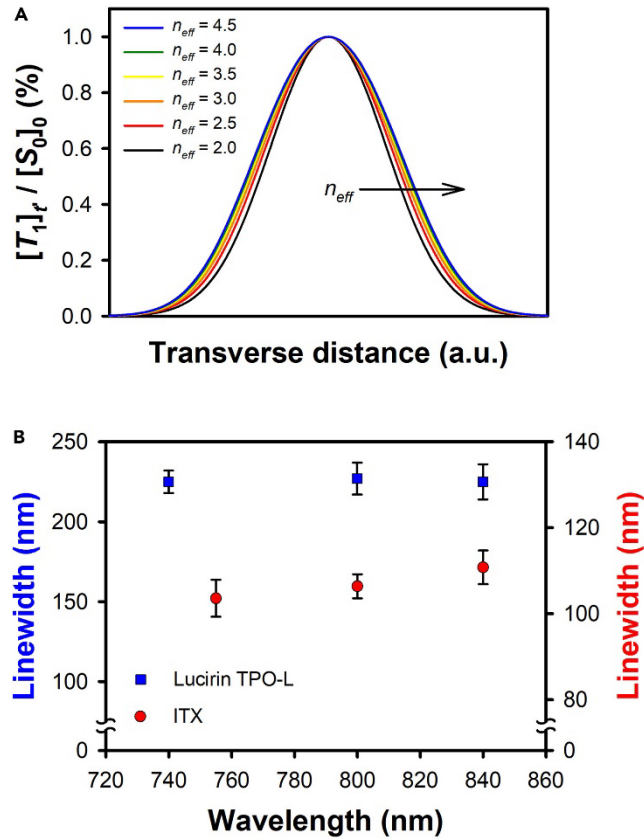


Figure 4.18 Relationship between feature size and  $n_{eff}$  in an ITX/PETA photoresist (A) Spatial dependence of the fractional triplet population in the kinetic model for different values of  $n_{eff}$  at the peak intensity. The spatial intensity distribution was assumed to be Gaussian, and  $k_2$  was fixed at  $2.21 \times 10^{-26} s^5/kg^2$ . (B) Minimum experimental linewidth as a function of excitation wavelength for the ITX/PETA photoresist (red, right axis) and a control photoresist with Lucirin TPO-L as the photoinitiator (blue, left axis). These data demonstrate that a higher  $n_{eff}$  in the ITX photoresist correlates with a broader linewidth. The error bars represent  $\pm 1$  standard deviation, as determined by making multiple measurements.

We tested these predictions experimentally by creating sets of polymerized lines using different excitation wavelengths. For each wavelength, lines were fabricated at a range of different irradiances. Scanning electron microscopy was used to determine the width of the narrowest lines that survived development. The measured average linewidths are plotted as a function of excitation wavelength in Figure 4.18B. If absorption from  $S_0$  to  $S_1$  is a 2-photon process and there is no deactivation, then  $n_{eff} = 2$ . In this case, the longest wavelength would yield the broadest lines, with the linewidth being proportional to the excitation wavelength. As

shown in Figure 4.18B, experiments with such a photoinitiator, Lucirin TPO-L,<sup>16</sup> gave minimum linewidths that were effectively independent of excitation wavelength over the range from 740 nm to 840 nm. In ITX, if  $n_{eff}$  represented the average number of photons absorbed to undergo a transition from  $S_0$  to a higher singlet state, then based on the data in Figure 4.4D, the smallest feature size should be observed at the longest wavelength. However, as shown in Figure 4.18B, the linewidth in the ITX photoresist increases with increasing wavelength. This result agrees with the predictions of our model, and is indicative of the presence of self-deactivation.

#### 4.4 Discussion

The key photophysical steps in photopolymerization using ITX without a coinitiator are summarized in Figure 4.19. 2-photon excitation drives a transition between  $S_0$  and  $S_1$  and/or  $S_2$  (the latter of which is not shown). Following excitation, the molecule can either fluoresce or undergo ISC to  $T_2$  or a vibrationally excited level of  $T_1$  (the latter case is not shown), in either case followed by IVR on a timescale of picoseconds. Molecules in the  $T_2$  state can react with easily abstractable hydrogen atoms in the monomers. However, internal conversion from  $T_2$  to  $T_1$ , the latter of which is unreactive, occurs on a timescale of nanoseconds. The  $T_1$  state can phosphoresce or, depending on the energy gap between  $T_1$  and  $T_2$ , which depends on the solvent, may be able to repopulate  $T_2$  thermally (not shown). Irradiation at a wavelength that can cause deactivation takes population in either  $T_1$  or  $T_2$  to a higher triplet state that undergoes RISC rapidly to a highly vibrationally excited level of  $S_0$ , which relaxes on a picosecond timescale via IVR.

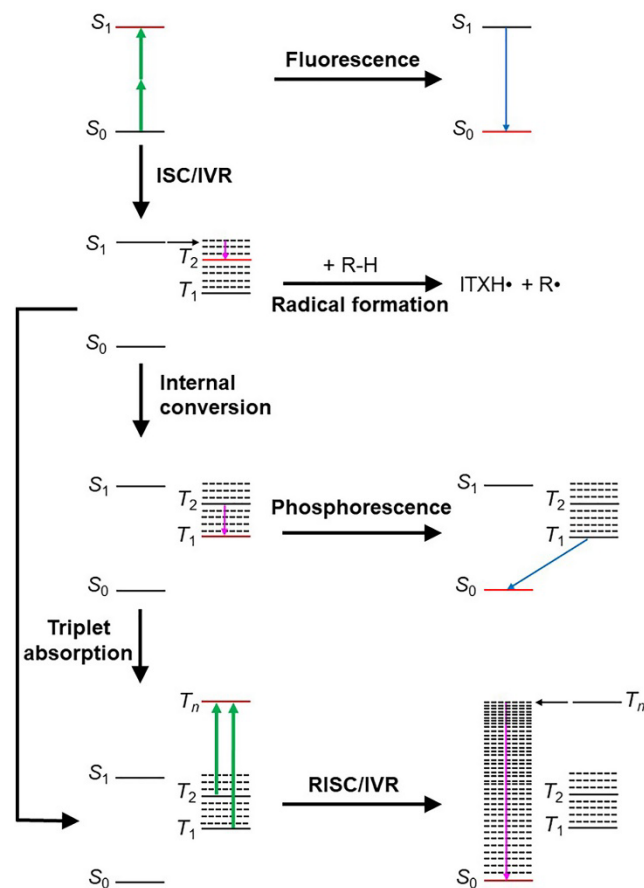


Figure 4.19 Schematic representation of the most important photophysical processes that take place in the ITX photoresist, with the relevant states ( $S_0$ ,  $S_1$ ,  $T_1$ ,  $T_2$ , and  $T_n$ ) that are involved. Green arrows indicate absorption of a photon, pink arrows indicate non-radiative relaxation, and blue arrows indicate radiative relaxation. Solid horizontal lines indicate vibrationless electronic states and dashed horizontal lines indicate vibrationally excited electronic states. The energy levels are not to scale. For each process, the final state is marked in red.

ITX is a complex model system, due to the nearly degenerate, and solvent-dependent energies of its lowest two singlet excited states and lowest two triplet states. The combination of techniques employed here enabled us to identify the initial triplet states involved in the optical deactivation of ITX, and also to ascertain the manner in which the singlet manifold is involved in the deactivation process. This pathway could not have been established unambiguously from any individual previously established technique or combination of such techniques. Furthermore, the knowledge that has been gained from our experiments and modeling provides clear

guidance for the development of new TX derivatives with improved performance for 2CL. For instance, TX derivatives with an increased energy gap between the lowest two triplet states and the next highest triplet states may not exhibit self-deactivation, which could lead to improved resolution.

The new spectroscopic toolkit presented here is broadly applicable to chemical systems that involve triplet photochemistry and photophysics. Our work demonstrates that 2-beam action spectroscopies enable the direct probing of triplet-state dynamics, and underscores the prospects for these methods to elucidate the mechanisms of complex triplet processes. The information obtained in the current study can be used to inform the synthesis of improved thioxanthone photoinitiators, but there are many other potential applications of 2-BA spectroscopies in areas of current interest in triplet dynamics. For instance, in the case of triplet–triplet annihilation upconversion,<sup>84</sup> 2-beam constant emission intensity spectroscopy offers a new approach to making precise measurements of the effective order of absorption at any given irradiance, providing a more sensitive means of determining when the linear excitation regime has been attained.<sup>85</sup>

The new spectroscopies presented here offer a clear path to characterizing and quantifying photodeactivation of triplets. If there is an observable that allows the triplet population to be determined (e.g., phosphorescence or photochemistry), then deactivation action spectroscopy can be used to determine the wavelength-dependent efficiency of deactivation. Wavelength-dependent 2-BA spectroscopies allow for the detailed probing of photochemistry and photophysics, and to identify and quantify any contributions from self-deactivation. These techniques can be used with whatever

observables are available from the system of interest (e.g., fluorescence, phosphorescence, photochemistry, or photocurrent), and comparing the results for different observables and/or conditions can give valuable information about triplet photodeactivation. The ability to extract a precise exponent at a given value of an observable provides key advantages over traditional methods of measuring optical nonlinearity. Although we used 2-BA spectroscopies here to study processes involving multiphoton absorption, which requires a pulsed laser, if the observable is not a cumulative one (i.e., fluorescence and phosphorescence, but not photochemistry), then there is no requirement that the two beams be spatially overlapped. In this case, the beams can be CW rather than pulsed.

The addition of a separate deactivation beam in 2-BA spectroscopies adds another dimension to the ability to elucidate triplet dynamics. In MAP using an ITX-based photoresist, this extra beam decreased the apparent order of nonlinearity in the system. However, the effect of the extra beam on the observed exponent is dependent on the mechanism by which triplet photodeactivation occurs. 2-BAD spectroscopies therefore have the potential to provide additional mechanistic understanding in processes in which triplet photodeactivation is involved.

The ability to elucidate pathways for the photodeactivation of triplet states will make it possible to develop new materials with improved performance for many applications. For instance, in the case of organic LEDs, triplet states are a bottleneck, because these states are electrogenerated statistically three times as often as the desired, emissive singlet states.<sup>37</sup> A common approach to solving this problem is to engineer the energies of the electronic states to promote thermal RISC from the

lowest triplet state.<sup>34</sup> However, this approach increases the effective emission lifetime of molecules, slowing the cycling of their excitation. Incorporating efficient triplet photodeactivation is another potential path toward moving population from the triplet manifold into the singlet manifold. In other applications, such as photon upconversion via triplet–triplet annihilation,<sup>84</sup> photodeactivation of triplet states is a deleterious process. It is important to be able to characterize photodeactivation in such cases, so that systems can be designed that minimize this phenomenon.

Self-deactivation of triplet states is a special case of photodeactivation that is not commonly considered in photochemistry and photophysics. Self-deactivation may be particularly important when multiphoton excitation is employed, as the irradiances used are much higher than for linear excitation, and so even a deactivation process that involves weak linear absorption can have a substantial effect. Our work here shows that self-deactivation can have a negative impact on the resolution in MAP, and the same may hold true for some other applications of multiphoton absorption, such as in 4-photon upconversion.<sup>86</sup> The characterization of the deactivation process is a key step toward developing molecules and/or choosing excitation wavelengths that minimize self-deactivation.

There are other applications in which self-deactivation is a desirable process. For example, in multiphoton fluorescence microscopy, triplet states can act as long-lived bottlenecks that reduce the fluorescence yield and increase the probability of irreversible photobleaching.<sup>87</sup> Furthermore, for fluorophores with high symmetry, the triplet yield under multiphoton excitation can be higher than that for linear excitation, because a different excited state is accessed initially; consequently, the fluorescence

quantum yield is decreased under multiphoton excitation.<sup>88</sup> Designing self-deactivation into fluorophores for multiphoton microscopy has the potential to break the triplet bottleneck, leading to more efficient emission.

## 4.5 Conclusion

We have developed a suite of optical techniques for studying triplet-state dynamics. In combination with established spectroscopic methods, these techniques make possible the identification of the states and pathways involved in complex photophysical and photochemical phenomena involving triplet states. To demonstrate the power and versatility of this expanded toolkit, we applied these techniques to study the triplet-state dynamics of ITX that are involved in the use of this material as a photoinitiator in MAP and 2-color lithography.

The studies presented here highlight the advantages of using multiphoton absorption to study triplet dynamics. The differences in selection rules for linear and 2PA for highly symmetric molecules can provide access to different excited states, which in turn can lead to differences in triplet yields. More importantly, in less symmetric molecules, one of the main advantages of multiphoton, as opposed to linear, absorption lies in the differences in triplet absorption at the excitation wavelength. In the case of linear excitation, any triplet absorption will take the molecules to a highly excited triplet state that is more likely to be reactive than are lower triplet states. On the other hand, when multiphoton absorption is used for the initial excitation, triplet absorption can involve excitation to lower-lying triplet excited states that are less reactive and more likely to lead to deactivation.

The self-deactivation process described here is likely a common phenomenon in triplet-state dynamics, particularly when multiphoton absorption is employed. As was demonstrated above, self-deactivation not only plays a role in the polymerization kinetics of ITX-based photoresists, but also in the phosphorescence of this molecule in solution. Deactivation and self-deactivation are likely to be key elements for exerting new forms of control in many processes that involve triplet-state dynamics.

## **Chapter 5 : Thin films for high-resolution, 3-color lithography**

Based on the paper by Sandra A. Gutierrez Razo, Adam Pranda, Nikolaos Liaros, Samuel R. Cohen, John T. Fourkas, Gottlieb S. Oehrlein, Hannah M. Ogden, Amy Mullin, Steven M. Wolf, Daniel Falvey, John S. Petersen. This chapter shows details on how we achieved a 40 nm thin film using acrylates that are liquid at room temperature. Further details on the substrate preparation are also discussed. For this work, I formulated the photoresist and developed the spincoating method. Adam Pranda characterized the thin films. All authors discussed the results and guided the research.

### **5.21 Abstract**

Multicolor lithography is a new class of techniques for attaining high resolution using visible, near-infrared, and/or near-ultraviolet light.<sup>53,89,90</sup> These techniques take their inspiration from recent advances in fluorescence microscopy.<sup>59</sup> The original multicolor techniques involved one color of light for exposure and a second for deactivation. However, it is now recognized that such methods have limitations due to the competition between deactivation and reaction. This problem is being addressed with a new generation of 3-color materials. One beam is used to pre-activate a photoresist, a second beam to deactivate it, and a third beam to activate the pre-activated regions that have not been deactivated. The deactivation beam is used to trim features, allowing for improved feature size and resolution.

The initial studies in 3-color lithography (3CL) employed multiphoton exposure as a means of rapid screening for promising candidate materials,<sup>4,66,91</sup> which

could be accomplished in thick films. However, large-area, semiconductor lithography applications will require the use of films that are a few tens of nanometers thick. We have developed techniques to create thin films of some of the most promising 3CL materials, and here we report the latest results on the resolution that can be attained in thin films of these materials.

To achieve uniform thin films, the substrates are first functionalized and then reacted with monomers to create a highly wettable surface. A solution of monomers and photoinitiator is spun onto the substrate to the desired thickness. The mixture of monomers is selected to have a high etch resistance, increasing fidelity during pattern transfer with plasma etching. The 3-color approach provides substantial latitude in the choice of monomers, allowing us to achieve an etch resistance that is substantially greater than that of a benchmark 193 nm resist.

## 5.22 Introduction

### 5.22 Thin film preparation

#### 5.221 Substrate functionalization

Silicon oxide ( $\text{SiO}_2$ )-coated Si wafers are used as substrates for thin film characterization, and glass coverslips are used as substrates for patterning experiments, but both substrates are prepared in the same way. The wafers and glass coverslips are functionalized and treated to increase wettability during spin-coating and to promote adhesion of the polymerized features. The substrates are first cleaned with acetone and water. After drying, the substrates are cleaned in an  $\text{O}_2$  plasma, which also exposes silanol groups to increase reactivity for the next step. Figure 5.1

shows a representation of the surface chemistry of a SiO<sub>2</sub>-coated Si wafer surface after being plasma cleaned.

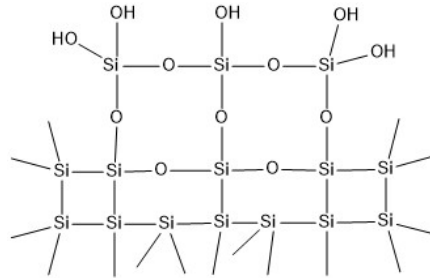


Figure 5.1 Representation of the chemical nature of a SiO<sub>2</sub>-coated Si wafer surface. The thickness of the SiO<sub>2</sub> coating is 100nm, and after plasma cleaning, silanol groups are exposed.

Figure 5.1 shows the chemical structure of (3-aminopropyl) triethoxysilane (APTES), which is used to functionalize the substrates. Our silanization procedure is adapted from optimization work done of Howarter and Youngblood.<sup>92</sup> During the first step in the silanization process, an ethoxy is replaced by a hydroxyl from water on the surface of the substrate, and ethanol leaves. A hydrogen bond forms between a hydroxyl on the silane and a hydroxyl on the surface of the substrate. Next, a condensation reaction results in a strong siloxane bond of the APTES to the surface of the substrate. From here, further hydrolysis can result in two additional siloxane bonds to the surface. The optimization work compares reaction time, silane concentration, and reaction temperature to achieve a uniform, thick layer with a high amine density. Our purpose is to have a uniform, but thin, aminated layer that is chemically bonded to the surface. A high amine density is not necessarily needed, as the amines are later reacted with monomers to create a non-labile, highly wettable surface for spin coating. Figure 5.3 shows five siloxane bonds to three APTES molecules.

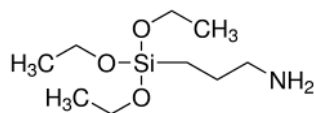


Figure 5.2 (3-Aminopropyl) triethoxysilane is used to functionalize Si wafers and glass coverslips.

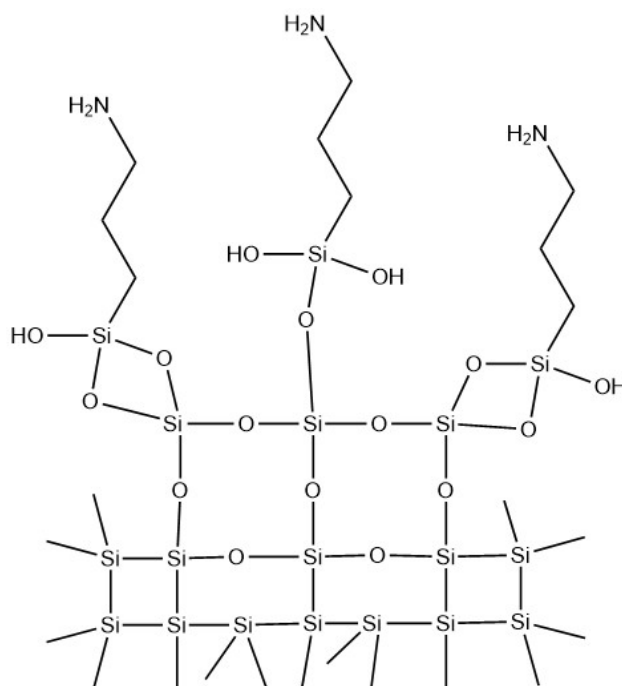


Figure 5.3 Representative schematic of the SiO<sub>2</sub>-coated Si wafer surface once functionalized with 3-(aminopropyl) triethoxysilane.

After amination, the substrates are reacted with the acrylate monomers that are used for the photoresist. Many different families of monomers could be used here, making this process versatile for 3CL films or other thin films. Figure 5.4 shows the two monomers SR368 tris[2-(acryloyloxy)ethyl] isocyanurate, and SR833 tricyclo decanedimethanol diacrylate, that are reacted with the substrates for this work. The monomers undergo Michael addition with the amines on the surface, providing strong bonds to the substrate and a compatible layer for spin coating. Figure 5.5 shows a schematic representation of the substrate after the acrylate monomers are bonded.

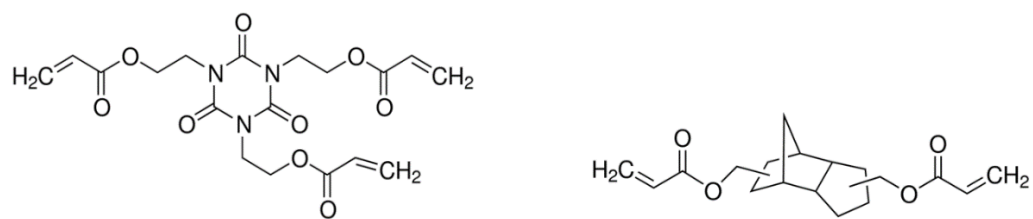


Figure 5.4 Acrylic monomers used to functionalize thin film substrates for this work. Left, SR368. Right, SR833.

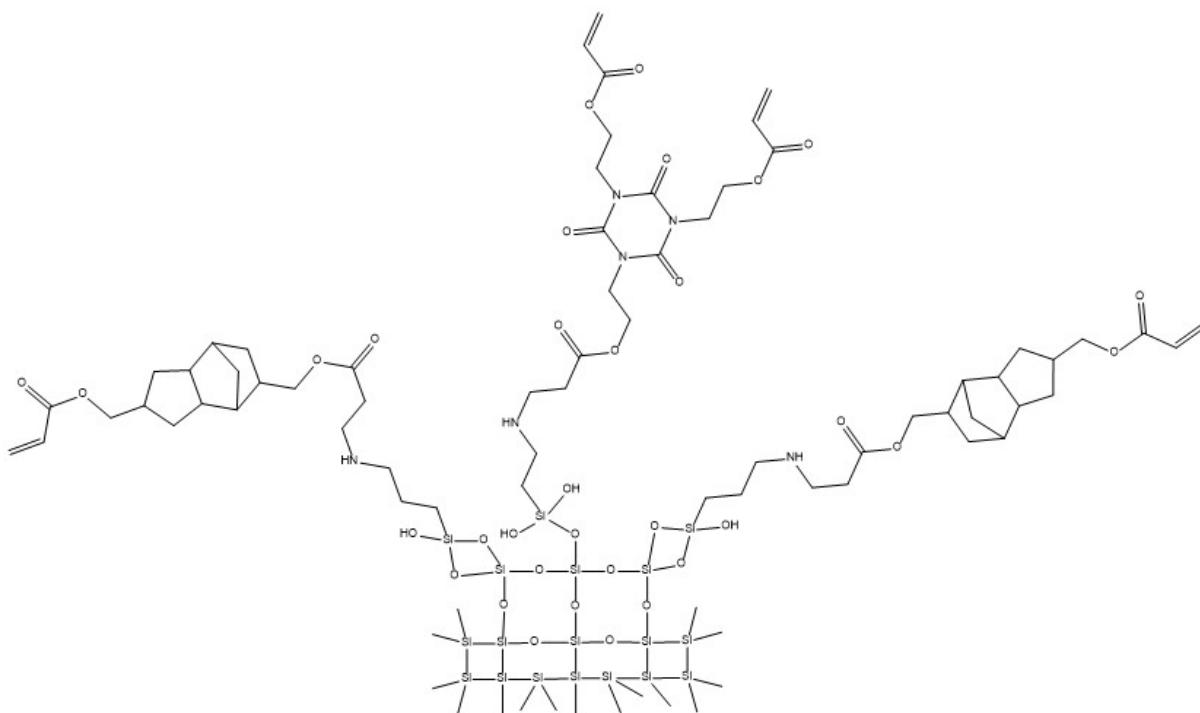


Figure 5.5 Result of Michael addition of the monomers to the functionalized substrate.

## 5.222 Spin coating and development

Once substrates are prepared, the photoresist is spun onto the substrate and dried. For film characterization, blanket exposures are performed on SiO<sub>2</sub>-coated Si wafers. The films are exposed with a UV lamp under N<sub>2</sub> flow. After development, the

thickness of these films is  $\sim 120$  nm. For fabrication, the films are spun the same way and exposed in a microscope using the 3CL technique.

## 5.23 Materials and Procedure

APTES was obtained from Sigma Aldrich and used as received. The acrylates were obtained from Sartomer and were used as received. The linked monomers and the photoinitiator are prepared in house beforehand. The  $\text{SiO}_2$  -coated Si wafers are cut into  $2 \text{ cm} \times 2 \text{ cm}$  squares, and the glass substrates are #1 coverslips. Both types of substrates are cleaned by sonicating in deionized (DI) water, acetone, then DI water again for 3 min each time. The substrates are dried for 1 h at  $100^\circ \text{C}$  and then  $\text{O}_2$  plasma cleaned at 250 mTorr for 3 min. Immediately after plasma cleaning, the substrates are submerged into a 2 wt% APTES solution in ethanol for 4 h. The substrates are rinsed well in DI water three times. The substrates are then heated to  $100^\circ \text{C}$  for 10 min to finish condensation. Afterwards, the substrates are left in a 2 vol% monomer solution in ethanol for 15 h. The substrates are rinsed for 1 h in ethanol and then dried at room temperature.

The spin-coating solution is 2 wt% photoinitiator in acrylate monomers diluted to 4 wt% photoresist with the spin-coating solvent.  $100 \mu\text{L}$  is put onto the substrate with a pipettor and is allowed to sit without spinning for 30 s. The spin coater is ramped to 1000 RPM in 30 s and spun for 60 s more to dry. The film is exposed under  $\text{N}_2$  flow with a UV spot lamp for 60 min at 40 mW. The crosslinked films are then developed in ethanol for 5 s and then are rinsed with DI water.

## 5.24 Results

### 5.241 Photoresist for 3CL

The photoinitiator used for this work has been studied in this group previously, and shown to be a good candidate for 3CL in the thick-film experiments.<sup>93-95</sup> A photoresist that is 1:1 by weight SR833:SR368 has shown 3CL behavior in thin films using multiphoton absorption for excitation, as shown in Figure 5.7. These colors are 800 nm modelocked (ML) light to pre-activate, 800 nm continuous-wave (CW) light to deactivate, and 445 nm CW light to activate to the chemically active state. A new exposure scheme for linear excitation has been identified,<sup>94</sup> but this work is ongoing. A photoresist made with linked monomers is expected to have the same 3CL behavior in thin films with the new colors for linear excitation at 405 nm ML to pre-activate, 635 nm CW to deactivate, and 445 nm CW to activate, but this work is also ongoing. Progress has also been made toward *in situ* studies using interference lithography with three colors.<sup>11</sup> Additionally, Periodic Structures, Inc. (PSI) has developed technology that will enable 3CL patterning with these materials on the wafer scale.<sup>12-16</sup>

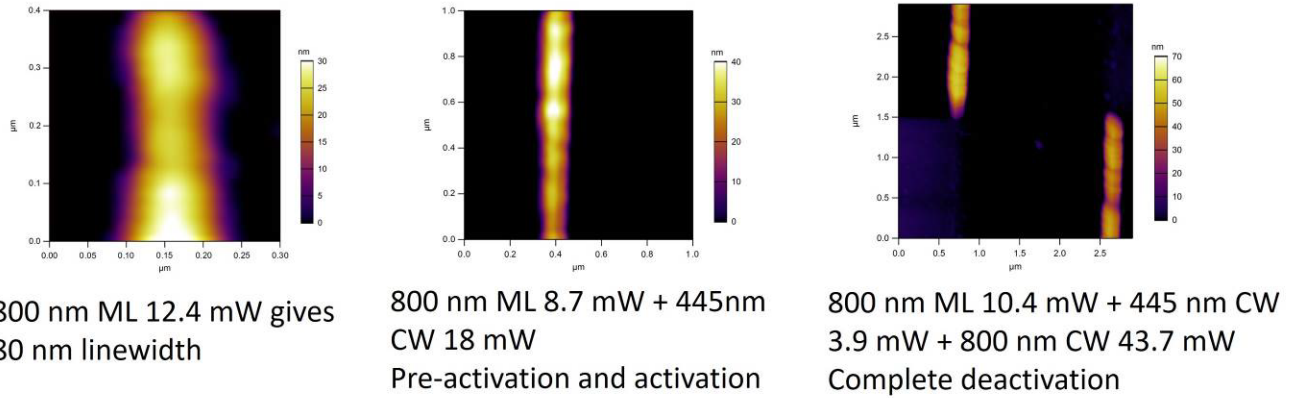


Figure 5.6 AFM images of 3CL behavior in thin films on glass cover slips. Left, 1-color exposure. Middle, 2-color exposure in which neither pre-activation nor activation alone will cause polymerization, but polymerization is observed once the beams are combined. Right, 3-color exposure with one beam pre-activating, another beam activating, and the third completely deactivating.

## 5.242 Film Characterization

Figure 5.6 shows AFM images obtained at different stages during the thin-film preparation process. The root-mean-square (RMS) roughness is 0.2 nm after functionalization with APTES. The RMS roughness increases to 0.5 nm after bonding with the monomers, and finally increases to 0.7 nm after spin-coating, exposure, and development. The roughness of the thin film made with a linked monomer resist is acceptable for fabrication and will be used in future fabrication experiments.

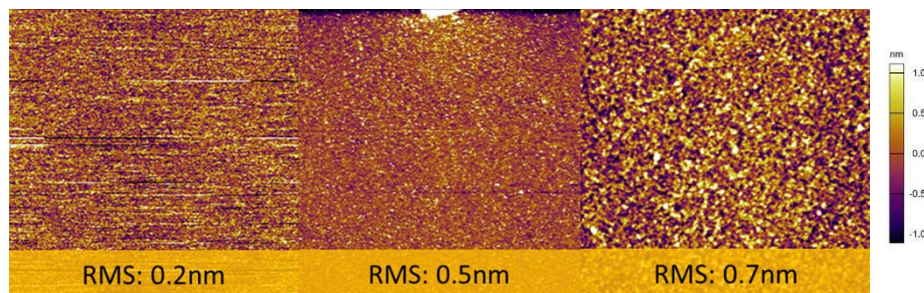


Figure 5.7. AFM images of substrates during substrate and film preparation steps. Left, RMS roughness of  $\text{SiO}_2$ -coated Si wafer after it is functionalized with APTES is 0.2 nm. Middle, RMS roughness of  $\text{SiO}_2$ -coated Si wafer after addition of monomers is 0.5 nm. Right, RMS roughness of thin film after blanket exposure and development is 0.7 nm.

The photoresist made with the linked monomers provides superior plasma etch resistance than do other photoresists we tested under identical plasma processing conditions. Our initial measurements of blanket film behavior have shown that the thickness loss during plasma etching is lower than both the benchmark JSR PR193 and thin films made with mixtures of SR833 with SR368 or SR368 with trimethylpropyltriacylate (TMPTA). Furthermore, the linked monomers attain a steady-state etch rate that is noticeably lower than that of the benchmark PR193 resist. We believe that the enhanced etch resistance of the photoresists with the linked monomers will enable us to retain high resolution during a pattern transfer process. Figure 5.8 shows the amount of film thickness etched for the materials tested as a function of processing time.

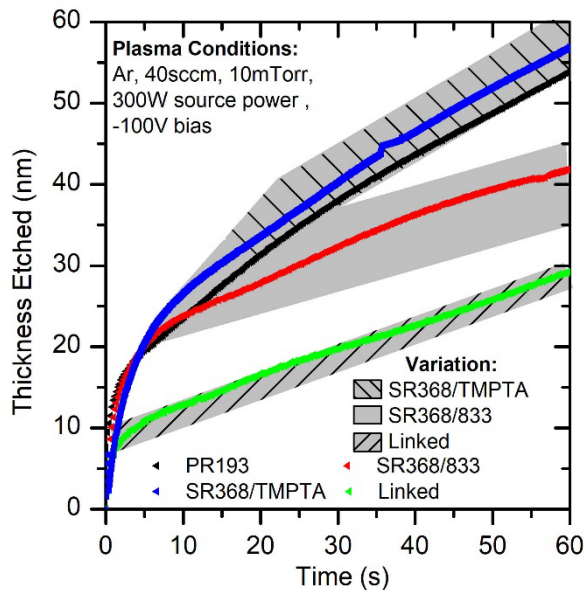


Figure 5.8 Plot of film thickness etched at the same plasma conditions: Ar, 40 sccm, 10 mTorr, 300 W source power, -100 V bias. The green symbols correspond to the film made with the linked monomers. The red symbols correspond to the Sartomer monomers mixed together. The black points correspond

to the benchmark PR193 resist. The blue symbols correspond to a mixture of SR368 with trimethylpropyltriacylate (TMPTA). The linked monomers exhibit a greater etch resistance relative to the other materials as the amount of thickness etched and etch variation is lower relative to the other materials.

## 5.25 Conclusion

In this work we have shown that the resist we have developed can work with 3CL and that we can adapt this technique into thin films that will be useful for linear excitation in large-scale patterning. We have developed a process to make smooth thin films with our resist. The etch resistance of a resist made with linked monomers should increase fidelity during the pattern transfer process. This resist shows promise for large-scale patterning, which will benefit the semiconductor industry.

## **Chapter 6 : Oxygen effects in thin films for high-resolution, 3-color lithography**

Based on a paper by Sandra A. Gutierrez Razo, Nikolaos Liaros, Adam Pranda, Gottlieb S. Oehrlein, John T. Fourkas, John S. Petersen. Once thin enough films were achieved, substantial differences in polymerization were observed between the thick and thin films. One cause for these differences is the abundance of oxygen in thin films versus thick films. For this work, I made the films and performed the experiments. All authors discussed the results and guided the research.

### 6.1 Abstract

Three-color lithography (3CL) produces features on the scale of tens of nanometers using visible light. In this technique, one beam pre-activates a photoresist, a second beam deactivates the photoresist, and a third beam activates the pre-activated regions that have not been deactivated. The deactivation beam trims features, allowing for improved feature size and resolution. Creating permeable thin films enables further control of feature size using oxygen as a quencher. We discuss these thin-film studies, which are a promising step towards large-area patterning.

### 6.2 Introduction

Inspired by recent advances in fluorescence microscopy, multicolor lithography uses two or more colors of visible and/or near-ultraviolet light to attain high resolution.<sup>53,89,90</sup> The initial approaches to multicolor lithography involved two colors of light: one for excitation and another for deactivation. With only two colors, there is competition between deactivation and chemical reaction, resulting in

resolution limitations. A new generation of 3-color materials was developed to overcome these problems. In the 3-color scheme, the first beam pre-activates the photoresist, a second beam to deactivate the region of photoresist where polymerization is not wanted, and a third beam activates the pre-activated area of the photoresist that has not been deactivated. The deactivation beam trims features, decreasing feature size and improving resolution.

Previous 3CL studies used multiphoton exposure in thick photoresist films for rapid screening of candidate materials.<sup>4,6,66</sup> In contrast, large-area semiconductor lithography applications will necessitate films that are tens of nanometers thick. After creating thin films of some of the most promising 3CL materials,<sup>96</sup> we have observed substantial differences in polymerization between the thick and thin films. Some of these differences can be attributed to the amount of oxygen present in the thin films during polymerization. Here we report our recent results on using varied oxygen concentrations in different photoresists.

Oxygen is quickly consumed in the thick films but is constantly replenished by the atmosphere in the more permeable thin films. Because oxygen is both a sensitizer and quencher in our 3CL photoresist, this problem has become an opportunity to tune the feature size and resolution by varying the oxygen concentration in the system. This effect is seen to varying extents in photoresists composed of different monomers. The 3-color approach provides substantial latitude in the choice of monomers, allowing us to select a composition that will give the best resolution when fabricating, as well as high-fidelity pattern transfer.

The 3CL technique has been used to make finer features in films that are approximately 600 nm thick; however, a problem arises when the aspect ratio of the deactivated features becomes so high that the features fall over, as seen in Figure 6.1. To decrease the aspect ratio, thin films are employed to control the height of the features, while the 3CL technique controls the  $x$  and  $y$  dimensions.

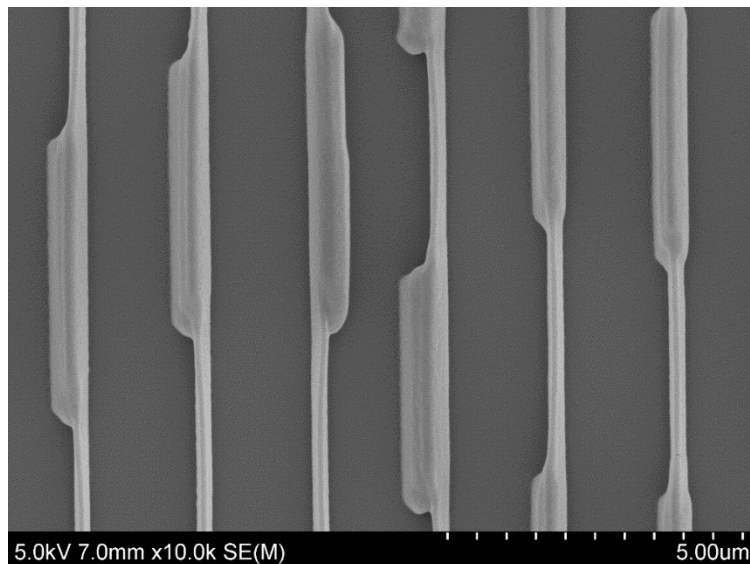


Figure 6.1 SEM image of features fabricated with the 3CL technique in 600-nm-thick films. In this case, the deactivation beam is chopped so that only parts of the features are deactivated. The deactivated portions have an aspect ratio too high to remain upright and fall to the sides upon development.

Oxygen can act as a quencher in two ways, as shown in Figure 6.2. When excited to the chemically active state, the photoinitiator can abstract a hydrogen atom and produce a radical. Oxygen can quench the triplet state before the radical is formed. If formed, the radical can start a polymerization chain reaction that can continue if unimpeded. Oxygen can scavenge the primary radical preventing polymerization, and can also terminate polymerization by producing relatively unreactive peroxides or other products.

Both mechanisms reduce the polymerization rate until the oxygen in the system is consumed. Differences in observations between thin and thick films could

be due to air permeation of the thin film, leading to constant oxygen replenishment. Oxygen can be used as a quencher to reduce feature size and increase the resolution in our thin films.

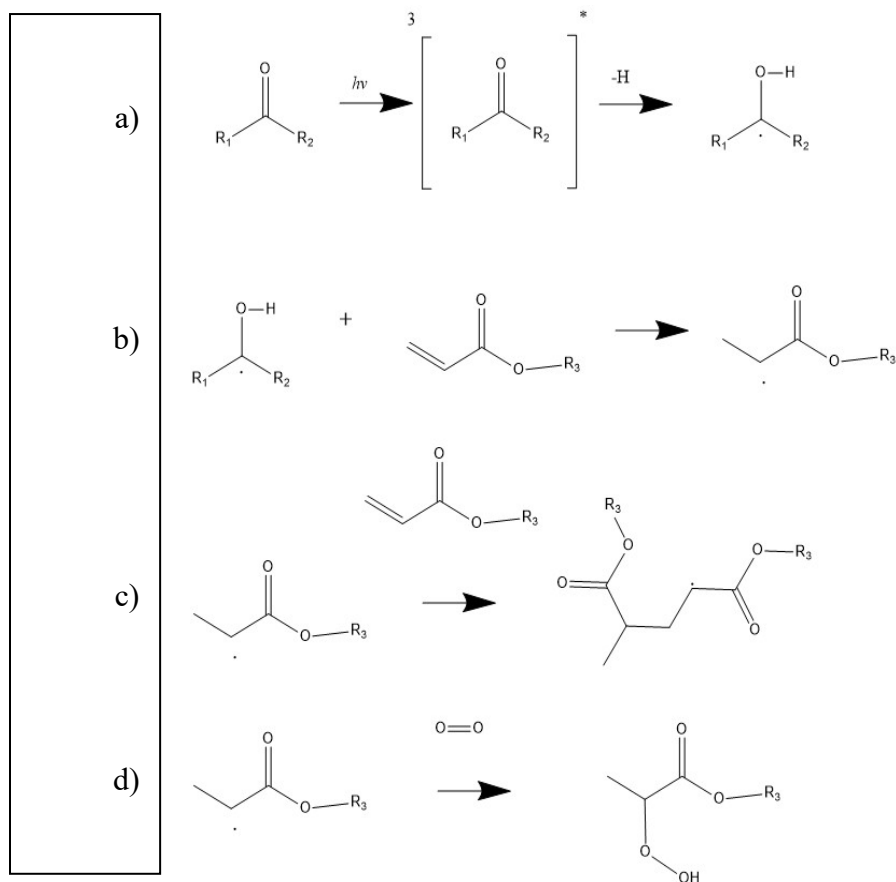


Figure 6.2 Adapted from Zhou et al.,<sup>97</sup> the figure above shows the roles of oxygen in our resist: a) hydrogen abstraction b) the start of radical polymerization c) polymerization propagation, and d) chain termination.

## 6.23 Sample preparation

### 6.231 Substrate and resist preparation

Glass coverslips are functionalized and treated to increase wettability during spin-coating and to promote adhesion of the polymerized features, as described in previous work.<sup>96</sup> For this work, the substrates are first silanized with (3-aminopropyl) triethoxysilane, as shown in Figure 5.2.

Afterwards, the substrates are reacted with the acrylate monomers that are used for the photoresist. Here, the substrates are functionalized with TMPTA, SR444, or SR833, as shown in Figure 6.3. Oxygen diffusion into the film is fast enough that the concentration of oxygen in the film is constant. Diffusion of the reactive species leads to the differences in threshold and feature size; therefore, three photoresists were made with differing viscosities to study the effect of oxygen concentration on the polymerization behavior of the thin films. The monomers for the most viscous resist at 2800 cP is a mixture of 7:3 SR368:TMPTA. SR368 is tris(2-(acryloyloxy)ethyl) isocyanurate, a waxy solid at room temperature with a density of 1.298g/cm<sup>3</sup>. TMPTA, trimethylolpropane triacrylate is a runny liquid at room temperature, with a density of 1.1g/mL, which is used to keep the mixture liquid at room temperature. The second resist is made with SR444, pentaerythritol triacrylate, also known as PETA. The density of this monomer is 1.18 g/mL, and the viscosity is 600 cP. The least viscous resist is made with SR833 tricyclo[5.2.1.0<sup>2,6</sup>]decanedimethanol diacrylate, with a density of 1.1 g/mL and a viscosity of 200 cP.

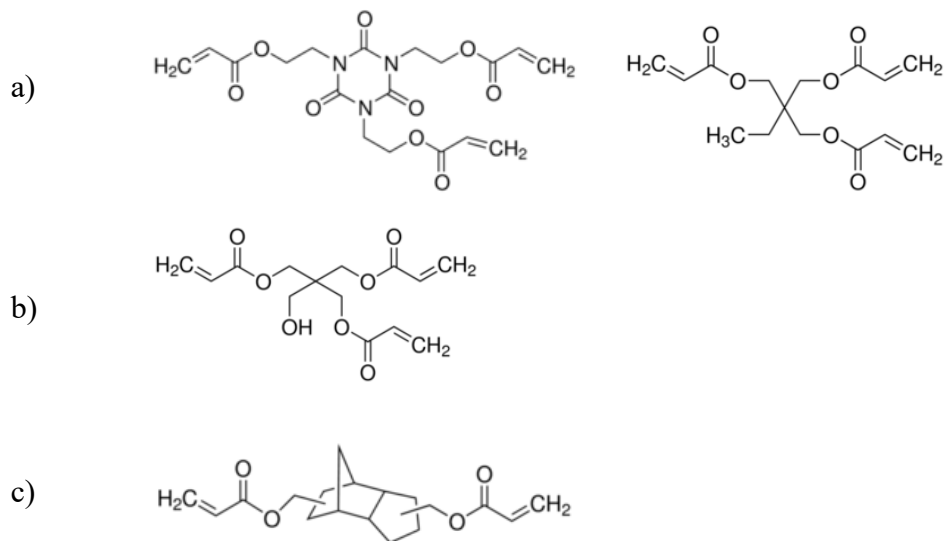


Figure 6.3 Acrylic monomers used for this work. a) SR368 and TMPTA used as a mixture for the most viscous photoresist. b) SR444, used in other multicolor lithography studies. c) SR833 used for the least viscous photoresist.

### 6.232 Spin coating and exposure

Once substrates are prepared, the photoresist is spun onto the glass coverslip and allowed to set. The thin films are put into an open air-tight sample holder. This holder is placed in a glove bag and the bag is evacuated and filled with the desired mixture of oxygen and nitrogen using flowmeters. The sample holder is closed in the glove bag before being exposed in the microscope, as shown in Figure 6.4.

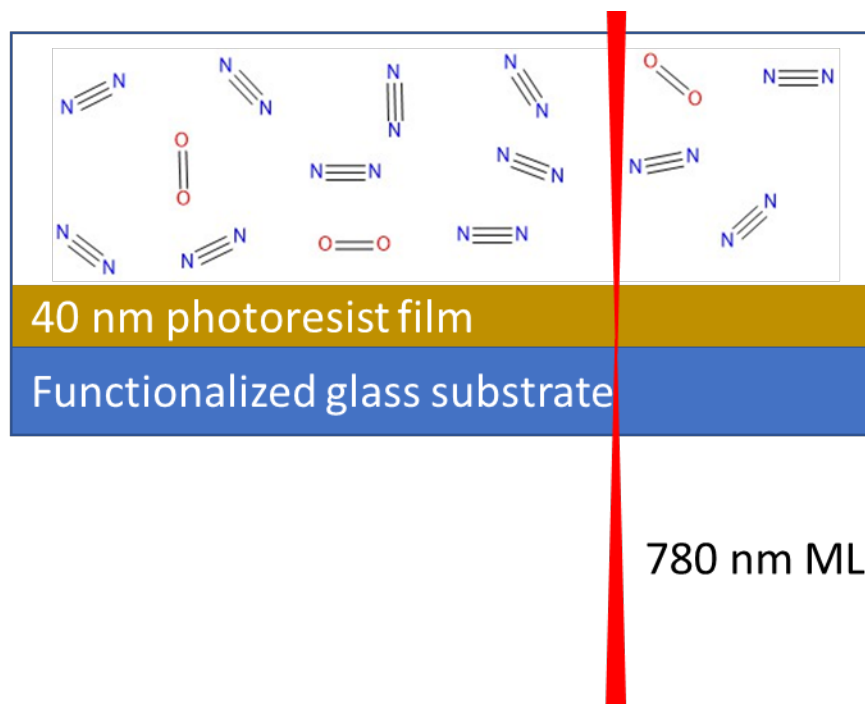


Figure 6.4 Experimental setup showing a single-beam experiment. The film is spun onto a functionalized substrate and put into an air-tight sample holder with the desired concentration of oxygen in nitrogen.

### 6.233 Materials and Procedure

APTES was obtained from Sigma Aldrich, and was used as received. The acrylates were obtained from Sartomer and Sigma Aldrich, and were also used as received. The photoinitiator is prepared in house beforehand. The glass substrates, #0 coverslips, are sonicated in deionized (DI) water, acetone, then DI water again, for 3 min each. The substrates are dried for 1 h at 100 °C, and then are O<sub>2</sub> plasma cleaned at 250 mTorr for 3 min. Immediately after plasma cleaning, the substrates are submerged into a 2 wt% APTES solution in ethanol for 4 h. The substrates are rinsed well in DI water three times. Afterwards, the substrates are left in a 2 vol% monomer solution in ethanol for 15 h. The substrates are rinsed for 1 h in ethanol and then are dried at room temperature.

The spin-coating solution is composed of the photoresist diluted with a spin-coating solvent. 60  $\mu\text{L}$  of the photoresist was dispensed on the substrate with a pipettor and allowed to sit without spinning for 30 s. The spin coater was ramped to 4000 RPM in 5 s and spun for 85 s more. The films were left in the spin-coater for 30 min to set. The film was exposed in the microscope with one 780 nm ML beam. The microscope was equipped with a camera, and the polymerization threshold was determined by eye. The threshold was noted when the monomers were crosslinked enough to cause a visible change in the refractive index of the material. The substrates were then developed in ethanol for 5 s to remove the unpolymerized monomer, and the structures were imaged by AFM to determine the linewidth.

## 6.24 Results

The polymerization threshold increases as the oxygen concentration increases for all of the photoresists tested, as shown in Figure 6.5. The most viscous material shows a larger linewidth change with increased oxygen, so higher concentrations of oxygen were investigated. Figure 6.6 shows that whereas the polymerization threshold changed as expected with the increase in oxygen, the linewidth did not continue to decrease. This discrepancy could be due to saturation, or to the observer's inability to detect the correct threshold as the dose increases with increasing oxygen concentration. More work is needed in this area. The photoinitiator used for this work has been studied in this group and was shown to be a good candidate for 3CL in previous experiments.<sup>6,93-96</sup> Although this work only used one beam to look at oxygen effects, these photoresists have shown 3CL behavior in thin films using multiphoton absorption polymerization with a 3-color exposure previously used to screen for

appropriate materials. These colors are 780 nm mode-locked (ML) light to pre-activate, 740 nm continuous-wave (CW) light to deactivate, and 445 nm CW light to activate to the chemically active state. Additionally, these photoresists are expected to have the same 3CL behavior in thin films with the new colors for linear excitation 405 nm ML to pre-activate, 635 nm CW to deactivate and 445 nm CW to activate, but this work is ongoing. Periodic Structures, Inc. (PSI) has developed technology that will enable 3CL patterning with these materials on the wafer scale.

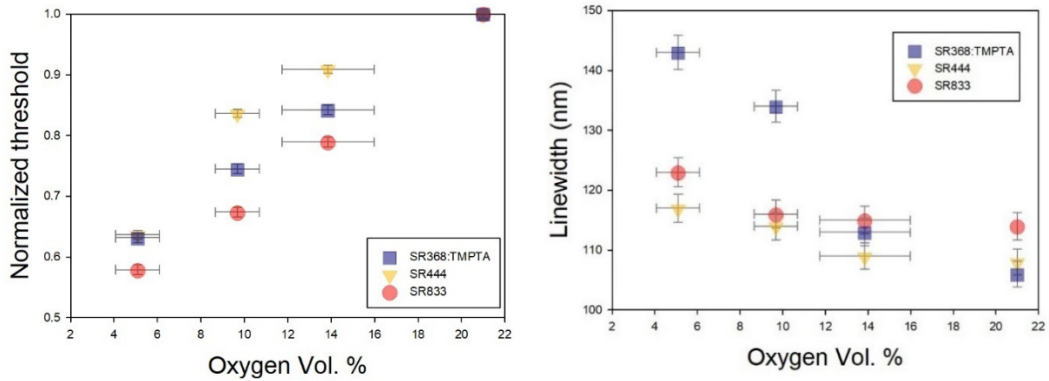


Figure 6.5 Plots of the three photoresists with varying viscosities. On the left: oxygen concentration vs polymerization threshold, right: oxygen concentration vs linewidth.

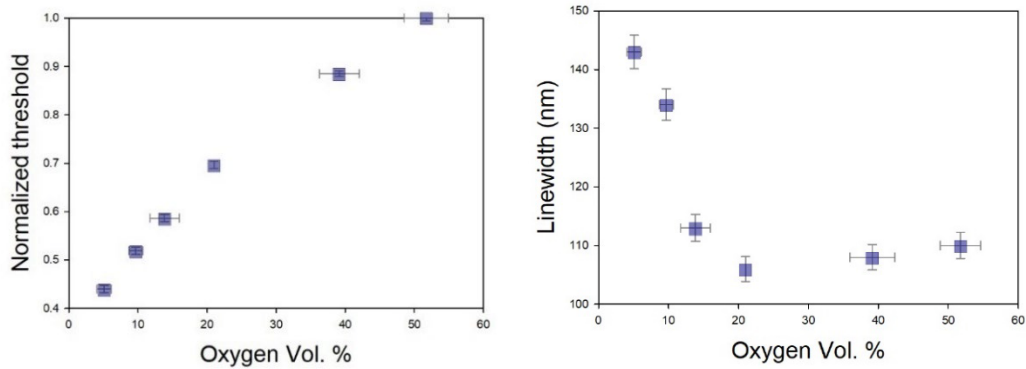


Figure 6.6 Plots of the most viscous photoresist with increased oxygen. On the left: oxygen concentration vs polymerization threshold, right: oxygen concentration vs linewidth.

## 6.25 Conclusions

In this and previous work we have shown that the resist we have developed can work with 3CL and that we can adapt this technique into thin films that will be useful for linear excitation in large-scale patterning. We are able to use oxygen as a quencher to further refine features size to increase resolution. This resist shows promise for large-scale patterning that will benefit the semiconductor industry. Future work will include 3CL exposure under increased oxygen concentration conditions.

## Chapter 7 : Impact and Future work

This work describes:

- 2-BIT, a technique to determine the order of nonlinearity of materials that could be used as photoinitiators in a 3CL system,
- ITX's performance as a 3CL photoinitiator,
- the procedure to produce 40 nm thin films,
- differences in polymerization and deactivation in thin films compared to micron-thick films.

Having learned so much about our photoinitiator and its behavior, future students can endeavor to increase fabrication resolution for 3CL. The 3CL technique can be developed further and scaled for production. ITX and its analogues can also be reformulated into innumerable photoresist systems or other systems that require controlled radical polymerization.

The photoresist for the 3CL project was formulated for thin films with high etch resistivity. Polymers with high etch resistivity have a larger percentage of C-C bonds and tend to be less viscous compared to ethoxylated acrylate monomers. Although not as etch resistant, ethoxylated acrylate monomers can create finer features because higher viscosity means there is less diffusion of the partially polymerized oligomers. Highly ethoxylated acrylate monomers could enable higher resolution polymerization.

In addition to trying different monomers for higher resolution, the 3CL can be developed further for other applications. One interesting avenue to pursue is a water soluble system. Although ITX is not soluble in water, it could be modified to increase its solubility. This modification could then open an path to a bio-compatible 3CL system.

Photoinitiator modifications can increase 3CL applications, but 3CL can also be done with other photoinitiators altogether. I have recently seen deactivation in acrylates with a photoacid generating initiator. The 3CL technique can be developed for many applications using different monomers and photoinitiators.

## **Appendices**

### **A. Deactivation beam characterization**

For 3 or even 2 color lithography experiments, we use a shaped deactivation beam to deactivate the outside edges of the exposed area, allowing for polymerization only in the center of the exposed area. Figure A.1 shows a simplified schematic of the ARCoTix polarization converter used for this work. This polarization converter gives a donut-shaped beam with a dark spot in the middle.

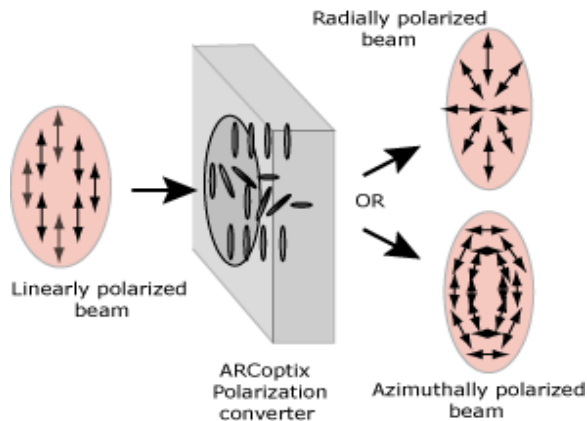


Figure A.1<sup>98</sup> Effect of ARCOptix polarization converter. The polarization converter contains a liquid crystal retardant material that can be controlled by changing the voltage applied to convert a linearly polarized beam into a radially or azimuthally polarized beam.

Throughout this project, we observed that deactivation seems to be related to the distance of the focus from the substrate. For example, we see that features that are thinner in  $x$  are also shorter in  $z$  compared to features fabricated without the deactivation beam. We used a GaAsP photodiode to characterize the shaped deactivation beam and found results consistent with our observations.

In addition to the beam we characterize, we use a beam controlled with scanning mirrors to move across the deactivation beam. Once both beam foci are overlapped, they are focused on the photodiode. A chopper is positioned in such a way so that one beam passes through the inner part of the wheel and the other beam passes through the outer part. This way, the beams are chopped at different frequencies. The lock-in amplifier is set to detect only the signal from the combination of both beams. The signal from the individual beams is subtracted as shown in Figure A.2. The beams start out next to each other and as the scanning mirrors move one beam over the other, the signal changes and is recorded.

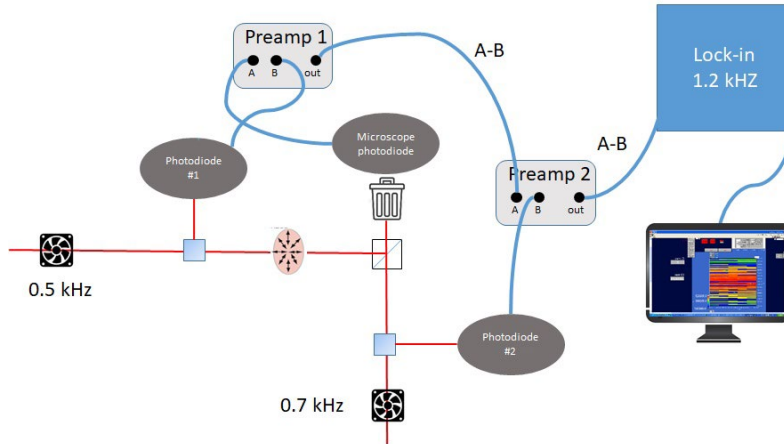


Figure A.2 Setup for beam characterization experiments. This setup involves two preamplifiers to subtract the individual signals from the beams. This way, the lock-in amplifier is sensitive to only the combined signal.

We expect the highest signal when the bright areas of the beams are overlapped. The signal from the lock-in amplifier is plotted against the position of the scanning beam to show the profile of the deactivation beam. To clarify, the signal from the lock-in amplifier is also in volts because it is the output of the lock-in amplifier and is not related to the voltage applied to the polarization converter. Figure A.3 shows the profile of the deactivation beam when there is 0 voltage applied to the polarization converter. Here we see that the highest signal comes from the middle of the peak because the shape is largely unaffected. When the voltage is 0, both beams are brightest in the center so Figure A.3 shows a peak in the middle.

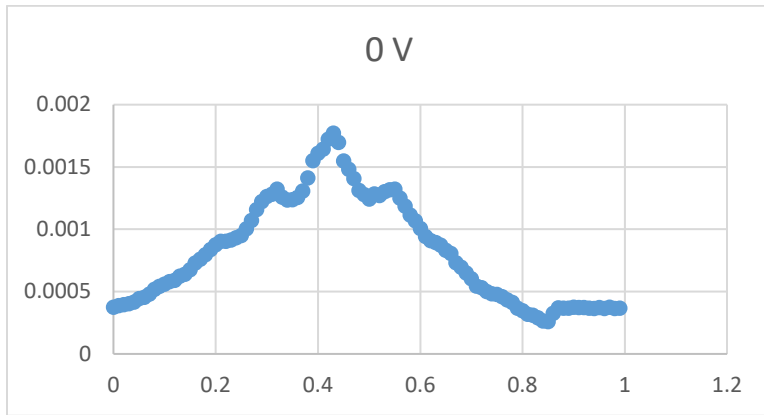


Figure A.3 Profile of the deactivation beam passing through the polarization converter with 0 voltage applied. The peak shows that both beams are brightest in the middle.

The voltage for a radially polarized beam was determined to be 1.567 V. This value changes over time, so it is important to confirm the shape of the beam by eye.

Figure A.4 shows the profile of the radially polarized deactivation beam. Here we can see two peaks. These peaks are the brightest areas of the shaped beam and we can see the profile of the donut hole in between the peaks.

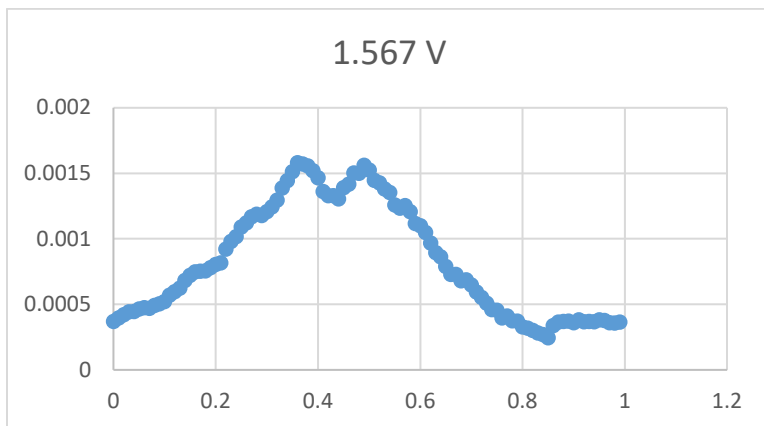


Figure A.4 Profile of the radially polarized beam.

Moving the objective into the photodiode gives different values, so we tried to find a position that shows a larger donut hole. The results in Figure A.5 shows scans at different  $z$  positions as I moved the objective closer to the photodiode.

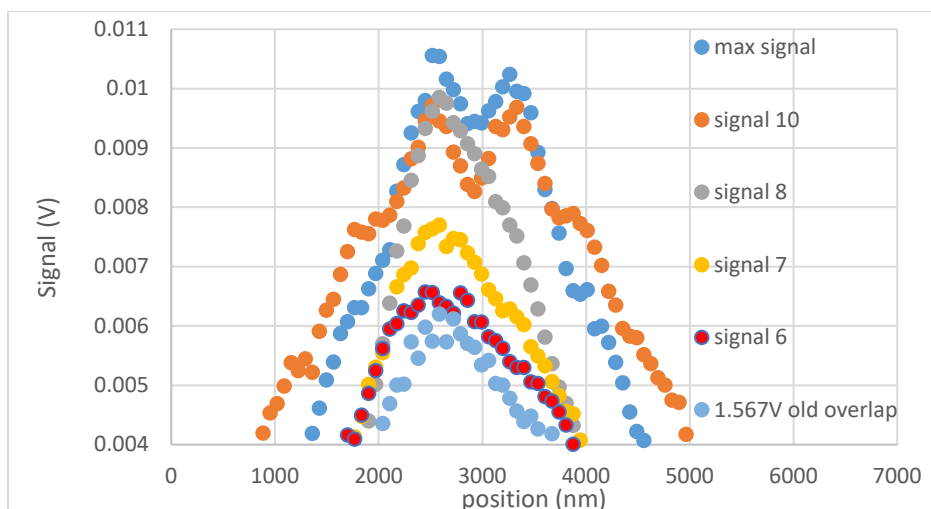


Figure A.5 Radially polarized beam profiles at different  $z$  positions. After each scan, the position of the objective moved closer to the photodiode. The exact relative position could not be determined because the photodiode holder can move. I relied on the signal of the amplifier to decide how far into the photodiode I moved the objective.

We can see a clear difference in the deactivation beam based on the voltage applied to the polarization converter, but the signal does not change much when making small adjustments to the voltage. We can also see that the hole is not as deep and dark as we hoped. These results are consistent with deactivated features being narrower as well as shorter than features that are not deactivated.

## B. APTES procedure

Both the glass coverslips used for microscope exposures experiments and the silicon oxide-coated silicon wafers are prepared in the same way. The substrates are functionalized to increase wettability during spin coating and to promote polymer adhesion to the substrate.

The substrates are sonicated for 3 min each time in deionized water to remove dust, then in acetone to remove most organic impurities, then again in water as acetone can dry too fast and leave a residue behind. After drying in a 100°C oven for

1 h, the substrates are cleaned in O<sub>2</sub> plasma at 250 mTorr for 3 min, exposing silanol groups to increase reactivity for the next step.

The substrates are then functionalized with (3-aminopropyl) triethoxysilane (APTES) using an adapted method. The substrates are submerged in a 2 vol.% solution of APTES in ethanol for 2 h. Water is not added to the solution, but small amounts of water in the ethanol and the substrate surface facilitate a substitution of an ethoxy group on the silane. A hydrogen bond forms between a hydroxyl on the silane and a hydroxyl on the surface of the substrate. A condensation reaction results in a siloxane bond to the substrate. Further hydrolysis may result in multiple siloxane bonds.

APTES is water sensitive, and will aggregate if not kept dry. Aggregates increase the roughness of the substrate and in turn the roughness of the thin film resulting in bumps around the polymerized features that affect the height of the features. APTES must be stored under dry gas. As the solution stands, moisture is absorbed from the air and continues to form APTES aggregates. Limiting the reaction time of APTES is necessary to obtain smooth thin films as can be seen in. The solution is only good for one functionalization.

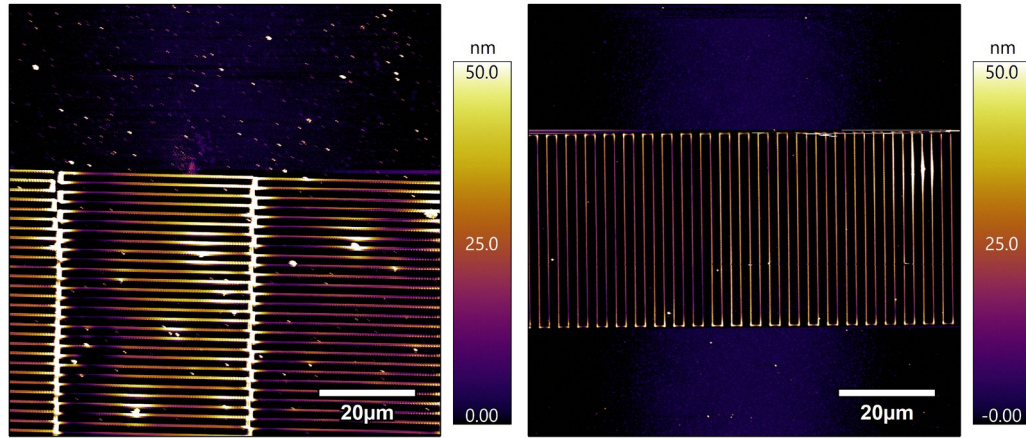


Figure B.1 AFM images of thin films with fabricated features. On the left, fabricated features made on a substrate using a 4 hour APTES reaction. The APTES aggregates appear as white spots and are present everywhere on the substrate. The aggregate spots change the height of the thin film and the height and width of lines fabricated around them. On the right, fabricated features made on a substrate using a 2 hour APTES reaction. Here, there are far fewer aggregates on the substrate.





## Bibliography

- 1 Arnold, F., Prabhakar, A. & Zuber, M. T. Report to the President. Revitalizing the U.S. Semiconductor Ecosystem. (2022).
- 2 Maruo, S., Nakamura, O. & Kawata, S. Three-dimensional microfabrication with two-photon-absorbed photopolymerization. *Optics Letters* **22**, 132 (1997). <https://doi.org:10.1364/ol.22.000132>
- 3 Baldacchini, T. Three-Dimensional Microfabrication Using Two-photon Polymerization. *Three-Dimensional Microfabrication Using Two-photon Polymerization*, xxiii-xxvi (2016). <https://doi.org:10.1016/b978-0-323-35321-2.00027-3>
- 4 LaFratta, C. N., Fourkas, J. T., Baldacchini, T. & Farrer, R. A. Multiphoton Fabrication. *Angewandte Chemie International Edition* **46**, 6238-6258 (2007). <https://doi.org:10.1002/anie.200603995>
- 5 Malinauskas, M., Farsari, M., Piskarskas, A. & Juodkazis, S. Ultrafast laser nanostructuring of photopolymers: A decade of advances. *Physics Reports* **533**, 1-31 (2013). <https://doi.org:10.1016/j.physrep.2013.07.005>
- 6 Maruo, S. & Fourkas, J. T. Recent progress in multiphoton microfabrication. *Laser & Photonics Review* **2**, 100-111 (2008). <https://doi.org:10.1002/lpor.200710039>
- 7 Cumpston, B. H. *et al.* Two-photon polymerization initiators for three-dimensional optical data storage and microfabrication. *Nature* **398**, 51-54 (1999). <https://doi.org:10.1038/17989>
- 8 Schafer, K. J. *et al.* Two-photon absorption cross-sections of common photoinitiators. *Journal of Photochemistry and Photobiology A: Chemistry* **162**, 497-502 (2004). [https://doi.org:10.1016/s1010-6030\(03\)00394-0](https://doi.org:10.1016/s1010-6030(03)00394-0)
- 9 Fischer, J. *et al.* Exploring the Mechanisms in STED-Enhanced Direct Laser Writing. *Advanced Optical Materials* **3**, 221-232 (2014). <https://doi.org:10.1002/adom.201400413>
- 10 de Araújo, C. B., Gomes, A. S. L. & Boudebs, G. Techniques for nonlinear optical characterization of materials: a review. *Reports on Progress in Physics* **79**, 036401 (2016). <https://doi.org:10.1088/0034-4885/79/3/036401>
- 11 Haske, W. *et al.* 65 nm feature sizes using visible wavelength 3-D multiphoton lithography. *Optics Express* **15**, 3426 (2007). <https://doi.org:10.1364/oe.15.003426>
- 12 Fischer, J. *et al.* Three-dimensional multi-photon direct laser writing with variable repetition rate. *Optics Express* **21**, 26244 (2013). <https://doi.org:10.1364/oe.21.026244>
- 13 Mueller, J. B., Fischer, J., Mayer, F., Kadic, M. & Wegener, M. Polymerization Kinetics in Three-Dimensional Direct Laser Writing. *Advanced Materials* **26**, 6566-6571 (2014). <https://doi.org:10.1002/adma.201402366>
- 14 Colley, C. S. *et al.* Probing the Reactivity of Photoinitiators for Free Radical Polymerization: Time-Resolved Infrared Spectroscopic Study of Benzoyl Radicals. *Journal of the American Chemical Society* **124**, 14952-14958 (2002). <https://doi.org:10.1021/ja026099m>

- 15 Farrer, R. A., Butterfield, F. L., Chen, V. W. & Fourkas, J. T. Highly Efficient Multiphoton-Absorption-Induced Luminescence from Gold Nanoparticles. *Nano Letters* **5**, 1139-1142 (2005). <https://doi.org:10.1021/nl050687r>
- 16 Baldacchini, T. *et al.* Acrylic-based resin with favorable properties for three-dimensional two-photon polymerization. *Journal of Applied Physics* **95**, 6072-6076 (2004). <https://doi.org:10.1063/1.1728296>
- 17 Wu, S., Straub, M. & Gu, M. Single-monomer acrylate-based resin for three-dimensional photonic crystal fabrication. *Polymer* **46**, 10246-10255 (2005). <https://doi.org:10.1016/j.polymer.2005.08.030>
- 18 Mendonca, C. R., Correa, D. S., Baldacchini, T., Tayalia, P. & Mazur, E. Two-photon absorption spectrum of the photoinitiator Lucirin TPO-L. *Applied Physics A* **90**, 633-636 (2007). <https://doi.org:10.1007/s00339-007-4367-0>
- 19 Serbin, J. *et al.* Femtosecond laser-induced two-photon polymerization of inorganic-organic hybrid materials for applications in photonics. *Optics Letters* **28**, 301 (2003). <https://doi.org:10.1364/ol.28.000301>
- 20 Jhaveri, S. J. *et al.* Direct three-dimensional microfabrication of hydrogels via two-photon lithography in aqueous solution. *Chem Mater* **21**, 2003-2006 (2009). <https://doi.org:10.1021/cm803174e>
- 21 Szabo, A. & Ostlund, N. S. *Modern quantum chemistry: introduction to advanced electronic structure theory.* (Courier Corporation, 2012).
- 22 Evans, D. F., Warhurst, E. & Roe, E. M. F. The effect of environment on singlet-triplet transitions of organic molecules. *Proceedings of the Royal Society of London. Series A. Mathematical and Physical Sciences* **255**, 55-63 (1960). <https://doi.org:10.1098/rspa.1960.0049>
- 23 Chang, Y.-L. *et al.* Highly Efficient Warm White Organic Light-Emitting Diodes by Triplet Exciton Conversion. *Advanced Functional Materials* **23**, 705-712 (2012). <https://doi.org:10.1002/adfm.201201858>
- 24 Zhao, H. & Mazumdar, S. Electron-Electron Interaction Effects on the Optical Excitations of Semiconducting Single-Walled Carbon Nanotubes. *Physical Review Letters* **93**, 157402 (2004). <https://doi.org:10.1103/PhysRevLett.93.157402>
- 25 Rauch, M. P. & Knowles, R. R. Applications and Prospects for Triplet-Triplet Annihilation Photon Upconversion. *CHIMIA* **72**, 501 (2018). <https://doi.org:10.2533/chimia.2018.501>
- 26 Bretschneider, S., Eggeling, C. & Hell, S. W. Breaking the Diffraction Barrier in Fluorescence Microscopy by Optical Shelving. *Physical Review Letters* **98**, 218103 (2007). <https://doi.org:10.1103/PhysRevLett.98.218103>
- 27 Zhao, J., Wu, W., Sun, J. & Guo, S. Triplet photosensitizers: from molecular design to applications. *Chemical Society Reviews* **42**, 5323-5351 (2013). <https://doi.org:10.1039/C3CS35531D>
- 28 Chi, T. *et al.* Tailored thioxanthone-based photoinitiators for two-photon-controllable polymerization and nanolithographic printing. *Journal of Polymer Science Part B: Polymer Physics* **57**, 1462-1475 (2019). <https://doi.org:10.1002/polb.24891>

- 29 Harke, B. *et al.* Polymerization Inhibition by Triplet State Absorption for Nanoscale Lithography. *Advanced Materials* **25**, 904-909 (2013). <https://doi.org/10.1002/adma.201204141>
- 30 Marian, C. M. Spin-orbit coupling and intersystem crossing in molecules. *WIREs Computational Molecular Science* **2**, 187-203 (2012). <https://doi.org/10.1002/wcms.83>
- 31 Steiner, U. & Winter, G. Position dependent heavy atom effect in physical triplet quenching by electron donors. *Chemical Physics Letters* **55**, 364-368 (1978). [https://doi.org/10.1016/0009-2614\(78\)87040-7](https://doi.org/10.1016/0009-2614(78)87040-7)
- 32 Romanovskii, Y. V. *et al.* Phosphorescence of  $\pi$ -Conjugated Oligomers and Polymers. *Physical Review Letters* **84**, 1027-1030 (2000). <https://doi.org/10.1103/PhysRevLett.84.1027>
- 33 Carmichael, I. & Hug, G. L. Triplet-Triplet Absorption Spectra of Organic Molecules in Condensed Phases. *Journal of Physical and Chemical Reference Data* **15**, 1-250 (1986). <https://doi.org/10.1063/1.555770>
- 34 Yang, Z. *et al.* Recent advances in organic thermally activated delayed fluorescence materials. *Chemical Society Reviews* **46**, 915-1016 (2017). <https://doi.org/10.1039/C6CS00368K>
- 35 Stranius, K., Hertzog, M. & Börjesson, K. Selective manipulation of electronically excited states through strong light-matter interactions. *Nat Commun* **9**, 2273 (2018). <https://doi.org/10.1038/s41467-018-04736-1>
- 36 Patterson, L. K., Porter, G. & Topp, M. R. Oxygen quenching of singlet and triplet states. *Chemical Physics Letters* **7**, 612-614 (1970). [https://doi.org/10.1016/0009-2614\(70\)87019-1](https://doi.org/10.1016/0009-2614(70)87019-1)
- 37 Baldo, M. A., Adachi, C. & Forrest, S. R. Transient analysis of organic electrophosphorescence. II. Transient analysis of triplet-triplet annihilation. *Physical Review B* **62**, 10967-10977 (2000). <https://doi.org/10.1103/physrevb.62.10967>
- 38 Smith, M. B. & Michl, J. Singlet Fission. *Chemical Reviews* **110**, 6891-6936 (2010). <https://doi.org/10.1021/cr1002613>
- 39 Lower, S. K. & El-Sayed, M. A. The Triplet State and Molecular Electronic Processes in Organic Molecules. *Chemical Reviews* **66**, 199-241 (1966). <https://doi.org/10.1021/cr60240a004>
- 40 Strömqvist, J. *et al.* Quenching of Triplet State Fluorophores for Studying Diffusion-Mediated Reactions in Lipid Membranes. *Biophysical Journal* **99**, 3821-3830 (2010). <https://doi.org/10.1016/j.bpj.2010.09.059>
- 41 Buck, J. T. *et al.* Spin-Allowed Transitions Control the Formation of Triplet Excited States in Orthogonal Donor-Acceptor Dyads. *Chem* **5**, 138-155 (2019). <https://doi.org/10.1016/j.chempr.2018.10.001>
- 42 Ge, J. *et al.* Bringing light into the dark triplet space of molecular systems. *Physical Chemistry Chemical Physics* **17**, 13129-13136 (2015). <https://doi.org/10.1039/C5CP00323G>
- 43 Angulo, G. *et al.* Ultrafast Decay of the Excited Singlet States of Thioxanthone by Internal Conversion and Intersystem Crossing. *ChemPhysChem* **11**, 480-488 (2010). <https://doi.org/10.1002/cphc.200900654>

- 44 Mundt, R. *et al.* Thioxanthone in apolar solvents: ultrafast internal conversion precedes fast intersystem crossing. *Physical Chemistry Chemical Physics* **18**, 6637-6647 (2016). <https://doi.org/10.1039/C5CP06849E>
- 45 Rai-Constapel, V., Villnow, T., Ryseck, G., Gilch, P. & Marian, C. M. Chimeric Behavior of Excited Thioxanthone in Protic Solvents: II. Theory. *The Journal of Physical Chemistry A* **118**, 11708-11717 (2014). <https://doi.org/10.1021/jp5099415>
- 46 Villnow, T., Ryseck, G., Rai-Constapel, V., Marian, C. M. & Gilch, P. The Chimeric Behaviour of Excited Thioxanthone in Protic Solvents: I. Experiments. *J. Phys. Chem. A* (2014).
- 47 Fischer, J., von Freymann, G. & Wegener, M. The Materials Challenge in Diffraction-Unlimited Direct-Laser-Writing Optical Lithography. *Advanced Materials* **22**, 3578-3582 (2010). [https://doi.org:https://doi.org/10.1002/adma.201000892](https://doi.org/https://doi.org/10.1002/adma.201000892)
- 48 Harke, B., Bianchini, P., Brandi, F. & Diaspro, A. Photopolymerization Inhibition Dynamics for Sub-Diffraction Direct Laser Writing Lithography. *ChemPhysChem* **13**, 1429-1434 (2012). [https://doi.org:https://doi.org/10.1002/cphc.201200006](https://doi.org/https://doi.org/10.1002/cphc.201200006)
- 49 Farsari, M. & Chichkov, B. N. Two-photon fabrication. *Nature Photonics* **3**, 450-452 (2009). <https://doi.org/10.1038/nphoton.2009.131>
- 50 Fourkas, J. T. in *Three-Dimensional Microfabrication Using Two-photon Polymerization* (ed Tommaso Baldacchini) 45-61 (William Andrew Publishing, 2016).
- 51 Sugioka, K. & Cheng, Y. *Light: Sci. Appl.* **3**, e149 (2014).
- 52 Hell, S. W. Far-Field Optical Nanoscopy. *Science* **316**, 1153-1158 (2007). <https://doi.org/doi:10.1126/science.1137395>
- 53 Klar, T. A. & Hell, S. W. Subdiffraction resolution in far-field fluorescence microscopy. *Optics Letters* **24**, 954-956 (1999). <https://doi.org/10.1364/ol.24.000954>
- 54 Klar, T. A., Jakobs, S., Dyba, M., Egner, A. & Hell, S. W. Fluorescence microscopy with diffraction resolution barrier broken by stimulated emission. *Proceedings of the National Academy of Sciences* **97**, 8206-8210 (2000). <https://doi.org/doi:10.1073/pnas.97.15.8206>
- 55 Fourkas, J. T. STED-inspired approaches to resolution enhancement. *Multiphoton Lithography: Techniques, Materials, and Applications*, 1756 (2016).
- 56 Gan, Z., Cao, Y., Evans, R. A. & Gu, M. Three-dimensional deep sub-diffraction optical beam lithography with 9 nm feature size. *Nat Commun* **4**, 2061 (2013). <https://doi.org/10.1038/ncomms3061>
- 57 Li, L., Gattass, R. R., Gershgoren, E., Hwang, H. & Fourkas, J. T. Achieving Lambda/20 Resolution by One-Color Initiation and Deactivation of Polymerization. *Science* **324**, 910 (2009). <https://doi.org/doi:10.1126/science.1168996>
- 58 Liaros, N. & Fourkas, J. T. Ten years of two-color photolithography [Invited]. *Optical Materials Express* **9**, 3006-3020 (2019). <https://doi.org/10.1364/OME.9.003006>

- 59 Fourkas, J. T. & Petersen, J. S. 2-Colour photolithography. *Physical Chemistry Chemical Physics* **16**, 8731-8750 (2014).  
<https://doi.org:10.1039/C3CP52957F>
- 60 Chi, T. *et al.* Substituted Thioxanthone-Based Photoinitiators for Efficient Two-Photon Direct Laser Writing Polymerization with Two-Color Resolution. *ACS Applied Polymer Materials* **3**, 1426-1435 (2021).  
<https://doi.org:10.1021/acsapm.0c01291>
- 61 Fischer, J. & Wegener, M. Three-dimensional direct laser writing inspired by stimulated-emission-depletion microscopy [Invited]. *Optical Materials Express* **1**, 614-624 (2011). <https://doi.org:10.1364/OME.1.000614>
- 62 Wolf, T. J. A., Fischer, J., Wegener, M. & Unterreiner, A.-N. Pump&#x2013;probe spectroscopy on photoinitiators for stimulated-emission-depletion optical lithography. *Optics Letters* **36**, 3188-3190 (2011).  
<https://doi.org:10.1364/OL.36.003188>
- 63 Andrzejewska, E., Zych-Tomkowiak, D., Andrzejewski, M., Hug, G. L. & Marciniak, B. Heteroaromatic Thiols as Co-initiators for Type II Photoinitiating Systems Based on Camphorquinone and Isopropylthioxanthone. *Macromolecules* **39**, 3777-3785 (2006).  
<https://doi.org:10.1021/ma060240k>
- 64 Kuebler, S. M. *et al.* in *Technical Digest. Summaries of papers presented at the Conference on Lasers and Electro-Optics. Postconference Edition. CLEO'99. Conference on Lasers and Electro-Optics (IEEE Cat. No. 99CH37013)*. 107-108 (IEEE).
- 65 Fischer, J. *et al.* Exploring the Mechanisms in STED-Enhanced Direct Laser Writing. *Advanced Optical Materials* **3**, 221-232 (2015).  
<https://doi.org:https://doi.org/10.1002/adom.201400413>
- 66 Tomova, Z., Liaros, N., Gutierrez Razo, S. A., Wolf, S. M. & Fourkas, J. T. In situ measurement of the effective nonlinear absorption order in multiphoton photoresists. *Laser & Photonics Reviews* **10**, 849-854 (2016).  
<https://doi.org:10.1002/lpor.201600079>
- 67 Liaros, N., Cohen, S. R. & Fourkas, J. T. Determination of the contributions of two simultaneous absorption orders using 2-beam action spectroscopy. *Optics Express* **26**, 9492-9501 (2018). <https://doi.org:10.1364/oe.26.009492>
- 68 Liaros, N., Gutierrez Razo, S. A. & Fourkas, J. T. Probing Multiphoton Photophysics Using Two-Beam Action Spectroscopy. *The Journal of Physical Chemistry A* **122**, 6643-6653 (2018). <https://doi.org:10.1021/acs.jpca.8b04463>
- 69 Liaros, N. & Fourkas, J. T. Methods for Determining the Effective Order of Absorption in Radical Multiphoton Photoresists: A Critical Analysis. *Laser & Photonics Reviews* **15**, 2000203 (2021).  
<https://doi.org:https://doi.org/10.1002/lpor.202000203>
- 70 Yang, L. *et al.* On the Schwarzschild Effect in 3D Two-Photon Laser Lithography. *Advanced Optical Materials* **7**, 1901040 (2019).  
<https://doi.org:https://doi.org/10.1002/adom.201901040>
- 71 Cohen, S. R. & Fourkas, J. T. Extracting Information on Linear and Nonlinear Absorption from Two-Beam Action Spectroscopy Data. *The Journal of*

- Physical Chemistry A* **123**, 7314-7322 (2019).  
<https://doi.org:10.1021/acs.jpca.9b06068>
- 72 Allonas, X., Ley, C., Bibaut, C., Jacques, P. & Fouassier, J. Investigation of the Triplet Quantum Yield of Thioxanthone by Time-Resolved Thermal Lens Spectroscopy: Solvent and Population Lens Effects. *Chem. Phys. Lett.* **322**, 483 (2000).
- 73 Amirzadeh, G. & Schnabel, W. *Die Makromolekulare Chemie* **182**, 2821-2835 (1981). <https://doi.org:10.1002/macp.1981.021821027>
- 74 Kajii, Y. *et al.* Transient absorption, lifetime and relaxation of C60 in the triplet state. *Chemical Physics Letters* **181**, 100-104 (1991).  
[https://doi.org:https://doi.org/10.1016/0009-2614\(91\)90339-B](https://doi.org:https://doi.org/10.1016/0009-2614(91)90339-B)
- 75 Rai-Constapel, V., Salzmann, S. & Marian, C. M. Isolated and Solvated Thioxanthone: A Photophysical Study. *The Journal of Physical Chemistry A* **115**, 8589-8596 (2011). <https://doi.org:10.1021/jp2022456>
- 76 Abdullah, K. A. & Kemp, T. J. Solvatochromic effects in the fluorescence and triplet-triplet absorption spectra of xanthone, thioxanthone and N-methylacridone. *Journal of Photochemistry* **32**, 49-57 (1986).  
[https://doi.org:10.1016/0047-2670\(86\)85006-7](https://doi.org:10.1016/0047-2670(86)85006-7)
- 77 Villnow, T., Ryseck, G., Rai-Constapel, V., Marian, C. M. & Gilch, P. Chimeric Behavior of Excited Thioxanthone in Protic Solvents: I. Experiments. *The Journal of Physical Chemistry A* **118**, 11696-11707 (2014). <https://doi.org:10.1021/jp5099393>
- 78 Kasha, M. Characterization of electronic transitions in complex molecules. *Discussions of the Faraday Society* **9**, 14-19 (1950).  
<https://doi.org:10.1039/DF9500900014>
- 79 Fischer, J. *et al.* Three-dimensional multi-photon direct laser writing with variable repetition rate. *Optics Express* **21**, 26244-26260 (2013).  
<https://doi.org:10.1364/OE.21.026244>
- 80 Callomon, J. H., Parkin, J. E. & Lopez-Delgado, R. Non-radiative relaxation of the excited  $\bar{A} 1B_{2u}$  state of benzene. *Chemical Physics Letters* **13**, 125-131 (1972). [https://doi.org:https://doi.org/10.1016/0009-2614\(72\)80059-9](https://doi.org:https://doi.org/10.1016/0009-2614(72)80059-9)
- 81 Knee, J. & Johnson, P. Lifetimes of dissociation-relaxed triplet states of pyrazine and pyrimidine. *The Journal of Physical Chemistry* **89**, 948-951 (1985). <https://doi.org:10.1021/j100252a012>
- 82 Otis, C. E., Knee, J. L. & Johnson, P. M. Nonradiative processes in the channel three region of the S1 state of ultracold benzene. *The Journal of Physical Chemistry* **87**, 2232-2239 (1983).  
<https://doi.org:10.1021/j100235a037>
- 83 Fischer, J. & Wegener, M. Three-dimensional optical laser lithography beyond the diffraction limit. *Laser & Photonics Reviews* **7**, 22-44 (2013).  
<https://doi.org:https://doi.org/10.1002/lpor.201100046>
- 84 Bharmoria, P., Bildirir, H. & Moth-Poulsen, K. Triplet-triplet annihilation based near infrared to visible molecular photon upconversion. *Chemical Society Reviews* **49**, 6529-6554 (2020). <https://doi.org:10.1039/d0cs00257g>

- 85 Pedrini, J. & Monguzzi, A. Recent advances in the application triplet–triplet annihilation-based photon upconversion systems to solar technologies. *Journal of Photonics for Energy* **8**, 022005 (2017).
- 86 Izakura, S., Gu, W., Nishikubo, R. & Saeki, A. Photon Upconversion through a Cascade Process of Two-Photon Absorption in CsPbBr<sub>3</sub> and Triplet–Triplet Annihilation in Porphyrin/Diphenylanthracene. *The Journal of Physical Chemistry C* **122**, 14425-14433 (2018).  
<https://doi.org/10.1021/acs.jpcc.8b05508>
- 87 Donnert, G., Eggeling, C. & Hell, S. W. Major signal increase in fluorescence microscopy through dark-state relaxation. *Nat Methods* **4**, 81-86 (2007).  
<https://doi.org/10.1038/nmeth986>
- 88 Liaros, N. & Fourkas, J. T. The Characterization of Absorptive Nonlinearities. *Laser & Photonics Reviews* **11**, 1700106 (2017).  
<https://doi.org/10.1002/lpor.201700106>
- 89 Betzig, E. *et al.* Imaging Intracellular Fluorescent Proteins at Nanometer Resolution. *Science* **313**, 1642-1645 (2006).  
<https://doi.org/10.1126/science.1127344>
- 90 Rust, M. J., Bates, M. & Zhuang, X. Sub-diffraction-limit imaging by stochastic optical reconstruction microscopy (STORM). *Nat Methods* **3**, 793-795 (2006). <https://doi.org/10.1038/nmeth929>
- 91 S., M. & T., F. J. *Laser Photonics Rev.* **2**, 100 (2008).
- 92 Howarter, J. A. & Youngblood, J. P. Optimization of Silica Silanization by 3-Aminopropyltriethoxysilane. *Langmuir* **22**, 11142-11147 (2006).  
<https://doi.org/10.1021/la061240g>
- 93 Fourkas, J. T. *et al.* in *SPIE Advanced Lithography* (SPIE, 2018).
- 94 Liaros, N., Gutierrez Razo, S. A., Tomova, Z., Petersen, J. S. & Fourkas, J. T. in *SPIE Advanced Lithography* (SPIE, 2018).
- 95 Ogden, H. M. *et al.* in *SPIE Advanced Lithography* (SPIE, 2018).
- 96 Gutierrez Razo, S. *et al.* in *SPIE Advanced Lithography* Vol. 10584 (SPIE, 2018).
- 97 Zhou, H., Song, D., Zhong, C. & Ye, G. Theoretical and Experimental Study of Light-assisted Polymerization by Multimechanism Action. *Sci Rep* **6**, 38473-38473 (2016). <https://doi.org/10.1038/srep38473>
- 98 Stalder, M. & Schadt, M. Linearly polarized light with axial symmetry generated by liquid-crystal polarization converters. *Optics Letters* **21**, 1948-1950 (1996). <https://doi.org/10.1364/OL.21.001948>